UNIVERSITY OF CALIFORNIA, SAN DIEGO

Variability in Functional Magnetic Resonance Imaging:
Influence of the Baseline Vascular State and Physiological Fluctuations

A Dissertation submitted in partial satisfaction of the requirements for the degree
Doctor of Philosophy

in

Bioengineering

by

Yashar Behzadi

Committee in charge:

- Professor Thomas T. Liu, Chair
- Professor Andrew D. McCulloch, Co-Chair
- Professor Richard B. Buxton
- Professor David Gough
- Professor Marcos Intaglietta

2006

ProQuest Information and Learning Company
300 North Zeeb Road
P.O. Box 1346
Ann Arbor, MI 48106-1346

The Dissertation of Yashar Behzadi is approved, and it is acceptable in quality and form for publication on microfilm:

Co-Chair

Chair

UNIVERSITY OF CALIFORNIA, SAN DIEGO

2006

DEDICATION

In recognition and appreciation of a lifetime of encouragement and support, I dedicate this work to my loving parents.

TABLE OF CONTENTS

Chapter 4: CompCor: Component Based Noise Correction for BOLD and Perfusion fMRI

Chapter 5: Conclusions

Appendix A1: MRI Physics Primer

Appendix A2: fMRI Primer

LIST OF ABBREVIATIONS

AFNI	Analysis of functional neuroimages
ASL	Arterial spin labeling
B_0	Static magnetic field applied in MRI
BOLD	Blood oxygenation level dependent
CBF	Cerebral blood flow
CBV	Cerebral blood volume
CMRGlu	Cerebral metabolic rate of glucose
$CMRO_2$	Cerebral metabolic rate of oxygen
CSF	Cerebral spinal fluid
CUPID	Complete utilities for processing imaging data
dHb	Deoxyhemoglobin
DWI	Diffusion-weighted imaging
EEG	Electroencephalography
EPI	Echo planar imaging
FFT	Fast Fourier transform
FID	Free induction decay
fMRI	Functional magnetic resonance imaging
fNIRS	Functional near-infrared spectroscopy
FOV	Field of view
GLM	General linear model
Hb	Hemoglobin
HDR	Hemodynamic response
ICA	Independent component analysis
LGN	Lateral geniculate nucleus

NMR	Nuclear magnetic resonance
PCA	Principal component analysis
PET	Positron emission tomography
RF	Radio frequency
ROI	Region-of-interest
nROI	Noise region-of-interest
SNR	Signal-to-noise
SVD	Singular value decomposition
T_1	Longitudinal magnetization recovery constant
T_2	Transverse magnetization decay constant
T_{2*}	Transverse magnetization decay constant including field inhomogeneity effects
TE	Echo time
TI	Inversion time
TR	Time of repetition
tSTD	Temporal standard deviation
VASO	Vascular space occupancy

LIST OF FIGURES AND TABLES

ACKNOWLEDGEMENTS

I would like to thank my advisor Professor Thomas T. Liu for his dedicated tutelage and generosity. Always a friend, Professor Liu was responsible for making my graduate years an enjoyable and valuable experience. In appreciation of their time, I would also like to thank my thesis committee.

I am grateful for the friendship of Khaled Restom and Joanna Perthen despite their constant efforts to introduce bugs into CUPID. Additionally, I would like to thank all my other friends and co-workers at the Center. For pushing me and allowing needed flexibility, I am grateful to Cliff Lewis.

For all the daily trips and discussions, I would like to thank Peter Costandi. For brain storming sessions, their friendship, and for fostering my ambitions, I like to thank fellow BE's Carlos Uranga, Nick Rahaghi and Ben Sullivan.

There since the beginning of it all, I am incredibly grateful to Shahram, Tom, Ben, and Jed. For countless conversations and a fair bit of world traveling, I am thankful to my good friend Tim. There to always provide a needed break, I am thankful to Roland, Ryan, and Zank.

For inspiring me to be a better person and loving me through it all, I am greatly indebted to my love Myra. I would like to thank my siblings and parents, for being my life-long best friends and truly an inspiration in every facet of my life. I am also grateful to my grandparents, aunts, uncles, and cousins for providing me the needed perspective on what is truly important in life.

Chapter 2, in full, is a reprint of the material as it appears in:

Behzadi, Y., and Liu, T.T., (2005) An arteriolar compliance model of the cerebral blood flow response to neural stimulus. *Neuroimage*. 25(4), 1100-1111.

The dissertation author was the primary author of these papers. I would like to acknowledge my co-author Professor Thomas T. Liu.

Chapter 3, in full, is a reprint of the material as it appears in:

Behzadi, Y., and Liu, T.T., (2006) Caffeine reduces the initial dip in the visual BOLD response at 3T. *Neuroimage*, 32(1), 9-15.

The dissertation author was the primary author of these papers. I would like to acknowledge my co-author Professor Thomas T. Liu.

VITA

-EDUCATION-

2006	Doctor of Philosophy, Bioengineering, University of California, San Diego.
2003	Master of Science, Bioengineering, University of California, San Diego.
2001	Bachelor of Science, Bioengineering, University of California, San Diego.

-EXPERIENCES-

2001–Present	Scientist Advanced Concepts Business Unit Technology Research and Integration Business Unit Science Applications International Corporation, San Diego, CA.
1/2006-Present	Co-founder, Organizing Chair UCSD $50K Entrepreneurship Competition San Diego, CA.
10/2002-6/2003	Co-founder, Product Director CYAN Automated Pathology San Diego, CA.
6/1999-6/2001	Process Engineer Canji Inc. (Subsidiary of Schering-Plough) San Diego, CA.
9/2000–1/2001	Bioengineer Advanced Tissue Sciences Inc. San Diego, CA
9/1997-5/1999	Research Assistant The Scripps Research Institute San Diego, CA.

-PUBLICATIONS-

Refereed Publications:

Behzadi, Y., and Liu, T.T., (2006) CompCor: Component-Based Noise Correction for BOLD and Perfusion Based fMRI, *Neuroimage*, in-preparation.

Behzadi, Y., and Liu, T.T., (2006) Caffeine reduces the initial dip in the visual BOLD response at 3T. *Neuroimage*, 32(1), 9-15.

Behzadi, Y., and Liu, T.T., (2005) An arteriolar compliance model of the cerebral blood flow response to neural stimulus. *Neuroimage*. 25(4), 1100-1111.

Restom, K., Behzadi, Y., Liu, T.T., (2006) Physiological noise removal for arterial spin labeling functional MRI. *Neuroimage,* 31(3), 1104-1115

Liu, T.T., Behzadi, Y., Restom, K., Uludag, K., Lu, K., Buracas, G.T., Dubowitz, D. J., and Buxton, R.B. (2004) Caffeine alters the temporal dynamics of the visual BOLD response. *Neuroimage*. 23(4), 1402-1413.

Conference Oral Presentations:

Behzadi, Y., Restom, K., Liu, T.T. Component Based Noise Correction for Perfusion fMRI, in *"Proc of. 13th Meeting, International Society for Magnetic Resonance in Medicine, Seattle, 2006."* May, 2006.

Behzadi, Y., Liu, T.T., Reducing inter-voxel variability of the BOLD response with measurement of resting blood flow, in *"Proc. of 13th Meeting, International Society for Magnetic Resonance in Medicine, Seattle, 2006."* May, 2006.

Behzadi, Y., Restom, K., Liu, T.T. Modeling the Effect of Baseline Arteriolar Compliance on BOLD Dynamics, in *"Proc. of Eleventh Meeting, International Society for Magnetic Resonance in Medicine, Kyoto, 2004."* July, 2004.

Behzadi, Y., Restom, K., Liu, T.T. Volterra Kernel Analysis of Event-Related fMRI Data Using Laguerre Basis Functions, in *"Proc of . Eleventh Meeting, International Society for Magnetic Resonance in Medicine, Toronto, 2003."* May 2003.

Select Conference Papers:

Behzadi, Y., Liu, T.T., Modeling the Temporal Dynamics of the Positive and Negative BOLD Response, in *"Proc. of 13th Meeting, International Society for Magnetic Resonance in Medicine, Seattle, 2006."* May, 2006.

Behzadi, Y., Liu, T.T., Effect of background suppression and physiological noise removal on the sensitivity of arterial spin labeling fMRI, in *"Proc. of 13th Meeting, International Society for Magnetic Resonance in Medicine, Seattle, 2006."* May, 2006.

Liau, J., Behzadi, Y., Liu, T.T., Caffeine Reduces the Initial Dip in the Visual BOLD Response, in *"Proc. of 13th Meeting, International Society for Magnetic Resonance in Medicine, Seattle, 2006."* May, 2006.

Perthen, J.E., Restom, K., Behzadi, Y., Lu, K., Liu, T.T. Accurate perfusion quantification using pulsed arterial spin labeling: Choosing appropriate sequence parameters, in *"Proc. of 13th Meeting, International Society for Magnetic Resonance in Medicine, Seattle, 2006."* May, 2006.

Restom, K., Behzadi, Y., Perthen, J.E., Liu, T.T. A Filtered Subtraction Approach for the Reduction of Physiological Noise in Perfusion Based fMRI, in *"Proc. of 13th Meeting, International Society for Magnetic Resonance in Medicine, Seattle, 2006."* May, 2006.

Liu, T.T., Behzadi, Y., Restom, K., Smith, G., Townsend, J. An Index of Low Frequency (0.1 Hz) Spectral Power Predicts Changes in the Amplitude and Shape of the BOLD Response, in *"Proc. of 13th Meeting, International Society for Magnetic Resonance in Medicine, Seattle, 2006."* May, 2006.

Behzadi, Y., Liu, T.T., The Viscoelastic Properties of the Venous Compartment are Dependent on the Baseline Cerebral Blood Flow in *"Proc of Twelfth Meeting, International Society for Magnetic Resonance in Medicine, Miami, 2005."* May, 2005.

Behzadi, Y., Restom, K., Liu, T.T., Background 0.1 Hz fluctuations are not in phase with post-stimulus oscillations in BOLD fMRI, in *"Proc. of Eleventh Meeting, International Society for Magnetic Resonance in Medicine, Kyoto,2004."* June, 2004.

-TEACHING EXPERIENCE-

1/2001-3/2001	MAE 152	Computer Graphics and Design for Engineers
4/2002-6/2002	BE 172	Experimental Methods for Bioengineers
1/2003-3/2003	BE 112A	Biomechanics
4/2003-6/2003	BE 186C	Bioengineering Senior Design
9/2003-12/2003	BE 280A	Biomedical Imaging

-PROFESSIONAL AND SCIENTIFIC SOCIETIES-

2003-Present	International Society of Magnetic Resonance in Medicine
2001-Present	Golden Key Honor Society

-ACADEMIC HONORS-

2003	First Place, Venture Forth Business Plan Competition
1998-2001	Henry Mayo Newhall Memorial Scholarship
1998	Target All-Around Scholarship

ABSTRACT OF THE DISSERTATION

Variability in Functional Magnetic Resonance Imaging: Influence of the Baseline Vascular State and Physiological Fluctuations

by

Yashar Behzadi

Doctor of Philosophy in Bioengineering

University of California, San Diego, 2006.

Professor Thomas T. Liu, Chair

Professor Andrew D. McCulloch, Co-chair

In recent years, functional magnetic resonance imaging (fMRI) has become an increasingly important tool for studying the working human brain. The blood oxygenation level dependent signal signal used in most fMRI experiments is an indirect measure of neural activity and reflects local changes in deoxyhemoglobin content, which is a complex function of dynamic changes in cerebral blood flow, cerebral blood volume, and the cerebral metabolic rate of oxygen. Although significant progress has been made in characterizing and modeling the link between neural activity and the hemodynamic response, the quantitative interpretation of basic neuroscience and clinical studies has been limited by sources of variability unrelated to the evoked neural response.

The fMRI signal has been shown to have a complex dependence on the baseline vascular state. This dependence is especially relevant in clinical settings where significant variations in the vascular state due to factors such as aging, disease, medication, or diet can confound the interpretation of the data. Additionally, physiological fluctuations, related to the respiratory and cardiac cycle, have been shown to modulate the fMRI signal and are becoming an increasingly important confound as neuroimaging moves to higher magnetic field strengths.

The first objective of this work is to characterize and model the effect of the baseline vascular state on the dynamics of the fMRI signal. The second objective of this work is to develop a technique to reduce the effect of physiological fluctuations on the fMRI signal. Developments proposed in this work represent an important step in developing fMRI as a quantitative research and clinical tool.

Chapter 1

Introduction

1.1 fMRI: An Introduction

Understanding the roots of consciousness and cognition in the human brain has been a fundamental scientific endeavor for hundreds of years; spanning the realms of psychology, biology, and philosophy. Over the last decade, researchers have increasingly looked to functional magnetic resonance imaging (fMRI) as a powerful non-invasive tool to help study the working human brain.

fMRI is rooted in the observations of Italian physiologist Mosso who in 1881 was the first to describe a functional change in regional brain circulation evoked by a mental task (Mosso, 1881). He noted that with mental calculation brain pulsations rose over the right prefrontal cortex in a patient with a bony defect in the skull (Mosso, 1881). Roy and Sherrington (1890) later presented the idea of the regional control of cerebral blood flow (CBF), generally stating that chemical byproducts of cerebral metabolism associated with increased neural activity regulated the caliber of nearby arterioles (Roy et al., 1890). Direct measurements of CBF in humans were not possible until 1948 when Kety and Schmidt introduced the nitrous oxide technique (Kety et al., 1948). Although this technique was limited to measuring global perfusion it led to subsequent techniques using radioactive tracers. In turn, these techniques led to the development of Positron Emission Tomography (PET) in 1970's and 1980's, which allowed insight into the local metabolic and hemodynamic responses to neural activation on a spatial scale of several centimeters.

In 1990, Ogawa et al. first demonstrated modulation of the magnetic resonance (MR) signal with physiological manipulations of blood oxygenation (Ogawa et al., 1990). Coined the blood oxygenation level dependent (BOLD) signal, this phenomena formed the foundation of fMRI. With neural activation, an accompanying increase in neuronal energy consumption triggers regional cerebral blood flow (CBF) increases that serve to deliver needed nutrients (O_2, glucose, etc) and remove unwanted byproducts (lactate, heat, etc.). Coupled with changes in cerebral blood volume (CBV) and oxygen extraction, the regional CBF alters the concentration of deoxyhemoglobin [dHb]. Hb possesses a useful magnetic property in that it is diamagnetic when oxygenated and paramagnetic when deoxygenated (Pauling et al., 1936). dHb affects the magnetic susceptibility within and around blood vessels, creating microscopic inhomogenities, which cause a greater degree of spin dephasing (Ogawa et al., 1990). The MR signal is consequently reduced in the presence of dHb. As a result, dHb acts as an endogenous contrast agent that serves as an indirect marker of localized neural activity. Leveraged into the BOLD effect, changes in dHb content with neural activity serve as the basis of fMRI.

fMRI, utilizing the BOLD signal, has been used extensively for brain mapping and confirmed the spatial location of known anatomically distinct processing areas such as the visual cortex (Belliveau et al., 1991); (Blamire et al., 1992, the motor cortex {Kim, 1993 #285; Kim et al., 1993) and Broca's area of speech and language-related activities (Hinke et al., 1993). The main advantages to fMRI as a technique to image brain activity is that the signal does not require injections of radioactive isotopes, the total scan time required can be on the order of minutes per run, and the in-plane resolution of the functional image can be as small as 1mm. An emerging advantage of fMRI is the ability to obtain and integrate measurements related to other physiological parameters. For example, CBF can be measured with Arterial Spin Labeling (ASL), a class of non-invasive MRI methods that involve taking the difference of two sets of images: tag images, in which the magnetization of arterial blood is inverted or saturated, and control images in which the magnetization of arterial blood in fully relaxed (Golay et al., 2004).

Although a powerful technique, fMRI provides only an indirect measure of neural activity related to the interaction of the neural and hemodynamic systems. The hemodynamic response (HDR) entails the complicated interaction of dynamic changes in CBF, CBV, and the cerebral metabolic rate of oxygen ($CMRO_2$). Although 125 years have passed since Mosso's observation that local perfusion is coupled to neural activity, the details of the hemodynamic events following neural activity remain to be fully described.

1.2 fMRI: Evoked Signal Response

A simple schematic of the fMRI response is presented in Figure 1.1. The basic picture of the hemodynamic response to neural activity is simple although the specifics are complex and not entirely understood. With neural activity, tissue metabolism is increased to support neuronal firing and the restoration of ionic gradients. The release of various vasoactive agents modulates CBF which consequently drive changes in CBV and together with $CMRO_2$ determine the [dHb]. As described earlier, the resulting BOLD signal is a function of the total dHb content. A more comprehensive examination of the neural and metabolic events underlying the BOLD signal as well as the associated MR physics is provided in the appendices.

A typical evoked BOLD signal is presented in Figure 1.2. In the first few seconds following the onset of increased neural activity, tissue metabolism increases rapidly leading to increases in oxygen consumption and CBF. With activation CBF increases much more than $CMRO_2$ resulting in a large influx of fully oxygenated blood and a decreases in [dHb]. As mentioned previously, the presence of dHb increases local spin dephasing and decreases the MR signal. Decreases in [dHb] following large CBF increases lead to a positive BOLD signal as depicted in figure 1.2. If in the first few seconds of the BOLD response, the $CMRO_2$

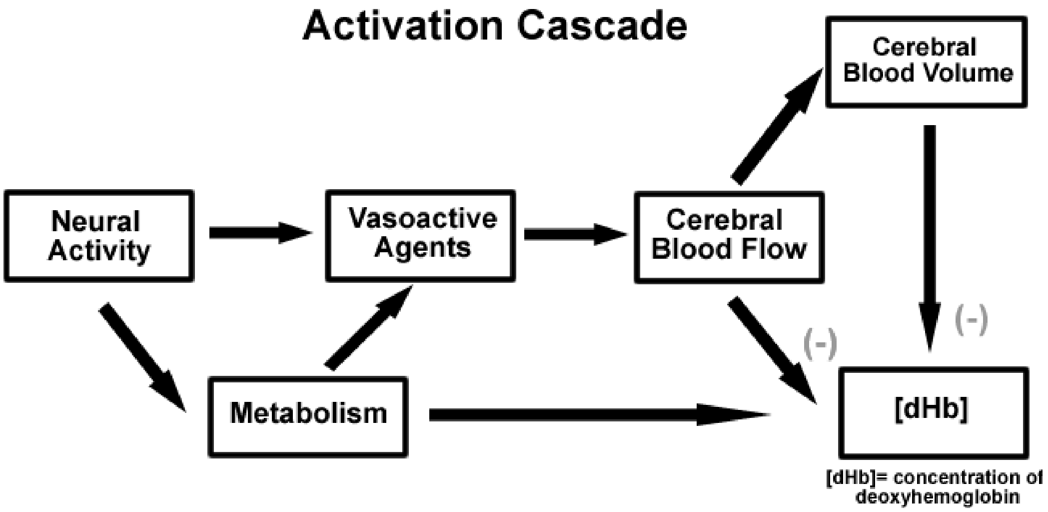

Figure 1.1. Simplified cascade of events following evoked neural activity. Evoked neural activity leads to increases in tissue metabolism and the release of various vasoactive agents which regulate the local blood flow. Changes in the local blood flow modulate the blood volume and the [dHb].

increases more quickly than CBF, it can lead to an initial transient increase in dHb and an associated “initial dip” in the BOLD signal (Ernst et al., 1994; Hu et al., 1997; Malonek et al., 1996; Menon et al., 1995; Thompson et al., 2004). The typical BOLD response can be parameterized by the rise-time, full-width-half-maximum (FWHM), and the peak amplitude of the response. The CBF and BOLD responses are typically delayed 1-2 seconds following neural activity and have a broad temporal width on the order of 4-6 s (Bandettini et al., 1992). A post-stimulus undershoot is often observed and is thought to reflect the slow resolution of CBV with respect to CBF following cessation of stimulus (Buxton et al., 2004).

1.3 Influence of the Baseline Vascular State

A number of recent studies have shown that the dynamic CBF and BOLD response to neural stimulus exhibits an intriguing dependence on the baseline CBF level. Studies in visual cortex have shown that the temporal width and time to peak of the visual BOLD response increases with hypercapnia and decreases with hypocapnia, while the peak amplitude of the response show the opposite dependence (Cohen et al., 2002; Kemna et al., 2001). Studies in our laboratory have shown that caffeine has similar effects as hypocapnia and can lead to significant variation in the observed BOLD signal (Liu et al., 2004).

There is also growing evidence to suggest that the dynamics of the BOLD response change with age. Some studies of the dynamic BOLD response have described age-related increases in the temporal parameters (e.g. latency, time to peak) of the response (Mehagnoul-Schipper et al., 2002; Richter et al., 2003; Taoka et al., 1998). The baseline vascular state can affect various physiological parameters responsible for the CBF and BOLD responses. Figure 1.3 is a schematic outlining the possible influence of the baseline vascular state on the governing physiological parameters of the BOLD response. Understanding the effect of the baseline vascular state on BOLD dynamics is important for many clinical studies. For example,

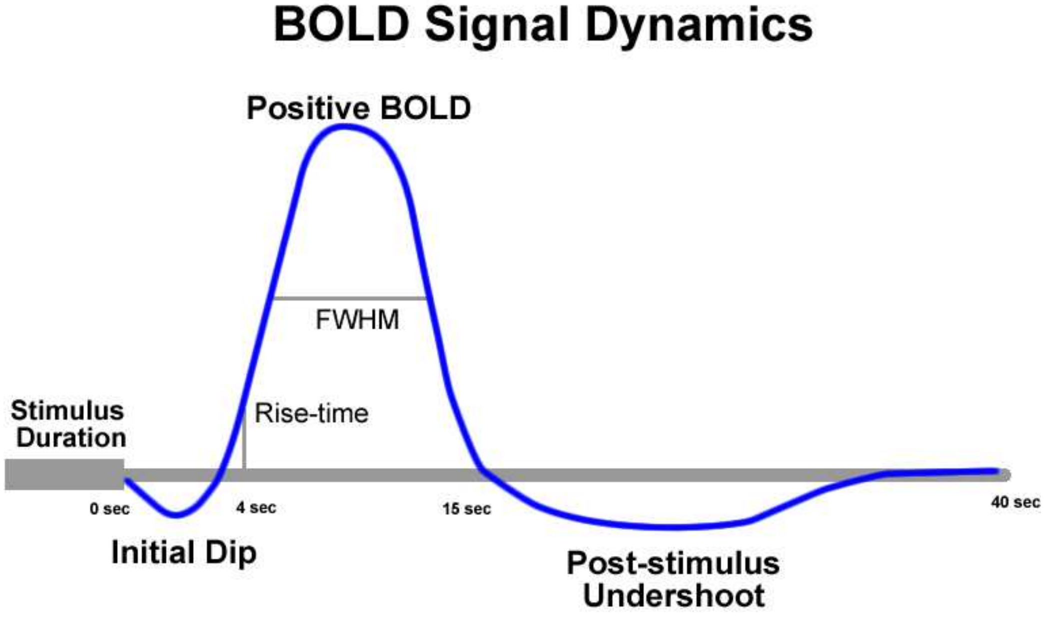

Figure 1.2. Schematic of a typical evoked BOLD response. Following stimulus onset, the initial increase in $CMRO_2$ leads to increased dHb and to an "initial dip" in the BOLD response. CBF then increases more than $CMRO_2$ driving dHb down and leading to the positive BOLD response. The post-stimulus undershoot recovers slowly back to baseline and is thought to arise from the slow resolution of CBV relative to CBF.

a study investigating the effect of a drug on neural activity may be complicated if the drug also has vasoactive effects. The potential differences between treatment groups may be interpreted as differences in the underlying neural activity although a significant portion of the effect is attributed to the drug's effect on the baseline vascular state. Complications may also arise in studies in which members of a study group have significantly different vascular states. This is an inevitable complication in studies comparing young and elderly adults. A model capable of describing the complex dependence of the observed BOLD dynamics on the baseline vascular state will be beneficial in the interpretation of fMRI studies.

1.4 The Elusive Initial Dip

The observed dynamics of the evoked BOLD response have sparked debate in the fMRI literature. An ongoing debate in fMRI has centered on the presence of the initial dip. As mentioned previously in section 1.2, the initial dip of the BOLD response has been attributed to an immediate increase in $CMRO_2$ prior to CBF increases. Several investigators have shown that the initial dip is well localized to areas of neural activity (e.g. cortical columns), whereas the delayed positive BOLD response is more diffuse, most likely reflecting coarse CBF control (Duong et al. 2000; Yacoub et al. 2001; Kim et al. 2000; Yacoub and Hu 2001). The increased spatial specificity of the initial dip compared to the positive BOLD response has been of particular interest to the brain mapping community. However, the initial dip is not always detected and different research groups have debated its presence (Buxton, 2001).

Since the initial dip is a result of the temporal mismatch between $CMRO_2$ and CBF dynamic responses, modulation of either response will affect the detection of the initial dip. As previously mentioned, the baseline vascular state has been shown to modulate the CBF response and it may also play a role in the detection of the initial dip of the BOLD response.

1.5 Influence of Physiological Noise

Further complicating the interpretation of the fMRI signal is the confounding effect of physiological noise. Physiological fluctuations have been shown to be a significant source of noise in BOLD fMRI experiments with a more pronounced effect in perfusion-based fMRI utilizing ASL techniques (Kruger et al., 2001; Restom et al., 2006). Figure 1.3, depicts the effect of physiological noise on the governing physiological parameters of the BOLD signal. The local blood flow is a function of cardiac cycle and the movement of the thoracic cavity with respiration modulates the main magnetic field, B_0, which affects imaging (Glover et al., 2000; Hu et al., 1995).

Physiological noise has been shown to be a limiting factor for perfusion and BOLD-based studies in the medial temporal lobe (Restom et al., 2006). Also the decreased signal-to-noise in elderly subjects compared to younger adults has been attributed to the greater inherent physiological noise (Huettel et al., 2001). The importance of removing physiological noise from the fMRI signal is especially relevant in studies of Alzheimer's disease, in which researchers aim to probe the subtle differences in the fMRI response in the medial-temporal lobe of elderly subjects.

Physiological noise is an important confound limiting the application of fMRI and many approaches have been developed to remove cardiac and respiratory related-noise. Methods include the use of pulse-oximeter time courses (Biswal et al., 1996; Hu et al., 1995), image based retrospective correction (RETROICOR), k-space based correction (RETROKCOR) and navigator echo based correction (DORK) (Glover et al., 2000; Josephs et al., 2001; Pfeuffer et al., 2002). However, these approaches have not been universally implemented since they require external monitoring of physiological processes or pulse sequence adaptations. An approach not dependent on the use of external monitoring equipment or pulse sequence adaptation will be valuable to the broad fMRI community.

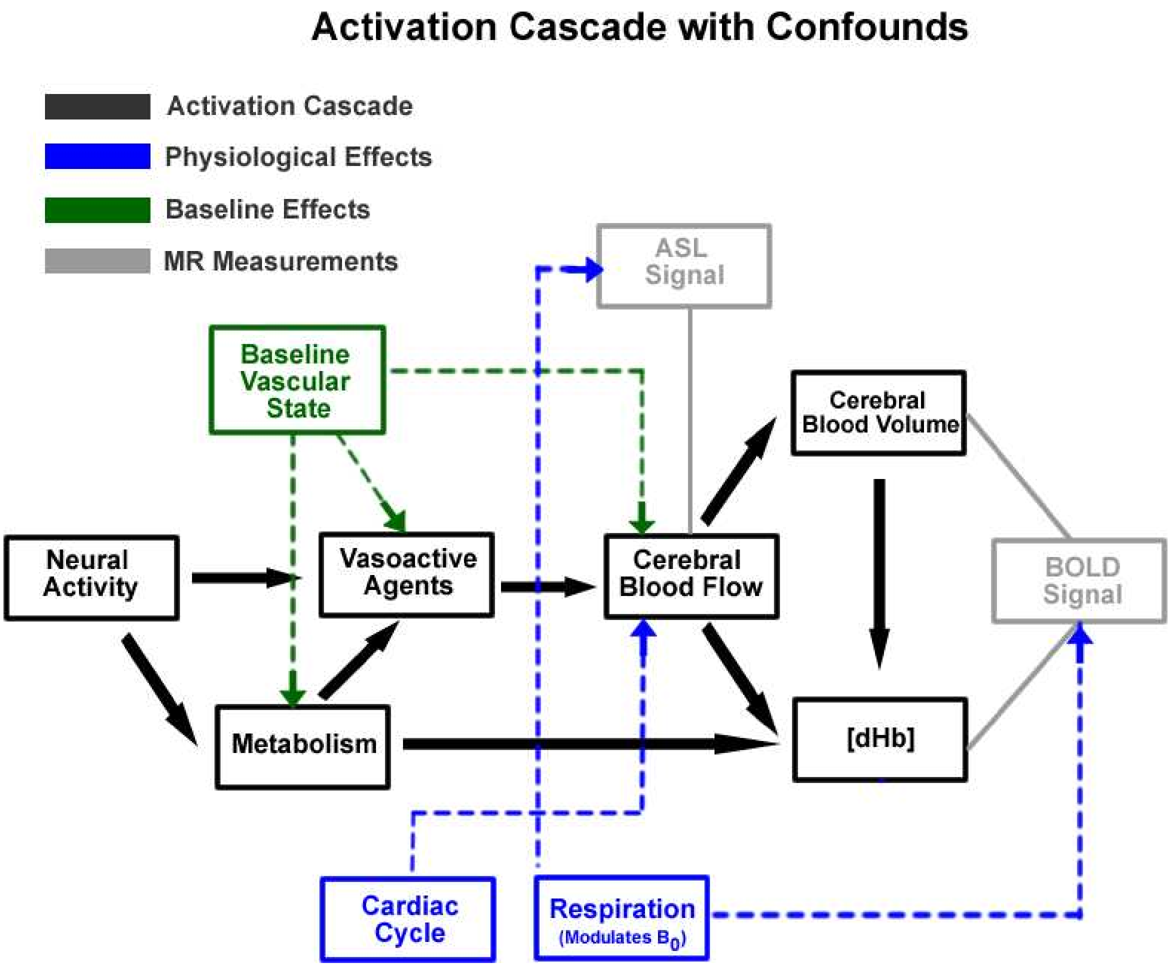

Figure 1.3. Schematic activation cascade (black) showing the confounding effects of the cardiac cycle and respiration (blue) along with the effect of the baseline vascular state (green) on various physiological quantities. The fMRI signals (gray) are strongly affected by these confounds.

1.6 Thesis Outline

The first objective of this thesis is to characterize and model the effect of the baseline vascular state on the dynamics of the fMRI signal. The second objective of this work is to develop a robust technique for the reduction of physiological noise in fMRI time-series data.

Chapter 2 will present an arteriolar compliance model of the evoked CBF response to neural stimulus. Coupled with the balloon model of the BOLD response, the combined model will be used to interpret and predict the experimentally observed dependence of the dynamics of the fMRI response on the baseline vascular state.

In chapter 3 we will investigate the effect of the baseline vascular state, as modulated by caffeine, on the detection of the initial dip. This study will serve to highlight the importance of the baseline vascular state on the dynamics of the fMRI signal and provide insight into the ongoing debate regarding the presence of the initial dip.

Chapter 4 will provide an in depth exploration of the effect of physiological noise on fMRI time-series data. A novel component-based correction (CompCor) scheme will be presented for the reduction of noise in BOLD and perfusion-based fMRI and compared to an established retrospective image based technique for the reduction of cardiac and respiratory induced noise. CompCor will be shown to be a robust method for the effective removal of cardiac and respiratory noise in the fMRI signal.

This thesis will conclude with a summary of the contributions and future directions of the work presented in chapters 2-4. The accompanying appendices provide an introduction on the biophysical origin of the fMRI signal, in which a primer on MR physics is followed by a comprehensive review of neurovascular coupling as related to the CBF and BOLD responses.

1.7 References

Bandettini P. A., Wong E. C., Hinks R. S., Tikofsky R. S., and Hyde J. S. (1992) Time course EPI of human brain function during task activation. *Magn Reson Med*. 25, 390-397.

Belliveau J. W., Kennedy D. N., McKinstry R. C., Buchbinder B. R., Weisskoff R. M., Cohen M. S., Vevea J. M., Brady T. J., and Rosen B. R. (1991) Functional mapping of the human visual cortex by magnetic resonance imaging. *Science*. 254, 716-719.

Biswal B., DeYoe A. E., and Hyde J. S. (1996) Reduction of physiological fluctuations in fMRI using digital filters. *Magn Reson Med*. 35, 107-113.

Blamire A. M., Ogawa S., Ugurbil K., Rothman D., McCarthy G., Ellermann J. M., Hyder F., Rattner Z., and Shulman R. G. (1992) Dynamic mapping of the human visual cortex by high-speed magnetic resonance imaging. *Proc Natl Acad Sci USA*. 89, 11069-11073.

Buxton R. B. (2001) The elusive initial dip. *Neuroimage*. 13, 953-958.

Buxton R. B., Uludag K., Dubowitz D. J., and Liu T. T. (2004) Modeling the hemodynamic response to brain activation. *Neuroimage*. 23 Suppl 1, S220-233.

Cohen E. R., Ugurbil K., and Kim S. G. (2002) Effect of basal conditions on the magnitude and dynamics of the blood oxygenation level-dependent fMRI response. *J Cereb Blood Flow Metab*. 22, 1042-1053.

Ernst T. and Hennig J. (1994) Observation of a fast response in functional MR. *Magn Reson Med*, 146-149.

Glover G. H., Li T.-Q., and Ress D. (2000) Image-based method for retrospective correction of physiological motion effects in fMRI: RETROICOR. *Magn Res Med*. 44, 162-167.

Golay X., Hendrikse J., and Lim T. C. (2004) Perfusion Imaging Using Arterial Spin Labeling. *Top Magn Reson Imaging*. 15, 10-27.

Hinke R. M., Hu X., Stillman A. E., Kim S.-G., Merkle H., Salmi R., and Ugurbil K. (1993) Functional magnetic resonance imaging of brocs's area during internal speech. *Neuroreport*. 4, 675-678.

Hu X., Le T. H., Parrish T., and Erhard P. (1995) Retrospective estimation and correction of physiological fluctuation in functional MRI. *Magn Reson Med*. 34, 201-212.

Hu X., Le T. H., and Ugurbil K. (1997) Evaluation of the early response in fMRI in individual subjects using short stimulus duration. *Magn Reson Med*. 37, 877-884.

Huettel S. A., Singerman J. D., and McCarthy G. (2001) The effects of aging upon the hemodynamic response measured by functional MRI. *Neuroimage*. 13, 161-175.

Josephs O., Howseman A., Friston K. J., and Turner R. (2001) Physiological Noise Modelling for multi-slice EPI fMRI using SPM. *Proc Intl Soc Mag Reson Med*, 1682.

Kemna L. J. and Posse S. (2001) Effect of respiratory CO(2) changes on the temporal dynamics of the hemodynamic response in functional MR imaging. *Neuroimage*. 14, 642-649.

Kety S. and Schmidt C. (1948) Nitrous oxide method for the quantitative determination of cerebral blood flow in man: Theory, procedure and normal values. *J Clin Invest*. 27, 475-483.

Kim S.-G., Ashe J., Hendrich K., Ellerman J. M., Merkle H., Ugurbil K., and Georgopoulos A. P. (1993) Functional magnetic resonance imaging of motor cortex: hemispheric asymmetry and handedness. *Science*. 261, 615-616.

Kruger G. and Glover G. H. (2001) Physiological noise in oxygenation-sensitive magnetic resonance imaging. *Magn Reson Med*. 46, 631-637.

Liu T. T., Behzadi Y., Restom K., and Uludag K. (2004) Caffeine Affects the Dynamics of the Visual BOLD Response. *NeuroImage*. 22, TU148.

Malonek D. and Grinvald A. (1996) Interactions between electrical activity and cortical microcirculation revealed by imaging spectroscopy: implications for functional brain mapping. *Science*. 272, 551-554.

Mehagnoul-Schipper D. J., van der Kallen B. F., Colier W. N., van der Sluijs M. C., van Erning L. J., Thijssen H. O., Oeseburg B., Hoefnagels W. H., and Jansen R. W. (2002) Simultaneous measurements of cerebral oxygenation changes during brain activation by near-infrared spectroscopy and functional magnetic resonance imaging in healthy young and elderly subjects. *Hum Brain Mapp*. 16, 14-23.

Menon R. S., Ogawa S., Strupp J. P., Anderson P., and Ugurbil K. (1995) BOLD based functional MRI at 4 tesla includes a capillary bed contribution: echo-planar imaging correlates with previous optical imaging using intrinsic signals. *Magn Reson Med*. 33, 453 - 459.

Mosso A. (1881) *Uber den Kreislauf des Blutes im Menschlichen Gehirn.* Verlag von Veit & Co., Leipzig.

Ogawa S. and Lee T.-M. (1990) Magnetic resonance imaging of blood vessels at high fields: in vivo and in vitro measurements and image simulation. *Magn Reson Med*. 16, 9-18.

Pauling L. and Coryell C. D. (1936) The magnetic properties and structure of hemoglobin, oxyhemoglobin, and carbonmonoxyhemoglobin. *Proc Natl Acad Sci USA*. 22, 210-216.

Pfeuffer J., Van de Moortele P. F., Ugurbil K., Hu X., and Glover G. H. (2002) Correction of physiologically induced global off-resonance effects in dynamic echo-planar and spiral functional imaging. *Magn Reson Med*. 47, 344-353.

Restom K., Behzadi Y., and Liu T. T. (2006) Physiological noise reduction for arterial spin labeling functional MRI. *Neuroimage*. 31, 1104-1115.

Richter W. and Richter M. (2003) The shape of the fMRI BOLD response in children and adults changes systematically with age. *Neuroimage*. 20, 1122-1131.

Roy C. S. and Sherrington C. S. (1890) On the regulation of the blood-supply of the brain. *J Physiol*. 11, 85-108.

Taoka T., Iwasaki S., Uchida H., Fukusumi A., Nakagawa H., Kichikawa K., Takayama K., Yoshioka T., Takewa M., and Ohishi H. (1998) Age correlation of the time lag in signal change on EPI-fMRI. *J Comput Assist Tomogr*. 22, 514-517.

Thompson J. K., Peterson M. R., and Freeman R. D. (2004) High-resolution neurometabolic coupling revealed by focal activation of visual neurons. *Nat Neurosci*. 7, 919-920.

Chapter 2

An Arteriolar Compliance Model of the CBF Response to Neural Stimulus

2.1 Abstract

Although functional magnetic resonance imaging (fMRI) is a widely used and powerful tool for studying brain function, the quantitative interpretation of fMRI measurements for basic neuroscience and clinical studies can be complicated by inter-subject and inter-session variability arising from modulation of the baseline vascular state by disease, aging, diet, and pharmacological agents. In particular, recent studies have shown that the temporal dynamics of the cerebral blood flow (CBF) and the blood oxygenation level dependent (BOLD) responses to stimulus are modulated by changes in baseline CBF induced by various vasoactive agents and by decreases in vascular compliance associated with aging. These effects are not readily explained using current models of the CBF and BOLD responses. We present here a second-order nonlinear feedback model of the evoked CBF response in which neural activity modulates the compliance of arteriolar smooth muscle. Within this model framework, the baseline vascular state affects the dynamic response by changing the relative contributions of an active smooth muscle component and a passive connective tissue component to the overall vessel compliance. Baseline dependencies of the BOLD signal are studied by coupling the arteriolar compliance model with a previously described balloon model of the venous compartment. Numerical simulations show that the proposed model describes to first order the observed dependence of CBF and BOLD responses on the baseline vascular state.

2.2 Introduction

The blood oxygenation level dependent (BOLD) signal used in most fMRI experiments reflects local changes in deoxyhemoglobin content, and is a complex function of dynamic changes in cerebral blood flow (CBF), cerebral blood volume (CBV), and the cerebral metabolic rate of oxygen ($CMRO_2$) (Buxton et al., 1998). Although significant progress has been made in characterizing and modeling the hemodynamic response (HDR) to brain activation (Buxton et al., 1998; Hoge et al., 1999; Logothetis et al., 2004; Mandeville et al., 1999), the quantitative interpretation of fMRI measurements is complicated by inter-subject and inter-session variability caused by differences in baseline physiology. An understanding of this dependency is especially relevant to the application of fMRI in clinical settings where significant variations in vascular state due to factors such as aging, disease, medication or diet can confound the interpretation of the data (D'Esposito et al., 2003; Handwerker et al., 2004)

A number of recent studies have shown that the dynamic CBF response to neural stimulus exhibits an intriguing dependence on the baseline CBF level. Laser Doppler flow measurements characterizing the dynamic CBF response in rats indicate that the response slows down significantly with elevated baseline CBF due to hypercapnia (Ances et al., 2001; Bakalova et al., 2001; Matsuura et al., 2000) and speeds up slightly with decreased baseline CBF due to either hypocapnia (Matsuura et al., 2000) or hyperoxia (Matsuura et al., 2000; Matsuura et al., 2001). An arterial spin labeling MRI study in rats has reported similar results (Silva et al., 1999). In humans, a hypocapnia-induced decrease in the rise time of the velocity response to visual stimulation has been observed in an ultrasound Doppler study of the posterior cerebral artery (Rosengarten et al., 2003). Additional evidence for a change in CBF dynamics can be inferred from BOLD measurements. Studies in visual cortex have shown that the temporal width and time to peak of the visual BOLD response increases with hypercapnia and decreases with hypocapnia, while the peak amplitude of the response show the opposite dependence (Cohen et al., 2002; Kemna et al., 2001). In addition, the post stimulus undershoot in the response resolved more quickly with hypocapnia and appeared to be abolished with hypercapnia (Cohen et al., 2002). Cohen et al (Cohen et al., 2002) note that the observed changes are perplexing, since a decrease in baseline CBF might be expected to correspond to reduced blood velocities and therefore a slower dynamic response (see for example, simulations in (Mildner et al., 2001)). The effect of hyperoxia on the BOLD response appears to be similar to the effect of hypocapnia and is consistent with laser Doppler flow findings in rats (Kashikura et al., 2001).

There is also growing evidence to suggest that the dynamics of the HDR change with age. Some studies of the dynamic BOLD response have described age-related increases in the temporal parameters (e.g. latency, time to peak) of the response (Mehagnoul-Schipper et al., 2002; Richter et al., 2003; Taoka et al., 1998). However, other studies have reported no changes with age (Buckner et al., 2000; D'Esposito et al., 1999). The reports of increases in the temporal parameters are consistent with the results of a functional near-infrared spectroscopy (fNIRS) showing broadening and less undershoot in the time courses of oxyHB and deoxyHB in prefrontal cortex for the elderly subjects as compared to young subjects (Schroeter et al., 2003). Similarly, an ultrasound Doppler study of velocity increases in the posterior cerebral artery induced by visual stimulation found significant age-related decreases in the slopes of the velocity response (Panczel et al., 1999). The slowing down of the vascular dynamics may be related to the age-related reduction in the elasticity of the arteriolar wall, which reflects a decrease in smooth muscle and elastin components and an increase in the less distensible collagen and basement membrane components (Hajdu et al., 1990; Riddle et al., 2003). In addition, the decrease in baseline CBF with age may play a role (Bentourkia et al., 2000; Leenders et al., 1990; Marchal et al., 1992; Martin et al., 1991). The studies described suggest the following working observations: baseline CBF decreases with age, vascular compliance decreases with age, and the HDR decreases in amplitude and slows down with age. Note that in marked contrast to the quickening of the HDR with baseline CBF decreases induced by vasoconstrictive agents, the age-related decrease in baseline CBF is associated with a slowing down of the HDR.

As the field of fMRI has evolved, several dynamic models of the HDR have been developed. Two popular models, the *balloon model* and the *post-arteriole windkessel model,* were motivated in part by observations of a post-stimulus undershoot in the BOLD response and of differences between the CBF and CBV dynamic responses (Buxton et al., 1998; Mandeville et al., 1999). In these models, CBF is the input that drives changes in CBV. To calculate the BOLD response, the balloon model is coupled to a dynamic model of the total amount of deoxyhemoglobin that reflects mass conservation and the relation between $CMRO_2$ and CBF (Buxton et al., 1998).

To generate a CBF response that could be used as an input to the balloon model, Friston and colleagues (Friston et al., 2000) introduced a linear feedback model of the CBF response. In this model, an increase in neural activity *u(t)* (equal to zero at rest) leads to an increase in the concentration of a flow-inducing signal *s* through the first order differential equation $\dot{\boldsymbol{s}} = \varepsilon \boldsymbol{u}(\boldsymbol{t}) - \boldsymbol{k}_s \boldsymbol{s} - \boldsymbol{g}_f (\boldsymbol{f} - 1)$, where ε is the neuronal efficacy, $\boldsymbol{k}_s$ is the rate constant for signal decay, and $\boldsymbol{g}_f$ is the gain constant for an auto-regulatory feedback term that drives the CBF back to its baseline value. The flow-inducing signal then leads to an increase in CBF through the relation $\dot{\boldsymbol{f}} = \boldsymbol{s}$ where *f* denotes CBF normalized by its baseline value. The form of the model was motivated by observations of an approximate linearity of the CBF response to stimulus (Miller et al., 2001), reports of post undershoots in CBF responses (Irikura et al., 1994), and the existence of vasomotion with a period of about 10 seconds (Mayhew et al., 1996). The two first order equations may be combined to yield the overall second order equation for flow $\ddot{f} + k_s \dot{f} + g_f (f - 1) = \varepsilon u(t)$. The properties of the equation can be understood by considering the impulse response $f_\delta(t) = 1 + \frac{\varepsilon}{\omega_0} \exp(-k_s t/2) \sin \omega_0 t$ where $\omega_0 = \sqrt{g_f - k_s^2/4}$ is the resonant frequency. As the impulse response is a constant term plus a damped sinusoid, the speed of the response depends on the resonant frequency. In order for the baseline CBF level to speed up the impulse response in this model, the primary effect of a decrease in CBF must be to increase the resonant frequency, either through decreasing the decay constant k_s or increasing the feedback gain constant g_f. Within the framework of the model, however, there is not a clear link between the values of the decay and gain constants and the baseline vascular state.

In this paper, we present an extension of Friston's model that explicitly models the contribution of the baseline vascular state to the dynamic CBF response. We refer to the modified model as the *arteriolar compliance model* because it models the link between neural activity and changes in the compliance of the arterioles. The motivation and basic form of the model are presented in the Theory section. Numerical simulations are then used to demonstrate the predictive capabilities of the model.

2.3 Theory

2.3.1 Nonlinear dependence of radius on compliance

The arteriolar compliance model is based on the following simplified picture. An arteriole experiences both intravascular pressure from the flowing blood and extravascular forces from the surrounding tissue and extracellular fluid. The intravascular and extravascular forces are balanced by circumferential stresses within the arteriole wall. There is an active stress component due to the vascular smooth muscle and a passive stress component due to connective tissues. The active and passive components act as two springs in parallel and together determine the overall compliance of the arteriole. With the assumption of constant external forces, the radius of the arteriole increases with its overall compliance. By analogy with a spring, the more compliant the arteriole, the more the vessel wall can stretch under a constant force.

Over the operating range of the arteriole, the relative contributions of the active and passive components to the overall compliance vary. Near or below the normal operating radius of the arteriole, most of the total stress is taken up by the muscle, so that the muscle compliance determines the overall compliance. As the radius saturates towards its maximum value, the muscle stress decreases while the passive stress increases exponentially (Davis et al., 1989; Lash et al., 1991). At these larger radii, most of the stress is taken up by the passive component, which then determines the overall compliance. Thus, there is a nonlinear dependence of total compliance on muscular compliance. This results in a nonlinear dependence of radius on muscular compliance that plays a critical part in explaining the dependence of the CBF dynamics on baseline CBF. Examples of the relations between stress, compliance and radius are shown in Figures 1a and 1b for a 35 micron radius arteriole where the fraction λ of the total stress at rest taken up by the passive component is equal to 0.15 and the maximum radius is 1.3 times the resting radius, consistent with typical values from (Davis et al., 1989; Lash et al., 1991).

In the Appendix, we formalize the above arguments and derive an expression (Eqn A10) for the nonlinear relation between the arteriolar radius and smooth muscle compliance. An example of this relation is shown in Figure 1c.

2.3.2 Link between neural activity and compliance

Although the precise mechanisms of neurovascular coupling are still poorly understood, it is generally thought that neural activity leads to an increase in the concentration of a number of vasoactive agents, such as nitric oxide, potassium ions, and adenosine (Attwell et al., 2002;

D'Esposito et al., 2003; Iadecola, 2004). These agents affect muscular compliance by modulating the phosphorylation of myosin light chains (MLC) in the vascular smooth muscle cells (VSMC) either directly (e.g. through cyclic adenosine monophosphate (cAMP)) or through changes in the intracellular concentration of calcium (Davis et al., 1999; Murray, 1990; West et al., 2003). The kinetics of the pathway from neural activity to compliance are complex and still an area of active investigation, and so our approach is to construct the simplest model consistent with the experimental data. This is a second order model consisting of a first stage relating neural activity to changes in a vasoactive signal and a second stage relating this signal to changes in muscular compliance.

The first stage approximates the complex path from neural activity to intermediate agents, such as nitric oxide and adenosine, onto final signaling agents, such as calcium, cAMP, cyclic guanine monophosphate (cGMP) and associated protein kinases (Davis et al., 1999; Murray, 1990; Somlyo et al., 1994; West et al., 2003). We lump the effects of the various vasodilatory and vasoconstrictive agents into a single vasoactive signal *s*, and adopt the first order form of Friston's model to approximate the relation between neural activity and the change in the signal *s* as

$$\dot{\boldsymbol{s}} = \varepsilon \boldsymbol{u}(\boldsymbol{t}) - \boldsymbol{k}_s \boldsymbol{s} - \boldsymbol{g}_f (\boldsymbol{r}^{\gamma} - 1) \qquad [1]$$

with the flow feedback term rewritten in terms of the normalized radius $\boldsymbol{r} = \boldsymbol{R} / \boldsymbol{R}_0$ where $\boldsymbol{R}_0$ is the baseline radius and the exponent γ is 2 for plug flow and 4 for laminar flow. Blood flow in arterioles is well described by a laminar flow model, whereas blood flow in capillaries can vary between plug and laminar flow depending on the length of the vessel and the relative distribution and deformation of red blood cells (Fung, 1997). The feedback term models mechanisms that attempt to drive the system back to its baseline state, such as the action of stretch-mediated receptors in the vessel wall leading to an increase in the influx of calcium into the VSMC (Davis et al., 1999; Martinez-Lemus et al., 2003). It is important to note that at rest the vasoactive signal *s* is equal to zero, reflecting the balance between competing vasodilatory and vasoconstrictive signals. At the onset of activation, the concentration of vasodilatory agents (e.g. nitric oxide and cGMP) increases, leading to an increase in *s*. As the flow increases, the vasoconstrictive effects (e.g. influx of calcium) rise due to the feedback term and eventually balance the vasodilatory effects, so that *s* decreases. In the case of sustained activation this leads to a new steady state with *s* again equal to zero. Upon the cessation of activation, the vasoactive signal decreases, becoming initially negative as the vasodilatory effects decrease, before increasing back to zero when the vessel has returned to its baseline radius. Examples of these dynamics are shown in Figure 2a.

In the second stage, an increase in *s* decreases the concentration of phosphorylated MLC, leading to a decrease in active muscle stress (Yang et al., 2003) and hence an increase in muscle compliance. Approximating this with first order kinetics yields the relation

$$\dot{c}_M = s \qquad [2]$$

where $c_M = C_M / C_{M,0}$ denotes normalized compliance with baseline value $C_{M,0}$. Combining Eqns 1 and 2 yields

$$\ddot{c}_M + k_s \dot{c}_M + g_f \left(r(c_M)^{\gamma} - 1 \right) = \varepsilon u(t) \qquad [3]$$

where the notation $r(c_M)$ indicates that normalized radius is a function of normalized muscle compliance.

2.3.3 Properties of the compliance model

The model presented above is clearly a simplified view of the underlying mechanisms. The question is whether such a simple model can explain the observed changes in the HDR with aging and induced changes in baseline CBF. Because of the nonlinear nature of the model, its properties are most readily explored using numerical simulations as described in the Methods and Results sections. However, we can gain useful insight into the model dynamics by linearizing about the equilibrium point $c_M = 1$ (Wilson, 1999). To facilitate this process, we first approximate the nonlinear relation between radius and muscular compliance by the exponential function

$$R \approx R_{\max}\left(1 - a_1 \exp\left(-a_2 C_M\right)\right) \qquad [4]$$

where $R_{\max}$ is the maximum radius and a_1 and a_2 are constants obtained by fits to the nonlinear relation. An example of this approximation is shown in Figure 1c. Substitution of this approximation into Eqn 3 yields the nonlinear second order differential equation

$$\ddot{c}_M + k_s \dot{c}_M + g_f \left(\left(1 - a_1 \exp(-a_2 C_{M,0} c_M)\right)^{\gamma} R_{\max}^{\gamma} / R_0^{\gamma} - 1\right) = \varepsilon u(t) \qquad [5]$$

Linearization about the equilibrium point, then leads to the second order linear differential equation

$$\ddot{c}_M + k_s \dot{c}_M + \gamma g_f a_1 a_2 R_{\max}^{\gamma} R_0^{-1} C_{M,0} \exp(-a_2 C_{M,0}) \left(c_M - 1\right) = \varepsilon u(t) \qquad [6]$$

The effective feedback gain and impulse response associated with the linear equation are

$$g_{eff} = \gamma g_f a_1 a_2 R_{\max}^{\gamma} R_0^{-1} C_{M,0} \exp(-a_2 C_{M,0}) \quad \text{and} \qquad [7]$$

$$c_{M,\delta}(t) = 1 + \frac{\varepsilon}{\omega_{eff}} \exp(-k_s t / 2) \sin \omega_{eff} t \qquad [8]$$

respectively, with resonant frequency $\omega_{eff} = \sqrt{g_{eff} - k_s^2/4}$. With hypocapnia both R_0 and $C_{M,0}$ decrease with baseline CBF, so the feedback gain and resonant frequency increase as baseline CBF decreases. As a result, the linearized equation exhibits the property that the dynamics of the impulse response speed up with a hypocapnia-induced decrease in baseline CBF. The importance of the nonlinear relation between radius and compliance can be appreciated by considering a linear relation of the form $\boldsymbol{R} = \boldsymbol{b}_1\boldsymbol{C}_M + \boldsymbol{b}_2$. With the linear form, the effective gain is $\boldsymbol{g}_{eff} = \gamma \boldsymbol{g}_f \boldsymbol{b}_1 / \left(\boldsymbol{b}_1 + \boldsymbol{b}_2 / \boldsymbol{C}_{M,0}\right)$, which decreases with lower values of baseline muscular compliance and CBF.

With age-related reductions in CBF and vascular compliance, the maximal radius $\boldsymbol{R}_{\max}$, initial radius $\boldsymbol{R}_0$ and baseline total compliance all decrease, reflecting an increase in the passive stress fraction (Hajdu et al., 1990). With these changes, we find empirically that the constant terms $\boldsymbol{a}_1$ and $\boldsymbol{a}_2$ also decrease (e.g. calculations used for Fig. 3). This leads to a decrease in the feedback gain, because the term $\boldsymbol{a}_1\boldsymbol{a}_2\boldsymbol{R}_{\max}^{\gamma}\boldsymbol{C}_{M,0}$ tends to decrease more quickly than the term $\boldsymbol{R}_0^{-1}\exp\left(-\boldsymbol{a}_2\boldsymbol{C}_{M,0}\right)$ increases.

The steady-state response of the compliance model can be obtained by setting the derivatives in Eqn 3 equal to zero and keeping in mind the saturation of the radius. The steady-state fractional change in CBF is then given by

$$\boldsymbol{f}_{SS} - 1 = \begin{cases} \varepsilon \boldsymbol{u} / \boldsymbol{g}_f & \textbf{\textit{for}}\ \boldsymbol{R}_0\left(1 + \varepsilon \boldsymbol{u} / \boldsymbol{g}_f\right)^{1/\gamma} \le \boldsymbol{R}_{\max} \\ \left(\boldsymbol{R}_{\max} / \boldsymbol{R}_0\right)^{\gamma} - 1 & \textbf{\textit{otherwise}} \end{cases} \qquad [9]$$

where the subscript *SS* denotes steady-state. Thus, the model predicts that the fractional change in CBF is linearly related to the neural activity when the operating range of the vessel is such that its vessel radius is always less than the maximal radius. If the baseline CBF is greatly elevated, the fractional change in CBF can be limited by the inability of the arteriole to expand beyond its maximum radius.

2.3.4 Balloon Model

The compliance model provides the link between neural activity and CBF. The BOLD response depends not only on dynamic changes in CBF but also on changes in cerebral blood volume (CBV) and the cerebral metabolic rate of oxygen (CMRO$_2$). We use the balloon model with viscoelastic terms to model the dynamic relation between CBF, CBV, and $CMRO_2$ and to determine the total volume of deoxyhemoglobin and its impact on the magnetic resonance signal (Buxton et al., 1998; Obata et al., 2004)}. A summary of the form of the balloon model used in this paper is provided in the Appendix.

2.4 Methods

2.4.1 Modeling of carbon dioxide experiments

Numerical simulations were used to test the predictive capability of the compliance model. To demonstrate the effects of baseline CBF changes, we modeled the carbon dioxide experiments described in (Cohen et al., 2002). The results of that study show good qualitative agreement with those of a similar human study by (Kemna et al., 2001) and an animal study by (Matsuura et al., 2000). We assumed normocapnic parameter values for baseline venous volume fraction, oxygen extraction fraction, and Grubb's law constant of $\boldsymbol{V}_0 = 0.025$, $\boldsymbol{E}_0 = 0.4$, and $\alpha = 0.38$, respectively (An et al., 2002; Grubb et al., 1974). The normocapnic transit time was calculated from the central volume principle, $\tau_0 = \boldsymbol{V}_0 / \boldsymbol{CBF}$ (Stewart, 1894) assuming an average baseline CBF of 60 ml/min-100ml of tissue (equivalent to a flow rate of 0.01 s^{-1}) (An et al., 2002; Obata et al., 2004). The coupling constant (defined in Eqn A14) between the fractional change in CBF and the fractional change in $CMRO_2$ was assumed to be $\boldsymbol{n} = 3$ across all levels of the partial pressure of carbon dioxide ($PaCO_2$) (Davis et al., 1998; Hoge et al., 1999; Kastrup et al., 2002). We also assumed that the baseline rate of oxygen metabolism $CMRO_{2,0}$ did not vary with $PaCO_2$ (Hoge et al. 1999). In addition, we assumed that the intravascular pressure, Grubb's law constant, and flow exponent ($\gamma = 4$ corresponding to laminar flow) did not vary across conditions (summarized in Table 1).

To determine the nonlinear relationship between arteriolar radius and the muscular compliance (Eqn A10), we assumed an intravascular pressure of 45 mmHg with a normocapnic baseline arteriole radius and wall thickness of 35 and 7 microns, respectively (Fung, 1997). A reference radius, required for the definition of the circumferential strain, was selected to be half of the resting radius. The fraction λ of stress in the passive element at the resting radius was set to 0.15. It is important to note that in our model we assume that the relation between radius and muscular compliance is determined by the normocapnic parameters, with changes in carbon dioxide level leading to different initial starting points on this operating curve.

Based on previous studies relating $PaCO_2$ to baseline CBF, the baseline CBF values under hypercapnia and hypocapnia were estimated to be 130% and 80%, respectively, of the normocapnic baseline value (Ito et al., 2003; Rostrup et al., 2002). For each level of $PaCO_2$, the following model parameters were adjusted from their normocapnic value to reflect the change in baseline CBF: initial radius $\boldsymbol{R}_0$, initial wall thickness $\boldsymbol{h}_0$, baseline blood volume fraction $\boldsymbol{V}_0$, baseline oxygen extraction fraction $\boldsymbol{E}_0$, baseline transit time τ_0, baseline muscular compliance $\boldsymbol{C}_{\boldsymbol{M},0}$, and baseline total compliance $\boldsymbol{C}_{\boldsymbol{TOT},0}$. The values of the adjusted parameters and details of the adjustment process are provided in Table 2. BOLD signal parameters for each $PaCO_2$ level were then determined from the adjusted values using equations presented in the balloon model appendix section.

Model simulations utilized the full form of the non-linear relation between compliance and radius, as described by Eqn A10. We constructed a lookup table to relate radius to compliance because of difficulty in inverting the closed form relation. The table was constructed with a radius step size of 0.01 micron and linear interpolation was used for values between steps. Simulation of the dynamic equations utilized a central Euler approximation of the coupled differential equations with a time step of 0.01 seconds.

In fitting the model to the carbon dioxide data, the model parameters discussed above and summarized in Tables 1 and 2 were treated as constants, while the following parameters were treated as unknowns: neuronal efficacy ε, signal decay constant $\boldsymbol{k}_s$, signal feedback constant $\boldsymbol{g}_f$, normalized maximum radius $\boldsymbol{r}_{\max} = \boldsymbol{R}_{\max} / \boldsymbol{R}_n$ where $\boldsymbol{R}_n$ is the normal operating radius corresponding to the normocapnic state, and viscoelastic time constants τ_+ and τ_-. The unknown parameters were constrained to be the same across the different carbon dioxide levels. Estimation of the unknown model parameters consisted of a two-step process. In the first step, model responses were generated over a coarse grid of parameter values with the range for each parameter shown in Table 3. The mean-squared error was then calculated between the data and the model responses, with the error at each level of $PaCO_2$ normalized by the power of the response. The parameter values that minimized the normalized mean-squared error summed over all levels were then used as initial estimates for the second step in which a constrained descent-based algorithm (fmincon function in MATLAB, Mathworks Inc., Natick, MA) was employed to obtain the final parameter estimates.

2.4.2 Modeling of aging effects

To model the effects of an age-related reduction in vascular compliance, we set the model parameters for the young response equal to those of the normocapnic condition described in the previous section. For the aged response, we assumed a decrease of 20 percent in the baseline CBF and increased the fraction λ of passive stress at rest from 0.15 to 0.25 of the total stress to reflect the reduction in the elasticity of the arteriolar wall resulting from the increase in the less distensible collagen and basement membrane components (Hajdu et al., 1990; Riddle et al., 2003). Initial radius $\boldsymbol{R}_0$, baseline blood volume fraction $\boldsymbol{V}_0$, and baseline transit time τ_0 were adjusted to reflect the change in baseline CBF as described in Table 2. The baseline oxygen extraction fraction $\boldsymbol{E}_0$ was held constant with age, consistent with studies showing that the baseline rate of oxygen metabolism $\mathrm{CMRO}_{2,0}$ mirrors the age-related CBF decrease (Leenders et al., 1990; Pantano et al., 1984). The coupling constant between changes in CBF and CMRO_2 was assumed to be independent of age. The wall thickness was set to 20% of the resting radius, reflecting the assumption that the ratio of wall thickness to radius does not change with age. As shown in Figure 3a, these parameter changes result in an upward and leftward shift of the total stress versus radius curve, as compared to the young curve. Reflecting this shift, the baseline total compliance $\boldsymbol{C}_{\boldsymbol{TOT},0}$ exhibits an age-related decrease (see Table 2). The baseline muscular compliance $\boldsymbol{C}_{\boldsymbol{M},0}$, however, shows an age-related increase since the muscle component accounts for a smaller fraction of the total stress in the aged state as compared to the young state. The model simulations for the aged state were performed using these adjusted parameters and the estimated model parameters obtained from the carbon dioxide data. In other words, it was assumed that the neuronal efficacy ε, signal decay constant k_s, signal feedback constant $\boldsymbol{g}_{\boldsymbol{f}}$, normalized maximum radius $\boldsymbol{r}_{\max} = \boldsymbol{R}_{\max} / \boldsymbol{R}_{\boldsymbol{n}}$ where the normal operating radius $\boldsymbol{R}_{\boldsymbol{n}}$ is equal to the age-adjusted $\boldsymbol{R}_0$, and viscoelastic time constants τ_+ and τ_- did not change with age.

2.5 Results

As shown in Figure 2d, the simulated BOLD responses show good agreement with the data from the carbon dioxide experiments. Correlation of the model responses with the data yielded a correlation coefficient of 0.99. With hypercapnia the overall BOLD response is slowed, exhibiting an increase in the temporal width, a decrease in the peak amplitude, a reduction in the post-stimulus undershoot, and an increase in the rise time with respect to the normocapnic response. In contrast, hypocapnia leads to a decrease in the temporal width, an increase in the peak amplitude, and a decrease in the rise time. The model responses underestimate the amplitudes of both the peak of the response and the post-undershoot response for the normocapnic data. This partly reflects the fact that the viscoelastic time constants were maintained constant across conditions.

The compliance model parameters describing neuronal efficacy ε, signal decay constant k_s, and flow dependent feedback gain $\boldsymbol{g_f}$ were estimated to be 0.57 s^{-2}, 1.38 s^{-1}, and 0.36 s^{-2}, respectively. These values are similar to the corresponding average values of 0.54 s^{-2}, 0.65 s^{-1}, and 0.41 s^{-2} reported for the linear feedback model in (Friston et al., 2000). The balloon model viscoelastic time constants were found to be 0.43 s during inflation and 11.59 s during deflation. The normalized maximum radius was estimated to be 1.30.

It is important to stress that the model responses were obtained with the signal decay and feedback gain parameters held constant across the levels of carbon dioxide. Thus, the speeding up or slowing down of the response was due primarily to the change in baseline compliance, which then modulates the effective feedback gain (see Theory section). This is in marked contrast with the linear feedback model, which, as discussed in the Introduction, requires a change in either the signal decay or feedback gain parameter in order to slow down or speed up the response in a manner consistent with the experimental data. In addition, although the parameters estimated for the compliance model show good agreement with those previously reported for the linear feedback model, these models are not equivalent, even for the normocapnic state. The feedback term in the compliance model exhibits a nonlinear and dynamic dependence on CBF, while the feedback term in the linear feedback model is assumed to be a constant.

A detailed examination of the various responses in Figure 2 is useful for understanding the dependence on baseline CBF. As shown in Figure 2a, the initial slopes of the vasoactive signal responses are independent of the baseline state, reflecting the fact that the signal decay and flow feedback terms in Eqn 1 are initially small so that the time derivative of the vasoactive signal is proportional to neural activity. Similarly, the initial slopes of the normalized muscle compliance curves are independent of the baseline state. In contrast, the slopes of the normalized CBF and BOLD responses in Figure 2c and 2d, respectively, exhibit a baseline dependence that reflects the non-linear relation between the radius and smooth muscle compliance described by equation A10. To better understand this dependence, we consider the derivative $\boldsymbol{dR/dC_M}$ of radius with respect to muscular compliance. Due to the nonlinear relation between radius and compliance, this derivative also exhibits a nonlinear dependence on muscular compliance, as shown in Figure 1d. At lower baseline muscular compliance values, corresponding to lower baseline CBF with hypocapnia, $\boldsymbol{dR/dC_M}$ is elevated with respect to the normocapnic condition. Conversely, at higher baseline muscular compliance values, corresponding to elevated baseline CBF with hypercapnia, $\boldsymbol{dR/dC_M}$ is reduced. As a result, the same fractional change in muscular compliance under hypocapnia will result in a larger fractional changes in radius and CBF as compared to the normocapnic condition, while under hypercapnia the percent CBF change is reduced.

After its initial rise, the vasoactive signal decreases more quickly under hypocapnia and more slowly under hypercapnia. In the hypocapnic condition, the increased fractional change in CBF leads to a larger flow dependent feedback term that drives the vasoactive signal back to zero more quickly. Referring back to the insight gained from the linearization analysis, we also note that the larger feedback term corresponds to a higher resonant frequency in the linearized form of the model. In contrast, the feedback term is smaller under hypercapnia and the vasoactive signal moves more slowly toward the baseline value. Because of the slower decrease of the vasoactive signal, the normalized muscular compliance reaches a larger value in the hypercapnic condition as compared to the normocapnic and hypocapnic states. However, as shown by the curves in Figure 2c, the greater percent change in compliance does not translate into a larger percent change in CBF. Instead, the hypercapnic response exhibits the smallest percent CBF increase, reflecting the lower value of $\boldsymbol{dR/dC_M}$. The peak values of the normalized flow during normocapnia, hypocapnia, and hypercapnia are 1.95, 2.25, and 1.60, respectively. For comparison, we find from equation 9 that the normocapnic and hypocapnic normalized steady state flows are both given by $1+\varepsilon \boldsymbol{u}/\boldsymbol{g_f} = 2.6$ (assuming a step input $u = 1$), while the hypercapnic steady-state response is given by $\left(\boldsymbol{R}_{\max}/\boldsymbol{R}_0\right)^{\gamma} = 2.2$

After the stimulus has ended, the vasoactive signal becomes negative, leading to a decrease in muscular compliance. Because of the larger flow feedback term, the hypocapnic vasoactive signal and compliance responses resolve the most quickly. This is also reflected in the CBF and BOLD responses. The simulated CBF responses under normocapnia and hypocapnia exhibit a post-stimulus undershoot that is not observed in the slower response under hypercapnia. The post-stimulus undershoot in the hypercapnic BOLD response is minimal, indicating a similarity between the time courses of the post-stimulus CBF and CBV responses (Buxton et al., 1998; Mandeville et al., 1999). In contrast, the post-stimulus undershoots in the hypocapnic and normocapnic BOLD responses reflect the contributions of the CBF undershoots and the relative mismatch of the CBF and CBV responses.

The stress versus radius curves for young versus aged conditions are shown in Figure 3a. The total stress is slightly increased in the aged condition, reflecting a reduction in the normal resting radius and wall thickness with intravascular pressure held constant between conditions. The passive stress curves exhibit an age-related shift similar to that described in (Hajdu et al., 1990), with a smaller maximum radius and a larger fraction of passive stress in the aged state. The increased passive fraction makes the vessel less responsive to changes in muscular compliance. This is reflected in the curves of Figure 3b showing a downward shift in the derivative $\boldsymbol{dR / dC_M}$ with aging. The age-related shift results in a smaller increase in radius and CBF for a given increase in muscular compliance. The smaller increase in CBF leads to a smaller flow-dependent feedback term and hence a slower response in the aged state. These effects are reflected in the CBF responses of Figure 3c, with the aged response exhibiting a smaller amplitude and slower dynamics as compared to the young response. The BOLD response shown in Figure 3d inherits these features. Additional numerical simulations (not shown), indicate that simply lowering baseline CBF without also increasing the passive stress fraction does not significantly slow down the responses, because this merely shifts the operating curve (stress vs. radius) of the arteriole as opposed to changing the shape of the curve. In addition, as described in the Methods section, the simulations were performed with the assumption that CMRO$_2$ decreases with age so that the baseline oxygen extraction fraction $\boldsymbol{E}_0$ does not change with age. With the alternative assumption that CMRO$_2$ remains constant with age, $\boldsymbol{E}_0$ would increase, and the amplitude of the aged BOLD response would be greater than that of the model response shown.

2.6 Discussion

We have presented a nonlinear dynamic model linking changes in neural activity to changes in arteriolar compliance and CBF. The compliance model may be considered an extension of the linear dynamic model proposed in (Friston et al., 2000). In the present model, the vasoactive signal modulates arteriolar muscular compliance as opposed to directly modulating CBF as in the prior model. Changes in total arteriolar compliance then lead to changes in vessel radius and CBF. The total compliance is modeled as the parallel combination of an active component representing smooth muscle and a passive component representing connective tissue. This results in a nonlinear relation between radius and smooth muscle compliance. At smaller radii, the total compliance is determined primarily by the smooth muscle compliance, so that neurally induced changes in muscle compliance lead to relatively large changes in vessel radius. At larger radii, the total compliance is determined primarily by the passive component so that changes in muscle compliance are less effective at modulating the vessel radius.

Using numerical simulations, we have shown that the compliance model predicts to first order the observed changes in the temporal dynamics of the CBF and BOLD responses as a function of baseline CBF. The model also predicts the slowing down of the responses with age-related decreases in vascular compliance.

Although the compliance model in its present form provides relatively good fits to experimental observations, it is clearly a simplification of the underlying mechanisms. Further experimental and theoretical work is required to develop more accurate and complex models. For example, although the output of the compliance model is CBF, most of the currently available observations revealing baseline vascular effects use measurements of the BOLD response. This is in part because of the lower signal-to-noise ratios (SNR) exhibited by present methods for measuring CBF, as compared to methods for measuring BOLD. Detailed measurements of dynamic CBF responses as a function of baseline CBF would allow for a more direct validation of the compliance model. In addition, in-vitro studies of isolated arterioles and in-vivo studies of CBF responses in animals, using invasive methods that cannot be applied to humans, would be useful for more fully revealing the mechanisms underlying the effects of the baseline vascular state.

The current model employs a first stage linking neural activity to a vasoactive signal and a second stage linking to the vasoactive signal to changes in muscular compliance. Further development of the model would lead to more accurate descriptions of the pathways in each stage. For example, the first stage involves initial pathways from neural activity to intermediate vasoactive agents, such as nitric oxide, and secondary pathways from the intermediate agents to final signaling agents, such as calcium. Thus, the next level of model development could entail modeling the first stage as the cascade of two first order systems. A recently presented biophysical model linking calcium to muscular compliance (Yang et al., 2003; Yang et al., 2003) may provide useful insights for modifying the second stage of the compliance model. This model integrates a large body of current knowledge about the electrochemistry and chemo-mechanics of the vascular smooth muscle cell, and has been shown to fit experimental measurements of the myogenic response in isolated cerebral arterioles. In its current state the model is probably too complex (23 state variables and roughly 50 assumed constants) to robustly model dynamic responses. However, numerical simulations of the biophysical model could be useful in exploring further developments of the second stage of the compliance model. For example, the present model might be expanded to incorporate a description of the phosphorylation of the myosin light chains.

While the compliance model is the primary focus of this paper, the balloon model plays an important role in testing the predictions of the compliance model with experimental BOLD observations. Although as discussed above, CBF measurements are preferable for direct validation of the compliance model, BOLD measurements are likely to play an important role in further development of the model, due to their better SNR and temporal resolution. In addition, the widespread use of BOLD measurements in fMRI studies makes it critical to understand the effect of the baseline vascular state on the BOLD responses. In the current form of the balloon model, we have assumed a tight coupling between CBF and $CMRO_2$ (Eqn. A14) and also assumed that $CMRO_2$ does not change with carbon dioxide level. Recently, Zheng et al (Zheng et al., 2002) have proposed a dynamic model that takes into account the modulatory effect of tissue oxygenation on the coupling between CBF and oxygen delivery. The model appears to yield a better prediction of the dynamic $CMRO_2$ response to neural stimulus and also provides a prediction of the observed $CMRO_2$ response in anesthetized rats to hypercapnia. The incorporation of the dynamic oxygen delivery model may therefore improve the predictive capability of the combined compliance and balloon model presented here. A reformulation of the viscoelastic properties of the balloon model may also lead to better predictions. In fitting the results of the carbon dioxide experiments, we found that it was difficult to simultaneously fit the post-stimulus undershoot of the BOLD response under all baseline conditions (see Figure 2). A better fit may be achievable with a model that incorporates the effect of baseline CBV and venous compliance on the dynamics of the venous compartment.

In this paper we have focused on the structure of the compliance model and its ability to predict the effect of the baseline vascular state on the hemodynamic response to stimulus. The estimation of model parameters was achieved using a two-step procedure consisting of a global minimization over a coarse grid followed by a conventional descent based algorithm. This approach may not be optimal from the point of view of computational efficiency or robustness. Friston et al (Friston, 2002; Friston et al., 2003) have applied a Bayesian identification scheme to the combination of the second order linear feedback model (described in the introduction) with the balloon model. This scheme utilizes the expectation-maximization algorithm for estimating the conditional or posterior distribution of the model parameters. The inclusion of priors in the estimation procedure enables robust and rapid convergence of the estimation process. In addition, the conditional densities provided by a Bayesian scheme enable inference about the dependencies between different model parameters. It is likely, therefore, that the application of a Bayesian scheme to the compliance model would improve the robustness of the estimation process and lead to a better understanding of the interdependence and relative importance of the different model parameters. Finally, an extension of the Bayesian framework to examine interactions among different brain regions has recently been presented in the form of dynamic causal models (Friston et al. 2003). Incorporation of the compliance model into the current dynamic causal model structure could prove useful in examining the effect of the baseline vascular state on the effective connectivity between brain areas.

Acknowledgements

This work was funded by a Biomedical Engineering Research Grant from the Whitaker Foundation. We thank Khaled Restom, Kamil Uludag, Matt Cronin, and Rick Buxton for helpful discussions.

Publication Acknowledgements

Chapter 2, in full, is a reprint of the material as it appears in:

Behzadi, Y., and Liu, T.T., (2005) An arteriolar compliance model of the cerebral blood flow response to neural stimulus. *Neuroimage*. 25(4), 1100-1111.

The dissertation author was the primary author of these papers. I would like to acknowledge my co-author Professor Thomas T. Liu.

2.7 Appendix

2.7.1 Radius and Muscular Compliance

In this section we show that there is a nonlinear relation between arteriolar radius and the compliance of the vascular smooth muscle. We begin with the force balance equation for a cylindrical thick walled vessel

$$\boldsymbol{R}\boldsymbol{P}_i - (\boldsymbol{R}+\boldsymbol{h})\boldsymbol{P}_e = (\sigma_M + \sigma_P + \sigma_V)\boldsymbol{h} \qquad \text{[A1]}$$

where $\boldsymbol{P}_i$ and $\boldsymbol{P}_e$ are the intravascular and extravascular pressures, respectively; σ_M, σ_P, and σ_v are muscular, passive, and viscoelastic stress terms, respectively; and *h* is the wall thickness (Ursino, 1991). We assume that the vessel wall is incompressible so that the wall thickness satisfies the constraint

$$\boldsymbol{h} = -\boldsymbol{R} + \sqrt{\boldsymbol{R}^2 + 2\boldsymbol{R}_0\boldsymbol{h}_o + \boldsymbol{h}_o^2} \qquad \text{[A2]}$$

where $\boldsymbol{R}_0$ and $\boldsymbol{h}_0$ are the initial values of the inner radius and wall thickness. With this relationship the vessel wall gets thinner as the radius increases. To obtain a steady-state relation between compliance and radius, we may neglect the viscoelastic stress term, which is proportional to the rate of change of the radius. Because of the lack of data on the extravascular pressure exerted by the surrounding tissue, we neglect this term to simplify our presentation. Choosing a constant value for this term would not change the overall approximation that we derive.

With the above assumptions the total stress can be expressed as

$$\sigma_{Tot} = \sigma_P + \sigma_M = \frac{\boldsymbol{P}_i}{\boldsymbol{h}}\boldsymbol{R}\,. \qquad \text{[A3]}$$

This is analogous to two springs acting in parallel in which the overall stress is the sum of the stresses in each individual element, and the individual strains are equal to the total strain. In contrast, two springs in series would experience equal stresses and the overall strain would be equal to the sum of the individual strains at each spring (Fung, 1994).

The total compliance of the arteriole is defined as

$$\boldsymbol{C}_{\boldsymbol{Tot}} = \frac{\boldsymbol{E}_{\boldsymbol{Tot}}}{\sigma_{\boldsymbol{Tot}} - \sigma_{\boldsymbol{Tot},\mathrm{Ref}}} \qquad [A4]$$

where $\sigma_{\boldsymbol{Tot}}$ is defined as a function of radius in Eqn A3, $\sigma_{\boldsymbol{Tot},\mathrm{Ref}}$ is the stress at a reference radius $\boldsymbol{R}_{\boldsymbol{ref}}$; and the Lagrangian finite strain term is $\boldsymbol{E}_{\boldsymbol{Tot}} = \frac{1}{2}\left(\frac{\boldsymbol{R}^2}{\boldsymbol{R}_{\boldsymbol{ref}}^2} - 1\right)$ (Fung, 1993). The reference radius is chosen to be smaller than the lowest radius of interest so that all stresses and strains are positive. Because the total stress is the sum of the passive and muscle stresses, the total compliance may also be expressed as the parallel combination

$$\boldsymbol{C}_{\boldsymbol{Tot}} = \frac{\boldsymbol{C}_{\boldsymbol{P}}\boldsymbol{C}_{\boldsymbol{M}}}{\boldsymbol{C}_{\boldsymbol{P}} + \boldsymbol{C}_{\boldsymbol{M}}} \qquad [A5]$$

of a muscle compliance term C_M and passive compliance term C_P. These are defined as

$$\boldsymbol{C}_{\boldsymbol{M}} = \frac{\boldsymbol{E}_{\boldsymbol{Tot}}}{\sigma_{\boldsymbol{M}} - \sigma_{\boldsymbol{M},\boldsymbol{ref}}}\ , \ \boldsymbol{C}_{\boldsymbol{P}} = \frac{\boldsymbol{E}_{\boldsymbol{Tot}}}{\sigma_{\boldsymbol{P}} - \sigma_{\boldsymbol{P},\boldsymbol{ref}}} \qquad [A6]$$

where $\sigma_{\boldsymbol{M},\mathrm{Ref}}$ and $\sigma_{\boldsymbol{P},\mathrm{Ref}}$ are the respective stresses at the reference radius and $\sigma_{\boldsymbol{Tot},\mathrm{Ref}} = \sigma_{\boldsymbol{P},\mathrm{Ref}} + \sigma_{\boldsymbol{M},\mathrm{Ref}}$. With these definitions and the relation in A3, Equations A4 and A5 are mathematically equivalent. Note that in the parallel combination of compliances in A5, the smaller compliance dominates the total compliance. This is analogous to the less compliant spring dominating the overall compliance when two springs are in parallel.

From Eqns A3 and A6, we can express muscular compliance as a function of the vessel radius and passive stress

$$C_M = \frac{E_{Tot}}{P_i\left(\frac{R}{h} - \frac{R_{ref}}{h_{ref}}\right) - \left(\sigma_P - \sigma_{P,\mathrm{Re}f}\right)} \quad . \qquad \text{[A7]}$$

It has been shown that passive stress is well modeled as an exponential function of radius

$$\sigma_P = \sigma_{P,0}\exp(k_P R) \qquad \text{[A8]}$$

where $\sigma_{P,0}$ and k_P are empirical constants (Fung, 1997). Estimation of these constants is based on the following observations: (a) the ratio of the stress in the elastic to the muscle element as a function of radius is conserved across various orders of the arteriole tree; (b) at the normal operating point radius R_n, 80-90% of the total tension is within the muscle element; and (c) nearly all the stress is exerted by the passive element when the vessel is at its maximum radius $R_{\max}$ (Davis et al., 1989; Lash et al., 1991). Application of the boundary conditions at R_n and $R_{\max}$ in conjunction with Eqn A3 for the total stress yields

$$\sigma_P = \frac{P_i\lambda R_n}{h_n}\left(\frac{R_{\max}h_n}{\lambda R_n h_{\max}}\right)^{\left(\frac{R-R_n}{R_{\max}-R_n}\right)} \qquad \text{[A9]}$$

where λ is the fraction of total stress in the passive element at R_n, and h_n and $h_{\max}$ are the vessel wall thickness at R_n and $R_{\max}$, respectively. Substitution of Eqn A9 into Eqn. A7 yields an expression for muscular compliance as a function of radius

$$C_M = \frac{\frac{1}{2}\left(\frac{R^2}{R_{ref}^2} - 1\right)}{P_i\left(\frac{R}{h} - \frac{R_{ref}}{h_{ref}}\right) - \frac{P_i\lambda R_n}{h_n}\left(\left(\frac{R_{\max}h_n}{\lambda R_n h_{\max}}\right)^{\left(\frac{R-R_n}{R_{\max}-R_n}\right)} - \left(\frac{R_{\max}h_n}{\lambda R_n h_{\max}}\right)^{\left(\frac{R_{ref}-R_n}{R_{\max}-R_n}\right)}\right)} \qquad \text{[A10]}$$

Assuming an intravascular pressure of 45 mmHg with a normal operating point radius and wall thickness of 35 and 7 microns; respectively, we use Equation A10 to plot the relation between radius and muscle compliance in Figure 1c. Additionally, the reference radius was selected to be half of the resting radius with λ and $\boldsymbol{R}_{\max}/\boldsymbol{R}_{\boldsymbol{n}}$ set to 0.15 and 1.3, respectively. This relation is fairly well approximated by the exponential form $\boldsymbol{R} = \boldsymbol{R}_{\max}\left(1 - \boldsymbol{a}_1 \boldsymbol{e}^{-\boldsymbol{a}_2 \boldsymbol{C}_{\boldsymbol{m}}}\right)$, also shown in the Figure 1c.

2.7.2 Balloon Model

In the balloon model with viscoelastic effects, the venous compartment is treated as a distensible balloon (Buxton et al., 1998). The flow into the balloon is determined by the compliance model, while the flow out of the balloon is modeled as

$$\boldsymbol{f}_{\boldsymbol{out}}(\boldsymbol{v}) = \boldsymbol{v}^{1/\alpha} + \tau_{\boldsymbol{v}} \dot{\boldsymbol{v}} \qquad \text{[A11]}$$

where *v* denotes the venous volume normalized by its initial value, $\tau_{\boldsymbol{v}}$ is the viscoelastic time constant (equal to τ_+ and τ_- during inflation and deflation, respectively), and α is an empirical constant that determines the steady state power law relation between flow and volume (Buxton et al., 1998; Grubb et al., 1974). The flow and volume dynamics follow the mass conservation relation

$$\tau_0 \dot{\boldsymbol{v}} = \boldsymbol{f} - \boldsymbol{f}_{\boldsymbol{out}}(\boldsymbol{v}) \qquad \text{[A12]}$$

where τ_0 is the mean transit time to traverse the venous compartment at rest.

The equation for mass conservation of deoxyhemoglobin in the balloon is

$$\tau_0 \dot{\boldsymbol{q}} = \boldsymbol{f} \frac{\boldsymbol{E}(\boldsymbol{f}, \boldsymbol{E}_0)}{\boldsymbol{E}_0} - \boldsymbol{f}_{\boldsymbol{out}}(\boldsymbol{v}) \frac{\boldsymbol{q}}{\boldsymbol{v}} \qquad \text{[A13]}$$

where q is the total deoxyhemoglobin content normalized by its initial value, $\boldsymbol{E}_0$ is the net extraction fraction of oxygen at rest, and $\boldsymbol{E}(\boldsymbol{f}, \boldsymbol{E}_0)$ is the extraction fraction as a function of flow and $\boldsymbol{E}_0$. An expression for $\boldsymbol{E}(\boldsymbol{f}, \boldsymbol{E}_0)$ is obtained by assuming a linear coupling

$$n = \frac{\Delta CBF / CBF_0}{\Delta CMRO_2 / CMRO_{2,0}} = \frac{f-1}{m-1} \qquad [A14]$$

between the fractional change in CBF and the fractional change in CMRO$_2$, where n is an empirical coupling constant and m is CMRO$_2$ normalized by its initial value (Buxton, 2002). The relation between CBF and CMRO$_2$ is $CMRO_2 = E \cdot C_A \cdot CBF$ where C_A is the arterial oxygen concentration. This may be written in normalized quantities as $E = E_0 \frac{m}{f}$. Combining this expression with Eqn A14 yields

$$E(f, E_0) = E_0 \frac{f+n-1}{nf} \qquad [A15]$$

which permits us to rewrite Eqn A13 as

$$\tau_0 \dot{q} = \frac{f+n-1}{n} - f_{out}(v)\frac{q}{v} \qquad [A16]$$

The BOLD signal change as a function of normalized volume and deoxyhemoglobin is

$$\Delta S / S_0 = V_0\left[(k_1 + k_2)(1-q) - (k_2 + k_3)(1-v)\right] \qquad [A17]$$

where V_0 is the resting blood volume fraction (Obata et al., 2004). The first constant term $k_1 = 4.3 v_0 E_0 TE$ where TE is the echo time of the sequence and $v_0 = 40.3 \cdot (B_0 / 1.5)\ \mathrm{s}^{-1}$ is a magnetic field (B_0) dependent frequency offset. The second constant term $k_2 = \beta r_0 E_0 TE$ where $\beta = S_E / S_I$ is the intrinsic ratio of blood to tissue signals at rest and r_0 is the slope of the intravascular relaxation rate $R^*_{2,I}$ versus the extraction fraction E (Li et al., 1998). The blood and tissue signals are defined as $S_E = S_{E,0} \exp(-TE / T^*_{2,E})$ and $S_I = S_{I,0} \exp(-TE / T^*_{2,I})$, respectively, where T^*_{2I} and T^*_{2E} are the resting intravascular and extravascular transverse relaxation times and S_{E0} and S_{EI} are the effective spin densities. For this paper we assume average values of $\boldsymbol{T}^{*}_{2,\boldsymbol{E}} = 25$ ms and $\boldsymbol{T}^{*}_{2,\boldsymbol{I}} = 12.8$ ms at 7 Tesla (Yacoub et al., 2001) and also assume that the effective spin densities are equal. In vitro measurements have shown that $\boldsymbol{r}_0$ exhibits a quadratic dependence on field strength (Silvennoinen et al., 2003), so that we may calculate its value as a function of field strength as $\boldsymbol{r}_0 = 25.0 \cdot \left(\boldsymbol{B}_0 / 1.5\right)^2$ where $25.0\,\mathrm{s}^{-1}$ is the measured in-vivo value at 1.5 T (Li et al., 1998; Obata et al., 2004). Finally, the third constant term is defined as $\boldsymbol{k}_3 = \beta - 1$.

2.8 Figures and Tables

Table 2.1. Model parameters that were held constant across all model simulations.

Parameter	Variable Name	Value
Grubb’s Constant	α	0.38
$CMRO_2$ and CBF Coupling Constant	n	3
Flow Exponent	γ	4
Intravascular Pressure (mmHg)	P_i	45

Table 2.2. Description of model parameters that were adjusted to reflect either carbon dioxide level-related or age-related changes in the normalized baseline cerebral blood flow $\boldsymbol{f}_0 = \boldsymbol{CBF}_0 / \boldsymbol{CBF}_{0,\boldsymbol{YN}}$ where $\boldsymbol{CBF}_{0,\boldsymbol{YN}}$ denotes baseline CBF for normocapnia in the young state. Initial radius is $\boldsymbol{R}_0 = \boldsymbol{R}_{0,\boldsymbol{YN}} \boldsymbol{f}_0^{1/\gamma}$ where $\boldsymbol{R}_{0,\boldsymbol{YN}}$ is the initial radius for the young normocapnic state and $\gamma = 4$ for laminar flow. The initial wall thicknesses $\boldsymbol{h}_0$ for the hypocapnic and hypercapnic states were computed using the incompressibility constraint in Eq A2, whereas the initial wall thickness for the old state was assumed to be 20% of $\boldsymbol{R}_0$. The passive stress fraction λ at rest is used to generate the stress versus radius operating curves for the young and old states. It therefore corresponds to the stress fraction for the normocapnic condition in either the young or old state. Initial muscular compliance $\boldsymbol{C}_{\boldsymbol{M},0}$ and total compliance $\boldsymbol{C}_{\boldsymbol{TOT},0}$ for each state were calculated from Equations A5 and A10 with appropriate substitutions. The resting venous volume fraction $\boldsymbol{V}_0$ was determined for each state with a Grubb's law relation $\boldsymbol{V}_0 = (0.025)\boldsymbol{f}_0^{\alpha}$. With the assumption of no change in baseline CMRO$_2$ between carbon dioxide levels, the resting oxygen fraction $\boldsymbol{E}_0$ for each state is $\boldsymbol{E}_0 = \boldsymbol{E}_{0,\boldsymbol{YN}} / \boldsymbol{f}_0$ where $\boldsymbol{E}_{0,\boldsymbol{YN}}$ denotes the young normocapnic value. Reflecting the assumed decrease in CMRO$_2$ with age, the extraction fraction for the aged state is equal to that for the young normocapnic state. The resting transit delay τ_0 in each state reflects the central volume principle $\tau_0 = \boldsymbol{V}_0 / \boldsymbol{CBF}_0$.

Parameter	Normocapnia/ Young	Hypocapnia	Hypercapnia	Old
$CBF_0 / CBF_{0,YN}$	1.0	0.8	1.3	0.8
R_0 (μm)	35.0	33.1	37.4	33.1
h_0 (μm)	7.0	7.33	6.62	6.62
λ	0.15	0.15	0.15	0.25
$C_{M,0}$ (1/mmHg)	0.012	0.011	0.014	0.013
$C_{TOT,0}$(1/mmHg)	0.00956	0.00954	0.00958	0.00856
V_0	0.025	0.023	0.028	0.023
E_0	0.4	0.5	0.31	0.4
τ_0 (s)	2.5	2.87	2.13	2.87

Table 2.3. Model parameters that were estimated with a least squares fit to the data of Cohen et al (2002). The maximum normalized radius is referenced to the normal operating radius R_n, which is defined as the normocapnic radius in either the young or old state. Details of the fitting process are described in the Methods section. Note that the simulations presented in Figures 2 and 3 use the estimated values for all conditions (i.e. these model parameters do not vary across conditions).

Parameter	Variable Name	Constrained Range	Estimated Value
Neuronal Efficacy ($1/s^2$)	ε	0-1	0.57
Decay Constant (1/s)	k_s	0-2	1.38
Feedback Gain Constant ($1/s^2$)	g_f	0-2	0.36
Viscoelastic Time Constant-inflation (s)	τ_+	0-30	0.17
Viscoelastic Time Constant-deflation (s)	τ_-	0-30	11.35
Maximum Normalized Radius	$R_{\max}/R_n$	1.2-1.30	1.30

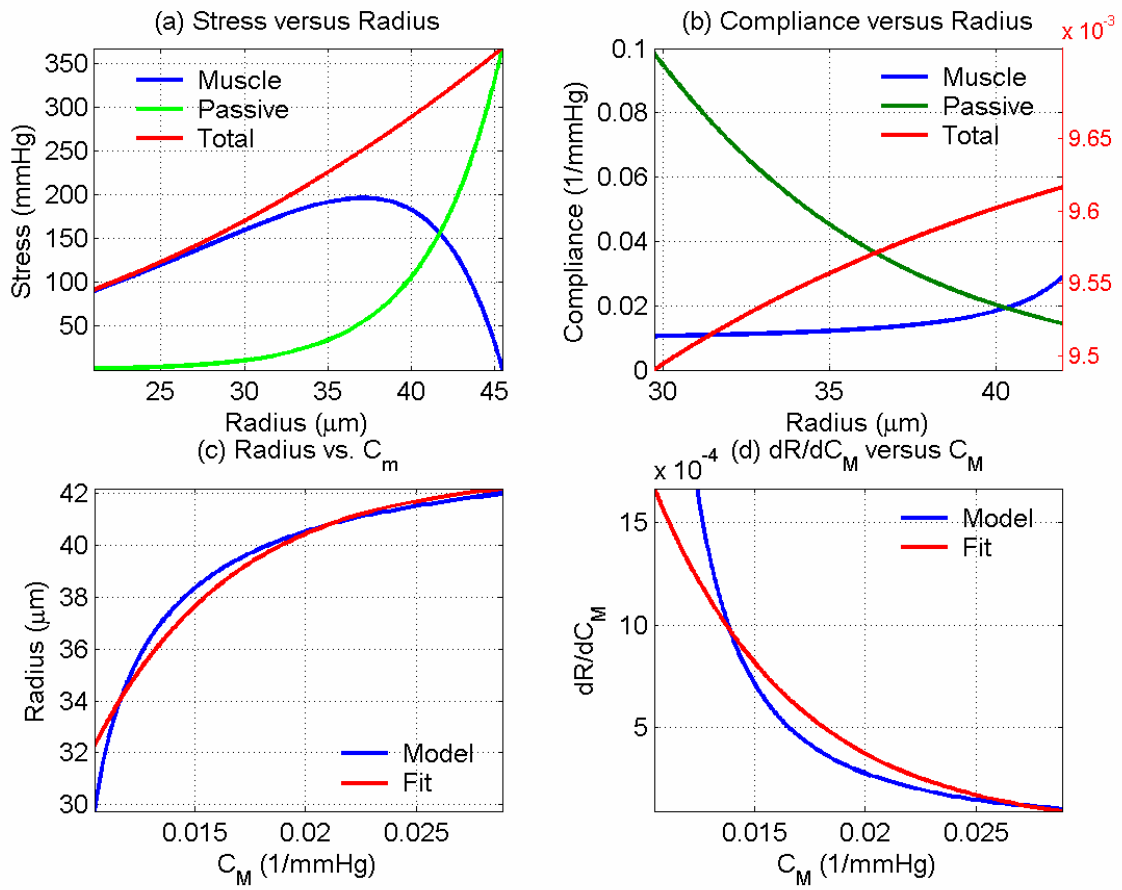

Figure 2.1. Mechanical properties of the arteriole. (a,b) Muscle, passive, and total stress and compliance versus radius. In (b), the total compliance is the parallel combination of the passive and muscle compliances, with units labeled on the righthand side of the plot. (c) Radius versus compliance and exponential fit. (d) Derivative of radius with respect to compliance. Derivative of exponential fit is also shown.

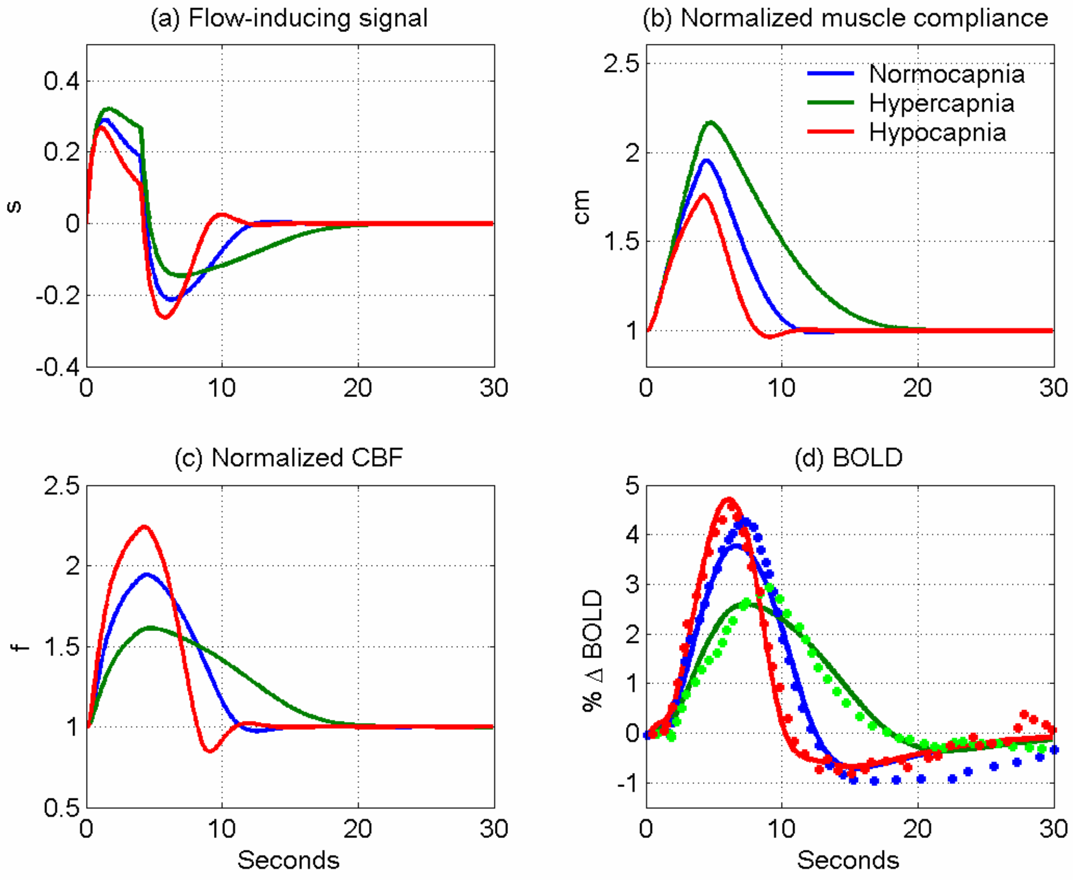

Figure 2.2. Model responses under hypocapnic, normocapnic, and hypercapnic conditions. Data from (Cohen et al., 2002) are shown by the plus symbols in panel (d)

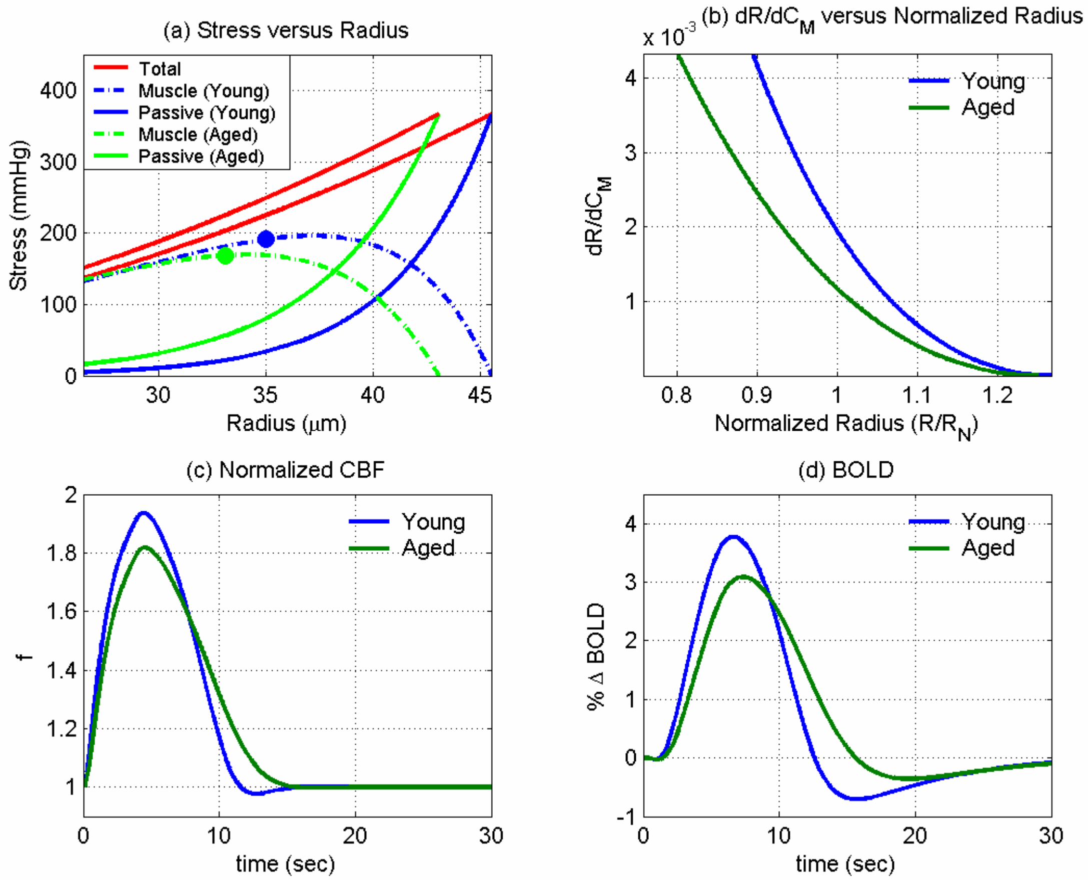

Figure 2.3. (a) Stress versus radius for young and old subject. (b) dR/dC_M versus normalized radius (c,d) Model CBF and BOLD responses.

2.9 References

An H. and Lin W. (2002) Cerebral venous and arterial blood volumes can be estimated separately in humans using magnetic resonance imaging. *Magn Reson Med*. 48, 583-588.

Ances B. M., Greenberg J. H., and Detre J. A. (2001) The effects of graded hypercapnia on the activation flow coupling response due to forepaw stimulation in alpha-chloralose anesthetized rats. *Brain Res*. 911, 82-88.

Attwell D. and Iadecola C. (2002) The neural basis of functional brain imaging signals. *Trends Neurosci*. 25, 621-625.

Bakalova R., Matsuura T., and Kanno I. (2001) Frequency dependence of local cerebral blood flow induced by somatosensory hind paw stimulation in rat under normo- and hypercapnia. *Jpn J Physiol*. 51, 201-208.

Bentourkia M., Bol A., Ivanoiu A., Labar D., Sibomana M., Coppens A., Michel C., Cosnard G., and De Volder A. G. (2000) Comparison of regional cerebral blood flow and glucose metabolism in the normal brain: effect of aging. *J Neurol Sci*. 181, 19-28.

Buckner R. L., Snyder A. Z., Sanders A. L., Raichle M. E., and Morris J. C. (2000) Functional brain imaging of young, nondemented, and demented older adults. *J Cogn Neurosci*. 12 Suppl 2, 24-34.

Buxton R. B. (2002) *Introduction to Functional Magnetic Resonance Imaging*. Cambridge University Press, Cambridge.

Buxton R. B., Miller K. L., Wong E. C., and Frank L. R. (1998) BOLD signal dynamics: the balloon model with viscoelastic effects. In: *Proc. 6th Annual Meeting ISMRM*), pp. 1401, Sydney.

Buxton R. B., Wong E. C., and Frank L. R. (1998) Dynamics of blood flow and oxygenation changes during brain activation: the balloon model. *Magn Reson Med*. 39, 855-864.

Cohen E. R., Ugurbil K., and Kim S. G. (2002) Effect of basal conditions on the magnitude and dynamics of the blood oxygenation level-dependent fMRI response. *J Cereb Blood Flow Metab*. 22, 1042-1053.

Davis M. J. and Gore R. W. (1989) Length-tension relationship of vascular smooth muscle in single arterioles. *Am J Physiol*. 256, H630-640.

Davis M. J. and Hill M. A. (1999) Signaling mechanisms underlying the vascular myogenic response. *Physiol Rev*. 79, 387-423.

Davis T. L., Kwong K. K., Weisskoff R. M., and Rosen B. R. (1998) Calibrated functional MRI: mapping the dynamics of oxidative metabolism. *Proc Natl Acad Sci USA*. 95, 1834-1839.

D'Esposito M., Deouell L. Y., and Gazzaley A. (2003) Alterations in the BOLD fMRI signal with ageing and disease: a challenge for neuroimaging. *Nat Rev Neurosci*. 4, 863-872.

D'Esposito M., Zarahn E., Aguirre G. K., and Rypma B. (1999) The effect of normal aging on the coupling of neural activity to the BOLD hemodynamic response. *NeuroImage*. 10, 6-14.

Friston K. J. (2002) Bayesian estimation of dynamical systems: an application to fMRI. *Neuroimage*. 16, 513-530.

Friston K. J., Harrison L., and Penny W. (2003) Dynamic causal modelling. *Neuroimage*. 19, 1273-1302.

Friston K. J., Mechelli A., Turner R., and Price C. J. (2000) Nonlinear Responses in fMRI: The Balloon Model, Volterra Kernels, and Other Hemodynamics. *NeuroImage*. 12, 466-477.

Fung Y. (1993) *Biomechanics: Mechanical Properties of Living Tissues*. Springer-Verlag, New York.

Fung Y. (1994) *A First Course in Continuum Mechanics*, Third edn. Prentice Hall, New Jersey.

Fung Y. C. (1997) *Biomechanics: Circulation*. Springer-Verlag, New York.

Grubb R. L., Raichle M. E., Eichling J. O., and Ter-Pogossian M. M. (1974) The effects of changes in $PaCO_2$ on cerebral blood volume, blood flow, and vascular mean transit time. *Stroke*. 5, 630 - 639.

Hajdu M. A., Heistad D. D., Siems J. E., and Baumbach G. L. (1990) Effects of aging on mechanics and composition of cerebral arterioles in rats. *Circ Res*. 66, 1747-1754.

Handwerker D. A., Ollinger J. M., and D'Esposito M. (2004) Variation of BOLD hemodynamic responses across subjects and brain regions and their effects on statistical analyses. *Neuroimage*. 21, 1639-1651.

Hoge R. D., Atkinson J., Gill B., Crelier G. R., Marrett S., and Pike G. B. (1999) Linear coupling between cerebral blood flow and oxygen consumption in activated human cortex. *Proc Natl Acad Sci U S A*. 96, 9403-9408.

Iadecola C. (2004) Neurovascular regulation in the normal brain and in Alzheimer's disease. *Nat Rev Neurosci*. 5, 347-360.

Irikura K., Maynard K. I., and Moskowitz M. A. (1994) Importance of nitric oxide synthase inhibition to the attenuated vascular responses induced by topical L-nitroarginine during vibrissal stimulation. *J Cereb Blood Flow Metab*. 14, 45-48.

Ito H., Kanno I., Ibaraki M., Hatazawa J., and Miura S. (2003) Changes in human cerebral blood flow and cerebral blood volume during hypercapnia and hypocapnia measured by positron emission tomography. *J Cereb Blood Flow Metab*. 23, 665-670.

Kashikura K., Kershaw J., Kashikura A., Zhang X., Matsuura T., and Kanno I. (2001) Hyperoxia modified activation-induced blood oxygenation level-dependent response of human visual cortex (V1): an event-related functional magnetic resonance imaging study. *Neurosci Lett*. 299, 53-56.

Kastrup A., Kruger G., Neumann-Haefelin T., Glover G. H., and Moseley M. E. (2002) Changes of cerebral blood flow, oxygenation, and oxidative metabolism during graded motor activation. *Neuroimage*. 15, 74-82.

Kemna L. J. and Posse S. (2001) Effect of respiratory CO(2) changes on the temporal dynamics of the hemodynamic response in functional MR imaging. *Neuroimage*. 14, 642-649.

Lash J. M., Bohlen H. G., and Waite L. (1991) Mechanical characteristics and active tension generation in rat intestinal arterioles. *Am J Physiol*. 260, H1561-1574.

Leenders K. L., Perani D., Lammertsma A. A., Heather J. D., Buckingham P., Healy M. J. R., Gibbs J. M., Wise R. J. S., Hatazawa J., Herold S., Beaney R. P., Brooks D. B., Spinks T., Rhodes C., Frackowiak R. S. J., and Jones T. (1990) Cerebral blood flow, blood volume and oxygen utilization: Normal values and effect of age. *Brain*. 113, 27-47.

Li D., Wang Y., and Waight D. J. (1998) Blood oxygen saturation assessment in vivo using T2* estimation. *Magn Reson Med*. 39, 685-690.

Logothetis N. K. and Wandell B. A. (2004) Interpreting the BOLD signal. *Annu Rev Physiol*. 66, 735-769.

Mandeville J. B., Marota J. J. A., Ayata C., Zaharchuk G., Moskowitz M. A., Rosen B. R., and Weisskoff R. M. (1999) Evidence of a cerebrovascular postarteriole windkessel with delayed compliance. *J Cereb Blood Flow Metab*. 19, 679-689.

Marchal G., Rioux P., Petit-Taboue M.-C., Sette G., Travere J.-M., LePoec C., Courtheoux P., Derlon J.-M., and Baron J.-C. (1992) Regional cerebral oxygen consumption, blood flow, and blood volume in healthy human aging. *Arch Neurol*. 49, 1013-1020.

Martin A. J., Friston K. J., Colebatch J. G., and Frackowiak R. S. (1991) Decreases in regional cerebral blood flow with normal aging. *J Cereb Blood Flow Metab*. 11, 684-689.

Martinez-Lemus L. A., Wu X., Wilson E., Hill M. A., Davis G. E., Davis M. J., and Meininger G. A. (2003) Integrins as unique receptors for vascular control. *J Vasc Res*. 40, 211-233.

Matsuura T., Fujita H., Kashikura K., and Kanno I. (2000) Evoked local cerebral blood flow induced by somatosensory stimulation is proportional to the baseline flow. *Neurosci Res*. 38, 341-348.

Matsuura T., Fujita H., Kashikura K., and Kanno I. (2000) Modulation of evoked cerebral blood flow under excessive blood supply and hyperoxic conditions. *Jpn J Physiol*. 50, 115-123.

Matsuura T., Kashikura K., and Kanno I. (2001) Hemodynamics of local cerebral blood flow induced by somatosensory stimulation under normoxia and hyperoxia in rats. *Comp Biochem Physiol A Mol Integr Physiol*. 129, 363-372.

Mayhew J. E., Askew S., Zheng Y., Porrill J., Westby G. W., Redgrave P., Rector D. M., and Harper R. M. (1996) Cerebral vasomotion: a 0.1-Hz oscillation in reflected light imaging of neural activity. *Neuroimage*. 4, 183-193.

Mehagnoul-Schipper D. J., van der Kallen B. F., Colier W. N., van der Sluijs M. C., van Erning L. J., Thijssen H. O., Oeseburg B., Hoefnagels W. H., and Jansen R. W. (2002) Simultaneous measurements of cerebral oxygenation changes during brain activation by near-infrared spectroscopy and functional magnetic resonance imaging in healthy young and elderly subjects. *Hum Brain Mapp*. 16, 14-23.

Mildner T., Norris D. G., Schwarzbauer C., and Wiggins C. J. (2001) A Qualitative Test of the Balloon Model for BOLD-based MR Signal Changes at 3T. *Magn Reson Med*. 46, 891-899.

Miller K. L., Luh W. M., Liu T. T., Martinez A., Obata T., Wong E. C., Frank L. R., and Buxton R. B. (2001) Nonlinear temporal dynamics of the cerebral blood flow response. *Hum Brain Mapp*. 13, 1-12.

Murray K. J. (1990) Cyclic AMP and mechanisms of vasodilation. *Pharmacol Ther*. 47, 329-345.

Obata T., Liu T. T., Miller K. L., Luh W. M., Wong E. C., Frank L. R., and Buxton R. B. (2004) Discrepancies between BOLD and flow dynamics in primary and supplementary motor areas: application of the balloon model to the interpretation of BOLD transients. *Neuroimage*. 21, 144-153.

Panczel G., Daffertshofer M., Ries S., Spiegel D., and Hennerici M. (1999) Age and stimulus dependency of visually evoked cerebral blood flow responses. *Stroke*. 30, 619-623.

Pantano P., Baron J. C., Lebrun-Grandie P., Duquesnoy N., Bousser M. G., and Comar D. (1984) Regional cerebral blood flow and oxygen consumption in human aging. *Stroke*. 15, 635-641.

Richter W. and Richter M. (2003) The shape of the fMRI BOLD response in children and adults changes systematically with age. *Neuroimage*. 20, 1122-1131.

Riddle D. R., Sonntag W. E., and Lichtenwalner R. J. (2003) Microvascular plasticity in aging. *Ageing Res Rev*. 2, 149-168.

Rosengarten B., Spiller A., Aldinger C., and Kaps M. (2003) Control system analysis of visually evoked blood flow regulation in humans under normocapnia and hypercapnia. *Eur J Ultrasound*. 16, 169-175.

Rostrup E., Law I., Pott F., Ide K., and Knudsen G. M. (2002) Cerebral hemodynamics measured with simultaneous PET and near-infrared spectroscopy in humans. *Brain Res*. 954, 183-193.

Schroeter M. L., Zysset S., Kruggel F., and von Cramon D. Y. (2003) Age dependency of the hemodynamic response as measured by functional near-infrared spectroscopy. *Neuroimage*. 19, 555-564.

Silva A. C., Iadecola C., and Kim S.-G. (1999) The Dependence of BOLD and CBF Changes on the CBF Baseline during Somatsensory Simulation. In: *Seventh ISMRM Scientific Meeting*), pp. 1736, Philadelphia, PA.

Silvennoinen M. J., Clingman C. S., Golay X., Kauppinen R. A., and van Zijl P. C. (2003) Comparison of the dependence of blood R2 and R2* on oxygen saturation at 1.5 and 4.7 Tesla. *Magn Reson Med*. 49, 47-60.

Somlyo A. P. and Somlyo A. V. (1994) Signal transduction and regulation in smooth muscle. *Nature*. 372, 231-236.

Stewart G. N. (1894) Researches on the circulation time in organs and on the influences which affect it. *J Physiol (London)*. 15, Parts I-III.

Taoka T., Iwasaki S., Uchida H., Fukusumi A., Nakagawa H., Kichikawa K., Takayama K., Yoshioka T., Takewa M., and Ohishi H. (1998) Age correlation of the time lag in signal change on EPI-fMRI. *J Comput Assist Tomogr*. 22, 514-517.

Ursino M. (1991) Mechanisms of cerebral blood flow regulation. *Critical Reviews in Biomedical Engineering*. 18, 255-288.

West G. A., Meno J. R., Nguyen T. S., Ngai A. C., Simard J. M., and Winn H. R. (2003) cGMP-dependent and not cAMP-dependent kinase is required for adenosine-induced dilation of intracerebral arterioles. *J Cardiovasc Pharmacol*. 41, 444-451.

Wilson H. R. (1999) *Spikes, Decisions and Actions: Dynamical Foundations of Neuroscience*. Oxford University Press, Oxford.

Yacoub E., Shmuel A., Pfeuffer J., Van De Moortele P. F., Adriany G., Andersen P., Vaughan J. T., Merkle H., Ugurbil K., and Hu X. (2001) Imaging brain function in humans at 7 Tesla. *Magn Reson Med*. 45, 588-594.

Yang J., Clark J. W., Jr., Bryan R. M., and Robertson C. (2003) The myogenic response in isolated rat cerebrovascular arteries: smooth muscle cell model. *Med Eng Phys*. 25, 691-709.

Yang J., Clark J. W., Jr., Bryan R. M., and Robertson C. S. (2003) The myogenic response in isolated rat cerebrovascular arteries: vessel model. *Med Eng Phys*. 25, 711-717.

Zheng Y., Martindale J., Johnston D., Jones M., Berwick J., and Mayhew J. (2002) A model of the hemodynamic response and oxygen delivery to brain. *Neuroimage*. 16, 617-637.

Chapter 3

Caffeine Reduces the Initial Dip in the Visual BOLD Response at 3T

3.1 Abstract

Localized changes in oxygen consumption related to increased neural activity can result in a small and transient "initial dip" of the blood oxygenation level-dependent (BOLD) signal used in functional magnetic resonance imaging (fMRI). The initial dip has been of great interest to the fMRI community because it may provide a more accurate and localized measure of neural activity than the conventional BOLD signal increase. Although potentially useful as a technique for human brain mapping, the initial dip is not always detected and has been a source of some controversy. In this study, the BOLD response to a 4-s long visual stimulus was measured with a 3 Tesla MRI system in 5 healthy volunteers both before and immediately after a 200-mg oral caffeine dose. The caffeine dose significantly ($P < 0.001$) reduced or eliminated the initial dip in all subjects. These findings suggest that caffeine usage may be a key factor in the detection of the initial dip in human fMRI studies.

3.2 Introduction

The blood oxygenation level dependent signal (BOLD) used in most functional magnetic resonance imaging (fMRI) studies reflects local changes in deoxyhemoglobin (dHb). With increased neural activity, there are increases in both the rate of oxygen metabolism ($CMRO_2$) and the delivery of oxygen via cerebral blood flow (CBF). In most cases, the increase in oxygen delivery eventually exceeds the rate of oxygen consumption, leading to a prolonged decrease in dHb and an increase in the BOLD response (Buxton et al., 1998). This signal increase, referred to as the positive BOLD response, is the basis for most fMRI applications. However, a number of optical imaging and functional magnetic resonance imaging (fMRI) studies have shown that, in the first few seconds following the onset of increased neural activity, $CMRO_2$ may increase more quickly than CBF, leading to an initial transient increase in dHb and an associated "initial dip" in the BOLD signal (Ernst et al., 1994; Hu et al., 1997; Malonek et al., 1996; Menon et al., 1995; Thompson et al., 2004). In addition, it has been shown that the initial dip is better localized to areas of neural activity (e.g. cortical columns), as compared to the more diffuse positive BOLD response (Duong et al. 2000; Yacoub et al. 2001; Kim et al. 2000; Yacoub and Hu 2001). These observations are consistent with a view in which the early portion of the BOLD signal reflects changes in dHb that are primarily localized to the microvasculature, whereas the later part of the BOLD signal reflects dHb changes in both the microvasculature and the macrovasculature, due to the draining of dHb into larger vessels (Duong et al. 2000; Fukuda et al. 2005; Yacoub et al. 2001).

Although the initial dip has been observed in a number of human and animal studies (Duong et al., 2000; Ernst et al., 1994; Hu et al., 1997; Kim et al., 2000; Malonek et al., 1996; Vanzetta et al., 1999; Yacoub et al., 2001; Yacoub et al., 2001), some animal studies have found no evidence for an initial dip (Lindauer et al., 2001; Mandeville et al., 1999; Marota et al., 1999;

Silva et al., 2000). It has been suggested that differences in imaging methodology, brain regions, animal species, and anesthesia are responsible for the conflicting observations in animal studies (Ances, 2004; Buxton, 2001). One human fMRI study suggested that the initial dip may be an experimental artifact that arises when stimuli are too closely spaced in time (Fransson et al., 1998), but a subsequent study found an initial dip even with wider spacings (Yacoub et al., 1999). While there do not appear to be additional human fMRI studies that explicitly focus on the absence of the initial dip, there are many studies of the dynamics of the BOLD response that either do not find or simply do not mention the initial dip. For example, the initial dip was not observed in studies examining the effects of carbon dioxide on the BOLD response (Cohen et al., 2002; Kemna et al., 2001). Cohen et al attributed the lack of detection to differences in experimental methodology, which can be an important factor given the relatively small amplitude of the initial dip.

In addition to methodological differences, variations in the baseline vascular state due to factors such as pharmacological agents, disease, and age have been shown to alter the dynamics of the BOLD response and may therefore affect the detection of the initial dip in humans (D'Esposito et al., 2003). As an example, the carbon dioxide studies mentioned above found that vasodilation caused by hypercapnia significantly slowed down the dynamics of the BOLD response, while vasoconstriction caused by hypocapnia led to a quickening of the response. In a recent study using a 4 Tesla MRI system, we showed that caffeine, a known vasoconstrictor, led to a quickening of the visual BOLD response in a manner similar to that observed with hypocapnia (Liu et al., 2004). Due to technical considerations (e.g. scanner instabilities), the initial dip was not easily detected in that study. In the present study, performed on a 3 Tesla MRI system, we demonstrate robust detection of the initial dip and show that a 200 mg caffeine dose can significantly reduce the initial dip.

3.3 Methods

3.3.1 Experimental Protocol

Five healthy subjects (ages 23 to 39) participated in the study after giving informed consent. Each subject refrained from ingesting any food or drink containing caffeine for at least 12 hours prior to the experiment. The estimated daily caffeine usage of the subjects based on self-reports of coffee, tea, and caffeinated soda consumption is summarized in Table 1. The assumed caffeine contents for an 8-oz coffee, tea, and soda were 100 mg, 40 mg, and 20 mg, respectively (Fredholm et al., 1999). Each experiment lasted approximately 3 hours and consisted of a 1-hour pre-dose imaging session followed by a 1-hour post-dose session. In addition to the actual time spent on imaging, the length of each session included time for preparation (e.g. ensuring that physiological monitoring equipment was working properly), parameter set-up and execution of prescan routines (as necessary), and instruction of the subject prior to each scan. Between sessions the subject ingested an over-the-counter tablet containing 200-mg of caffeine and rested outside the scanner for approximately 30 minutes. The first functional run began approximately 45 minutes post ingestion. This interval was chosen based on studies showing that the absorption of caffeine from the gastrointestinal tract reaches 99% about 45 minutes after ingestion, with a half-life of 2.5 to 4.5 hours (Fredholm et al., 1999).

During both the pre-dose and post-dose imaging sessions, each subject viewed two repeats of a periodic single trial visual stimulus consisting of a 20-second initial “off” period followed by 5 cycles of a 4 second “on” period and a 40 second “off” period. During the “on” periods, a full-field, full contrast radial 8 Hz flickering checkerboard was displayed, while the “off” periods consisted of a gray background of luminance equal to the average luminance of the “on” period. Three of the five subjects viewed two additional repeats of the periodic single trial design. As described below, these were acquired with a smaller imaging slice thickness than the first two repeats. In addition, a resting-state scan, during which the subject was presented with the “off” condition for 3 minutes, was performed and used to characterize the resting CBF level.

3.3.2 Imaging Protocol

Imaging data were collected on a GE Signa Excite 3 Tesla whole body system with a body transmit coil and an eight channel receive coil. Laser alignment was used to landmark the subject and minimize differences in head position between sessions. During the resting-state scan, data were acquired with a PICORE QUIPPS II (Wong et al., 1998) arterial spin labeling (ASL) sequence (TR= 2s , TI1/TI2= 600/1500ms, 10 cm tag thickness, and a 1 cm tag-slice gap) with a dual echo spiral readout (TE1/TE2=9.1/30 ms, FOV=24 cm, 64x64 matrix, and a flip angle= 90 degrees). Small bipolar crusher gradients were included to remove signal from large vessels ($b=2\ s/mm^2$). Three oblique axial 8 mm slices were prescribed about the calcarine sulcus for this ASL run. During the periodic single trial runs, BOLD-weighted images were acquired with a spiral readout (TE=25ms, TR=500 ms, FOV=24cm, 64x64 matrix, and a flip-angle of 45 degrees). In all five subjects, these BOLD runs used the same slice prescription as the ASL runs (e.g. three 8 mm slices). The choice of the 8mm slice thickness reflects the fact that the experiments on two of the subjects (labeled as Subjects 4 and 5 in Results) were not originally intended to examine the initial dip. To determine whether there was an effect of the large slice thickness, the experiments in the three remaining subjects (labeled 1 to 3 in Results) included two additional BOLD-weighted runs using the periodic single trial design and acquired with six oblique 4 mm slices covering the same volume as the three 8 mm slices. For all periodic single trials acquired at either slice thickness, 480 volumes at a TR of 500 ms were acquired.

A high resolution structural scan was acquired with a magnetization prepared 3D fast spoiled gradient acquisition in the steady state (FSPGR) sequence (TI 450ms, TR 7.9ms, TE 3.1ms, 12 degree flip angle, FOV 25x25x16 cm, matrix 256x256x124). In addition, a cerebrospinal fluid (CSF) reference scan and a minimum contrast scan were acquired for use in CBF quantification. The CSF scan consisted of a single-echo, single repetition scan acquired at full relaxation and echo time equal to 9.1 ms, while the minimal contrast scan was acquired at TR=2 sec and TE=11 ms. Both scans used the same in-plane parameters as the ASL scans, but the number of slices was increased to cover the lateral ventricles.

Cardiac pulse and respiratory effort data were monitored using a pulse oximeter (InVivo) and a respiratory effort transducer (BIOPAC), respectively. The pulse oximeter was placed on the subject's right index finger, and the respiratory effort belt was placed around the subject's abdomen. Physiological data were sampled at 40 samples per second using a multi-channel data acquisition board (National Instruments).

3.3.3 Data Analysis

All images were coregistered using AFNI software (Cox, 1996). The structural scan from each post-dose session was aligned to the structural scan of its respective pre-dose session, and the rotation and shift matrix used for this alignment was then applied to the post-dose BOLD and ASL images. An image-based retrospective correction method RETROICOR (Glover et al., 2000; Restom et al., 2004) was used to reduce physiological noise due to cardiac and respiratory fluctuations. For each subject, a mean ASL image was formed from the average difference of the control and tag images from the resting-state scan data. This mean ASL image was then corrected for coil inhomogeneities using the minimum contrast image (Wang et al., 2005) and converted to physiological units using the CSF image as a reference signal (Chalela et al., 2000).

For each slice thickness, average BOLD time series were formed from the data (after physiological noise correction) for the two runs acquired at that thickness. All subsequent analyses were performed separately for the average BOLD time series. Correlation analysis was performed using a positive BOLD reference function formed by convolving the periodic single trial stimulus pattern with a gamma density function of the form $h(t) = (\tau n!)^{-1}\left(\left(t-\Delta t\right)/\tau\right)^{n} \exp\left(-\left(t-\Delta t\right)/\tau\right)$ for $t \geq \Delta t$ and 0 otherwise, with $\tau = 1.2$, $n = 3$ and $\Delta t = 1$. A constant term and linear trend term were used as nuisance terms in the correlation analysis.

Functional regions of interest (ROI) were defined for the pre-dose ($\mathrm{ROI}_{\mathrm{pre}}$) and post-dose ($\mathrm{ROI}_{\mathrm{post}}$) data using a correlation coefficient threshold of 0.40 based on the positive BOLD response. A joint functional ROI ($\mathrm{ROI}_{\mathrm{joint}}$) was then formed from the intersection of $\mathrm{ROI}_{\mathrm{pre}}$ and $\mathrm{ROI}_{\mathrm{post}}$, using a spatial clustering criterion (one nearest neighbor) to eliminate isolated voxels. The area of the first 2.5 seconds of the average BOLD response, referred to as the initial dip area, was computed for each voxel within $\mathrm{ROI}_{\mathrm{joint}}$, with a negative area corresponding to the presence of an initial dip. Voxels within $\mathrm{ROI}_{\mathrm{joint}}$ displaying an initial dip in the pre-dose data were then used to define an initial dip ROI, denoted as $\mathrm{ROI}_{\mathrm{dip.}}$ In other words, $\mathrm{ROI}_{\mathrm{dip}}$ encompasses all voxels in $\mathrm{ROI}_{\mathrm{joint}}$ that display an initial dip in the pre-dose periodic BOLD response.

Note that for subjects with both 4 mm and 8 mm slice thickness data, a separate $\mathrm{ROI}_{\mathrm{dip}}$ was defined for each slice thickness. For each voxel within $\mathrm{ROI}_{\mathrm{dip}}$ the average BOLD response was formed by averaging across cycles of the average BOLD time series. For each subject, a mean BOLD response was then computed for $\mathrm{ROI}_{\mathrm{dip}}$ and a paired t-test (two-tailed) was used to compare the pre-dose and post-dose initial dip areas across all voxels within $\mathrm{ROI}_{\mathrm{dip}}$. In addition, the average CBF was computed for $\mathrm{ROI}_{\mathrm{dip}}$, and a paired t-test (two-tailed) was used to compare the pre-dose and post-dose CBF levels across voxels in $\mathrm{ROI}_{\mathrm{dip}}$.

An additional correlation analysis was performed to show localization of the initial dip, but was not used for further statistical comparisons. The initial dip reference function was a symmetric triangle that started at 0.5 seconds, peaked at 1.5 seconds with a negative amplitude of -0.5, and returned to zero at 2.5 seconds (total duration = 2 seconds). A spatial clustering criterion (one nearest neighbor) was used to eliminate isolated voxels.

3.4 Results

The group average pre-dose (blue) and post-dose (red) BOLD responses (N = 5) from the 8mm slice thickness data are shown in the top row of Figure 1, with panel (b) depicting a magnified view of the initial response. Consistent with prior findings (Liu et al., 2004), the administration of caffeine speeds up the BOLD response with a decrease in peak-time from 8.45 s to 7.45 s and full-width half maximum from 6.95 s to 6.1 s. The peak amplitude increased from 1.83% to 2.16% following caffeine ingestion. In the initial portion of the pre-dose response, the response dips after the onset of the visual stimulus, reaching a minimum value of –0.16% at 1.5 seconds, at which time the response begins to recover and becomes positive at 2.5 seconds. In contrast to the pre-dose initial response, the post-dose response increases after the onset of stimulus. Group average responses from the 4mm slice thickness data (N = 3 subjects) are shown in the bottom row of Figure 1. The results are similar to those observed for the 8 mm slice thickness data, with the initial dip clearly visible in the pre-dose response and reduced in the post-dose response. Following the initial onset of visual stimulation, the pre-dose response dips to a minimum value of –0.24% at 1.5 s before becoming positive at 2.5 s.

Figure 2 shows the post-dose (y-axis) versus pre-dose (x-axis) initial dip areas from the ROI_{dip} for each subject. Panels a-c and d-h correspond to the data acquired at 4mm and 8mm slice thicknesses, respectively. A significant ($p < 8.4e-4$) reduction of the initial dip (e.g. more positive initial dip area) was observed for each subject. Figure 3 shows magnified views of the pre-dose (blue) and post-dose (red) average initial responses for each subject. Panels a-c show the responses from the 4mm slice thickness data while panels d-h are for the 8mm slice thickness data. The reduction of the initial dip by caffeine is clearly present in each subject's responses.

Figure 4 compares the pre-dose and post-dose spatial localization of the initial dip and the positive BOLD response for a representative slice (4mm thick) from subject 1. Panels a) and c) show the spatial extent of the initial dip in the pre-dose and post-dose conditions, respectively, with the colorbar indicating the scale of the correlation coefficient calculated with the initial dip reference function. Consistent with the above observations of a significant reduction of the initial dip with caffeine, the spatial extent of the initial dip is greatly diminished in the post-dose map. Panels b) and d) are positive BOLD activation maps for the pre-dose and post-dose conditions, respectively, with the colorbar indicating the scale of the correlation coefficients obtained with the positive BOLD reference function. In comparison to the initial dip spatial maps the positive BOLD maps exhibit a wider spread of activation across the occipital cortex, consistent with the findings of prior studies (Yacoub and Hu 2001 and Yacoub et al. 2001). Spatial localization maps from the other subjects showed similar behavior.

Table 1 shows the average pre-dose and post-dose CBF values for each subject, along with p-values obtained with two-tailed paired t-tests. The mean and standard deviations of the CBF were computed using voxels within each subject's ROI_{dip}. For each subject, there is a significant reduction ($p < 1.7e-11$) in CBF associated with the caffeine dose, with the percent decrease in CBF ranging from 30 to 51% across subjects.

3.5 Discussion

A significant reduction in the initial dip amplitude due to caffeine was observed in each subject that was studied. This reduction was observed in both 8 mm slice thickness data (N=5) and the 4mm slice thickness data (N=3), indicating that the effect is fairly robust with respect to voxel size. Consistent with prior studies, the caffeine dose also significantly reduced the baseline CBF level in each subject (Cameron et al., 1990; Field et al., 2003; Liu et al., 2004).

Why does caffeine reduce the initial dip? Caffeine exerts both neural and vascular effects through its binding to adenosine receptors in the brain (Fredholm et al., 1999). In particular, its neurostimulant effects are thought to arise from the inhibition of adenosine A1 receptors, while its vasoconstrictive effects are believed to be due primarily to the inhibition of adenosine A_{2A} receptors (Ngai et al., 2001). It is reasonable to conjecture that the enhancement of neural activity with caffeine would primarily affect the $CMRO_2$ response, while vasoconstriction due to caffeine is more likely to alter the CBF response. The presence of an initial dip is generally thought to reflect a temporal mismatch between $CMRO_2$ and CBF, with $CMRO_2$ increasingly more rapidly than CBF following the onset of stimulus (Ances, 2004; Buxton, 2001). A reduction in the initial dip could therefore reflect either a relative quickening of the CBF response or a relative slowing down of the $CMRO_2$ response. Given its neurostimulant properties, it seems unlikely that caffeine would cause the $CMRO_2$ response to become slower. In contrast, a quickening of the CBF response due to vasoconstriction would be consistent with the findings of a recent theoretical model introduced by our group (Behzadi et al., 2005).

In the theoretical model, the dynamics of the CBF response depend on the biomechanical responsiveness of the arterioles, which in turn depends on the relative contributions of the vascular smooth muscle and connective tissue to the dynamics of the arteriolar wall. With vasodilatory agents, such as carbon dioxide, the vascular smooth muscle relaxes and exerts less force so that the arteriole may expand, while the connective tissue becomes stiffer and exerts more force, similar to the walls of a rubber tube becoming less compliant as it expands. This makes the arteriole relatively less responsive and slows down the dynamic CBF response. In contrast, with the application of a vasoconstrictive agent, such as caffeine, the vascular smooth muscle exerts more force in order to constrict the arteriole, while the force exerted by the connective tissue is reduced. This redistribution of forces makes the arteriole more responsive and speeds up the dynamic CBF response.

While the above arguments suggest that the reduction in the initial dip is due primarily to a quickening of the CBF response, an effect of caffeine on the CMRO$_2$ response cannot be ruled out. It is likely, however, that caffeine-induced changes in the CMRO$_2$ response are smaller than changes in the CBF response. Further experimental studies directly examining the effect of caffeine on the CBF and CMRO$_2$ responses would be useful for clarifying the mechanisms through which caffeine affects the initial dip.

Our finding that caffeine reduces the initial dip in humans may also provide insight into the conflicting reports concerning the initial dip in animals. A number of the studies (Duong et al., 2000; Kim et al., 2000; Logothetis et al., 1999) reporting an initial dip have used isoflurane, which has been shown to increase baseline CBF (Sicard et al., 2003). The isoflurane-induced vasodilation would tend to slow down the CBF response and enhance the initial dip. Recently, (Fukuda et al., 2005) showed that the administration of sodium nitroprusside, a vasodilator, significantly attenuated the CBF response to neural stimulus and led to a large and sustained initial dip in cat visual cortex. In contrast, studies using alpha-chloralose, which has been shown to reduce baseline CBF (Nakao et al., 2001), have typically reported an absence of an initial dip, similar to the findings obtained here with caffeine (Mandeville et al., 1999; Marota et al., 1999; Silva et al., 2000). However, as pointed out in (Ances, 2004), there are counter-examples to these broad trends, such as no initial dip with isoflurane (Lindauer et al., 2001) and an initial dip with alpha-chloralose (Ances et al., 2001). In addition, the initial dip has been observed with urethane, which has been shown to slightly reduce CBF in the hippocampus (Jones et al., 2001; Osborne, 1997). Thus, while the vasoactive properties of anesthesia may account for some of the variability in the animal studies, it is likely that additional factors, such as brain region, animal species, and details of the experimental preparation and imaging method, also play a significant role.

Finally, given the widespread use of dietary caffeine in the general population, it is likely that variability in caffeine usage across subjects plays a significant role in the detection of the initial dip in human fMRI studies, especially in young healthy populations where additional confounding factors such as medication and disease are typically minimal. Caffeine usage should therefore be carefully controlled in human fMRI studies focused on the initial dip.

Acknowledgments

The authors thank Joy Liau for her assistance with the preparation of this paper. This work was supported in part by a grant from the Whitaker Foundation.

Publication Acknowledgments

Chapter 3, in full, is a reprint of the material as it appears in:

Behzadi, Y., and Liu, T.T., (2006) Caffeine reduces the initial dip in the visual BOLD response at 3T. *Neuroimage*, 32(1), 9-15.

The dissertation author was the primary author of these papers. I would like to acknowledge my co-author Professor Thomas T. Liu.

3.6 Figures

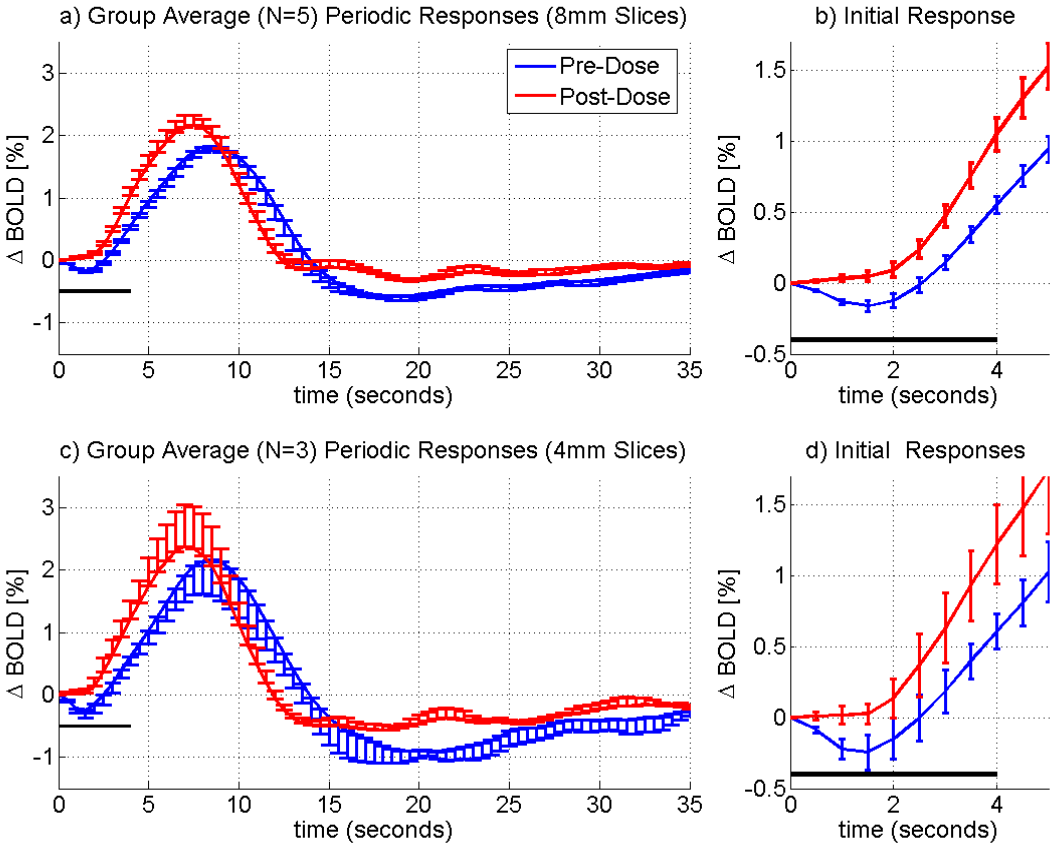

Figure 3.1. Pre-dose (blue) and post-dose (red) group averaged periodic BOLD responses acquired with slice thicknesses of 8mm (panel a) and 4mm (panel c). Averages are from voxels within $\mathrm{ROI}_{\mathrm{dip}}$ (defined separately for each slice thickness). Magnified views are shown in panels (b) and (d). The initial dip is clearly evident in the pre-dose responses and is absent in the corresponding post-dose responses. The length of each error bar represents the standard error across subjects and the thick black line denotes the stimulus duration.

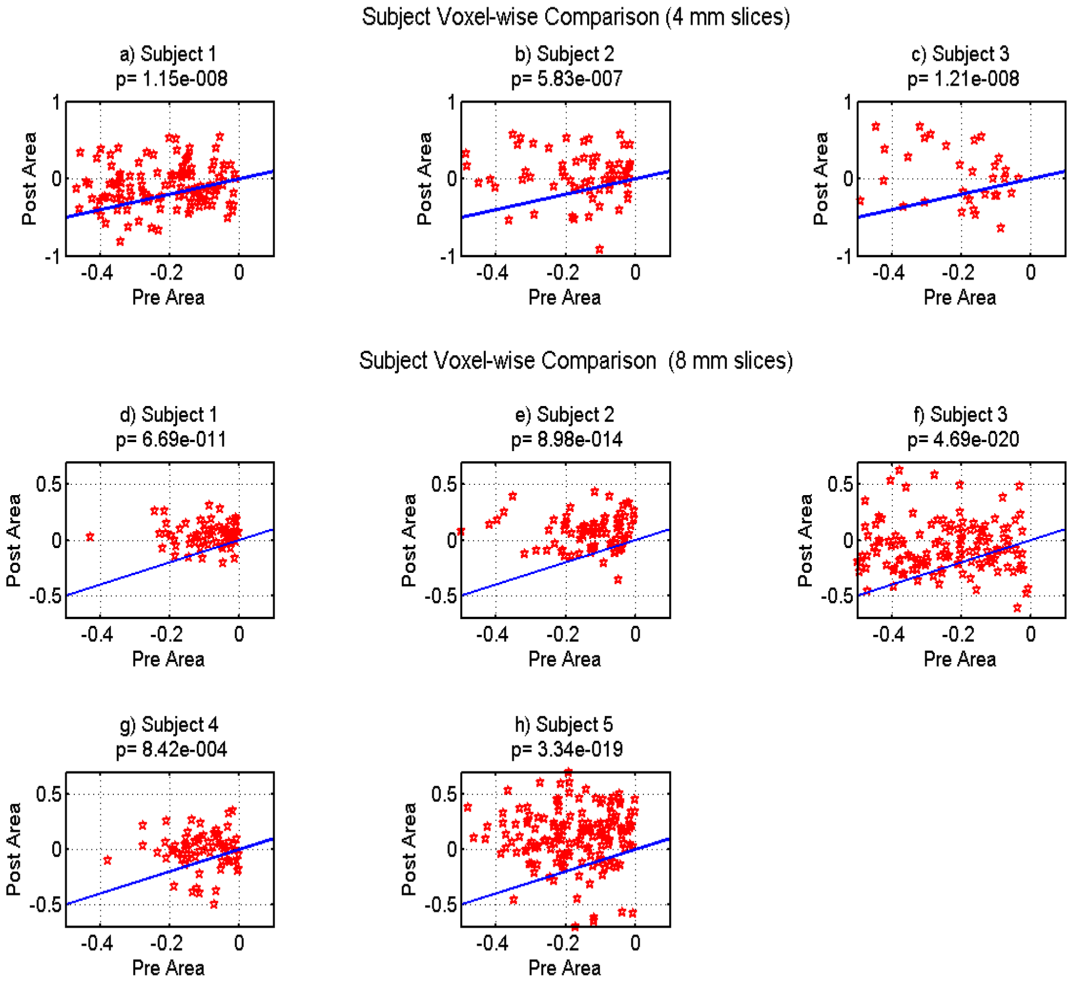

Figure 3.2. Comparison of the post-dose (y-axis) and pre-dose (x-axis) initial dip areas for each subject for voxels within $\mathrm{ROI}_{\mathrm{dip}}$. The solid line represents the line of equality. Panels a-c and d-h represent subject data acquired with slice thicknesses of 4 mm and 8 mm, respectively. The p-values were computed with a paired t-test (two-tailed).

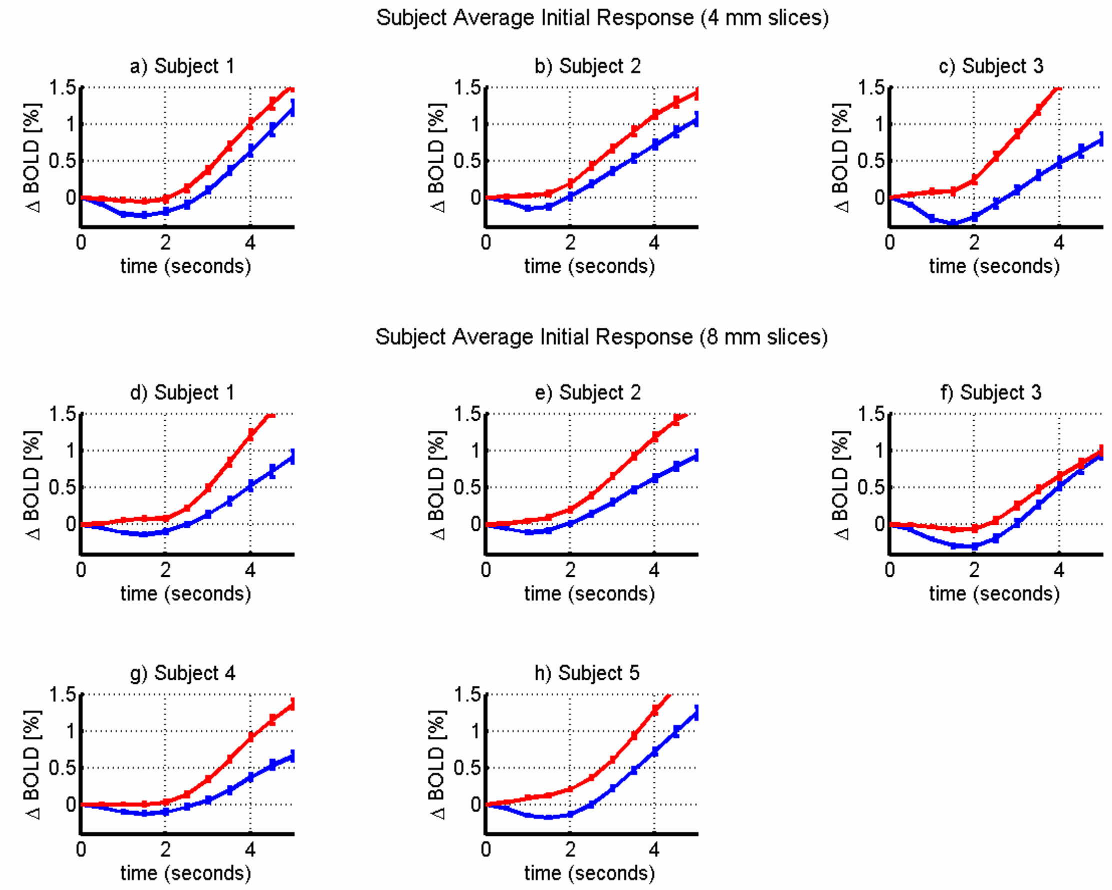

Figure 3.3. Magnified views of the pre-dose (blue) and post-dose (red) initial responses for each subject averaged across their respective ROI_{dip}. Panels a-c show the responses from the 4mm slice thickness data while panels d-h are for the 8mm slice thickness data. The error bars represent the standard error across voxels. The reduction of the initial dip by caffeine is clearly present in each subject's responses.

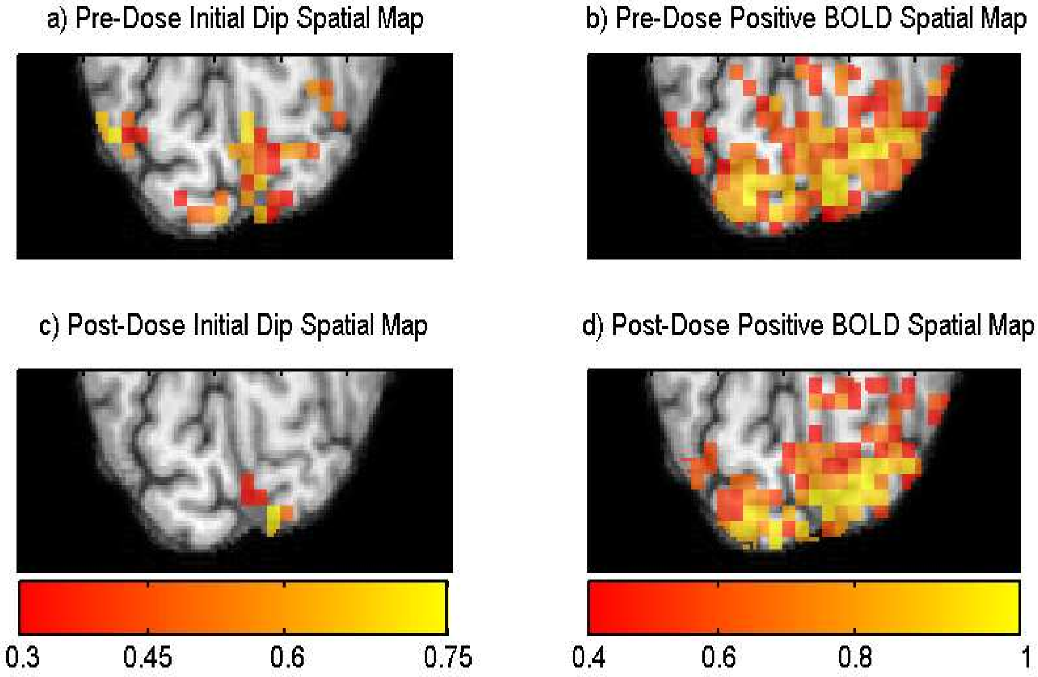

Figure 3.4. Comparison of the pre-dose (top row) and post-dose (bottom row) spatial localization maps for the initial dip (left column) and the positive BOLD response (right column) for subject 1. Panels a) and c) show the spatial extent of the initial dip in the pre-dose and post-dose conditions, respectively, with the colorbar below panel c indicating the scale of the correlation coefficients obtained with the initial dip reference function. Panels b) and d) are positive BOLD spatial maps for the pre-dose and post-dose conditions, respectively. The colorbar below panel d) indicates the scale of the correlation coefficients obtained with the positive BOLD reference function.

Table 3.1. Pre-dose and post-dose baseline CBF values shown as mean (standard deviation). Mean and standard deviation were computed across voxels in each subject's respective $ROI_{dip.}$ For each subject, significance was computed with a paired t test (two-sided).

Subject	Estimated daily caffeine usage (mg)	Pre-dose baseline CBF ml/(100 g min)	Post-dose baseline CBF ml/(100 g min)	Paired t-test P Value
1	200	53.4 (28.1)	33.5 (16.1)	3.9 e-18
2	<50	57.6 (23.3)	35.1 (16.8)	2.4 e-20
3	200	55.4 (22.6)	38.9 (20.2)	1.7e-11
4	<50	73.1 (14.0)	35.8 (15.9)	1.0e-19
5	250	88.2 (25.2)	47.4 (21.8)	1.8e-19

3.7 References

Ances B. M. (2004) Coupling of changes in cerebral blood flow with neural activity: what must initially dip must come back up. *J Cereb Blood Flow Metab*. 24, 1-6.

Ances B. M., Buerk D. G., Greenberg J. H., and Detre J. A. (2001) Temporal dynamics of the partial pressure of brain tissue oxygen during functional forepaw stimulation in rats. *Neurosci Lett*. 306, 106-110.

Behzadi Y. and Liu T. T. (2005) An arteriolar compliance model of the cerebral blood flow response to neural stimulus. *Neuroimage*. 25, 1100-1111.

Buxton R. B. (2001) The elusive initial dip. *Neuroimage*. 13, 953-958.

Buxton R. B., Wong E. C., and Frank L. R. (1998) Dynamics of blood flow and oxygenation changes during brain activation: the balloon model. *Magn Reson Med*. 39, 855-864.

Cameron O. G., Modell J. G., and Hariharan M. (1990) Caffeine and human cerebral blood flow: a positron emission tomography study. *Life Sci*. 47, 1141-1146.

Chalela J., Alsop D. C., Gonzalez-Atavales J. B., Maldjian J. A., Kasner S. E., and Detre J. A. (2000) Magnetic resonance perfusion imaging in acute ischemic stroke using continuous arterial spin labeling. *Stroke*. 31, 680-687.

Cohen E. R., Ugurbil K., and Kim S. G. (2002) Effect of basal conditions on the magnitude and dynamics of the blood oxygenation level-dependent fMRI response. *J Cereb Blood Flow Metab*. 22, 1042-1053.

Cox R. W. (1996) AFNI-software for analysis and visualization of functional magnetic resonance neuroimages. *Comput Biomed Res*. 29, 162-173.

D'Esposito M., Deouell L. Y., and Gazzaley A. (2003) Alterations in the BOLD fMRI signal with ageing and disease: a challenge for neuroimaging. *Nat Rev Neurosci*. 4, 863-872.

Duong T. Q., Kim D. S., Ugurbil K., and Kim S. G. (2000) Spatiotemporal dynamics of the BOLD fMRI signals: toward mapping submillimeter cortical columns using the early negative response. *Magn Reson Med*. 44, 231-242.

Ernst T. and Hennig J. (1994) Observation of a fast response in functional MR. *Magn Reson Med*, 146-149.

Field A. S., Laurienti P. M., Yen Y.-F., Burdette J. H., and Moody D. M. (2003) Dietary Caffeine Consumption and Withdrawal: Confounding Variables in Quantitative Cerebral Perfusion Studies? *Radiology*. 227, 129-135.

Fransson P., Kruger G., Merboldt K. D., and Frahm J. (1998) Temporal characteristics of oxygenation-sensitive MRI responses to visual activation in humans. *Magn Reson Med*. 39, 912-919.

Fredholm B. B., Battig K., Holmen J., Nehlig A., and Zvartau E. E. (1999) Actions of caffeine in the brain with special reference to factors that contribute to its widespread use. *Pharmacol Rev*. 51, 83-133.

Fukuda M., Wang P., Moon C., Tanifuji M., and Kim S. G. (2005) Spatial specificity of the enhanced dip inherently induced by prolonged oxygen consumption in cat visual cortex: Implication for columnar resolution functional MRI. *Neuroimage*. in-press.

Glover G. H., Li T. Q., and Ress D. (2000) Image-based method for retrospective correction of physiological motion effects in fMRI: RETROICOR. *Magn Reson Med*. 44, 162-167.

Hu X., Le T. H., and Ugurbil K. (1997) Evaluation of the early response in fMRI in individual subjects using short stimulus duration. *Magn Reson Med*. 37, 877-884.

Jones M., Berwick J., Johnston D., and Mayhew J. (2001) Concurrent optical imaging spectroscopy and laser-Doppler flowmetry: the relationship between blood flow, oxygenation, and volume in rodent barrel cortex. *Neuroimage*. 13, 1002-1015.

Kemna L. J. and Posse S. (2001) Effect of respiratory CO(2) changes on the temporal dynamics of the hemodynamic response in functional MR imaging. *Neuroimage*. 14, 642-649.

Kim D. S., Duong T. Q., and Kim S. G. (2000) High-resolution mapping of iso-orientation columns by fMRI. *Nat Neurosci*. 3, 164-169.

Lindauer U., Royl G., Leithner C., Kuhl M., Gold L., Gethmann J., Kohl-Bareis M., Villringer A., and Dirnagl U. (2001) No evidence for early decrease in blood oxygenation in rat whisker cortex in response to functional activation. *Neuroimage*. 13, 988-1001.

Liu T. T., Behzadi Y., Restom K., Uludag K., Lu K., Buracas G. T., Dubowitz D. J., and Buxton R. B. (2004) Caffeine alters the temporal dynamics of the visual BOLD response. *Neuroimage*. 23, 1402-1413.

Logothetis N. K., Guggenberger H., Peled S., and Pauls J. (1999) Functional imaging of the monkey brain. *Nat Neurosci*. 2, 555-562.

Malonek D. and Grinvald A. (1996) Interactions between electrical activity and cortical microcirculation revealed by imaging spectroscopy: implications for functional brain mapping. *Science*. 272, 551-554.

Mandeville J. B., Marota J. J., Ayata C., Moskowitz M. A., Weisskoff R. M., and Rosen B. R. (1999) MRI measurement of the temporal evolution of relative CMRO(2) during rat forepaw stimulation. *Magn Reson Med*. 42, 944-951.

Marota J. J., Ayata C., Moskowitz M. A., Weisskoff R. M., Rosen B. R., and Mandeville J. B. (1999) Investigation of the early response to rat forepaw stimulation. *Magn Reson Med*. 41, 247-252.

Menon R. S., Ogawa S., Strupp J. P., Anderson P., and Ugurbil K. (1995) BOLD based functional MRI at 4 tesla includes a capillary bed contribution: echo-planar imaging correlates with previous optical imaging using intrinsic signals. *Magn Reson Med*. 33, 453 - 459.

Nakao Y., Itoh Y., Kuang T. Y., Cook M., Jehle J., and Sokoloff L. (2001) Effects of anesthesia on functional activation of cerebral blood flow and metabolism. *Proc Natl Acad Sci U S A*. 98, 7593-7598.

Ngai A. C., Coyne E. F., Meno J. R., West G. A., and Winn H. R. (2001) Receptor subtypes mediating adenosine-induced dilation of cerebral arterioles. *Am J Physiol Heart Circ Physiol*. 280, H2329-2335.

Osborne P. G. (1997) Hippocampal and striatal blood flow during behavior in rats: chronic laser Doppler flowmetry study. *Physiol Behav*. 61, 485-492.

Restom K., Behzadi Y., Uludag K., and Liu T. T. (2004) Image Based Physiological Noise Correction for Perfusion-Based fMRI. In: *12th ISMRM Scientific Meeting*), pp. 2525, Kyoto.

Sicard K., Shen Q., Brevard M. E., Sullivan R., Ferris C. F., King J. A., and Duong T. Q. (2003) Regional cerebral blood flow and BOLD responses in conscious and anesthetized rats under basal and hypercapnic conditions: implications for functional MRI studies. *J Cereb Blood Flow Metab*. 23, 472-481.

Silva A. C., Lee S. P., Iadecola C., and Kim S. G. (2000) Early temporal characteristics of cerebral blood flow and deoxyhemoglobin changes during somatosensory stimulation. *J Cereb Blood Flow Metab*. 20, 201-206.

Thompson J. K., Peterson M. R., and Freeman R. D. (2004) High-resolution neurometabolic coupling revealed by focal activation of visual neurons. *Nat Neurosci*. 7, 919-920.

Vanzetta I. and Grinvald A. (1999) Increased cortical oxidative metabolism due to sensory stimulation: implications for functional brain imaging. *Science*. 286, 1555-1558.

Wang J., M.Qiu, and Constable R. T. (2005) In vivo method for corrrecting transmit/receive nonuniformities with phased array coils. *Magn Reson Imaging*. 53, 666-674.

Wong E. C., Buxton R. B., and Frank L. R. (1998) Quantitative imaging of perfusion using a single subtraction (QUIPSS and QUIPSS II). *Magn Reson Med*. 39, 702-708.

Yacoub E. and Hu X. (2001) Detection of the early decrease in fMRI signal in the motor area. *Magn Reson Med*. 45, 184-190.

Yacoub E., Le T. H., Ugurbil K., and Hu X. (1999) Further evaluation of the initial negative response in functional magnetic resonance imaging. *Magn Reson Med*. 41, 436-441.

Yacoub E., Shmuel A., Pfeuffer J., Van De Moortele P. F., Adriany G., Ugurbil K., and Hu X. (2001) Investigation of the initial dip in fMRI at 7 Tesla. *NMR Biomed*. 14, 408-412.

Chapter 4

CompCor: Component Based Noise Correction for BOLD and Perfusion fMRI

4.1 Abstract

A component based method (CompCor) for the reduction of noise in both blood oxygenation level dependent (BOLD) and perfusion-based functional magnetic resonance imaging (fMRI) data is presented. We show the inclusion of principal components derived from noise-regions-of-interest (noise ROI) as regressors within the appropriate general linear models for the BOLD and perfusion-based fMRI time-series data can significantly reduce physiological noise (e.g. cardiac and respiratory induced fluctuations). In our presentation we investigate the use of two different methodologies for determining the noise ROI. The first method uses anatomical data to identify white matter and CSF-only voxels while the second method uses voxels with high temporal standard deviation to define regions dominated by physiological noise.

With application of CompCor, the temporal standard deviation of resting state BOLD and ASL is significantly ($p<0.01$) reduced compared to no correction in a manner consistent with application of a previously presented retrospective image based correction scheme, RETROICOR. Additionally, we show a marked improvement in sensitivity during visual stimulus as quantified in the number of significantly activated voxels based on an F-statistic threshold. As compared to RETROICOR, CompCor has the following advantages: 1) does not

require external monitoring of physiological activity (such as cardiac or respiratory signals); 2) can be executed in a fully automated fashion (e.g. does not require user intervention).

4.2 Introduction

Over the last decade, blood oxygenation level dependent (BOLD) and perfusion-based functional magnetic resonance imaging (fMRI) have become indispensable tools for studies of the working brain. When utilized together, the BOLD and perfusion signal can provide a quantitative understanding of the metabolic response to neural activity and provide insight into neurovascular coupling mechanisms (Hoge et al., 1999). However, as the fMRI community has moved to higher field strengths, physiological noise has become an increasingly important confound limiting the sensitivity and the application of fMRI studies (Kruger et al., 2001; Liu et al., 2006).

Physiological fluctuations have been shown to be a significant source of noise in BOLD fMRI experiments, with even a greater effect in perfusion-based fMRI utilizing arterial spin labeling (ASL) techniques (Kruger et al., 2001; Restom et al., 2006). Physiological sources of noise primarily include cardiac pulsations and modulations of the main magnetic field by thoracic cavity volume changes associated with respiration. Additional sources include blood flow changes coupled to end-tidal $C0_2$ and vasomotion occurring at 0.1 Hz (Dagli et al., 1999; Glover et al., 2000; Hu et al., 1995).

Approaches to removing cardiac and respiratory related-noise include temporal filtering, image based retrospective correction (RETROICOR), k-space based correction (RETROKCOR) and navigator echo based correction (DORK) (Biswal et al., 1996; Glover et al., 2000; Hu et al., 1995; Josephs et al., 2001; Pfeuffer et al., 2002). More recently, RETROICOR has been extended to a general linear model (GLM) framework (Lund et al., 2006) and modified for use in ASL (Restom et al., 2006). A recent adaptation for BOLD based imaging involved the addition of regressors describing variations in respiratory volume (Birn et al., 2006).

An alternate approach to the use of external measures of physiological activity or specially modified pulse sequences is to globally subtract average time-courses from regions unlikely to be associated with neural activity (e.g. ventricles, large vessels, etc.). (Lund et al., 2001; Petersen et al., 1998). Additionally, component based techniques, utilizing independent component analysis (ICA) or principal components analysis (PCA), have shown potential in identifying spatial and temporal patterns of structured noise (Beckmann et al., 2004; McKeown et al., 2003; Thomas et al., 2002). However, the utility of component based methods has been limited to BOLD studies with sampling times short enough to clearly differentiate cardiac and respiratory elements from evoked responses (Thomas et al., 2002) in which case a temporal band pass filter would be adequate for noise removal.

Here we present and characterize a novel component based method (CompCor) for the correction of physiological noise in BOLD and perfusion-based fMRI. We show that principal components derived from noise regions-of-interest (ROI) are able to accurately describe physiological noise processes in gray matter regions. In our presentation we investigate the use of two different methodologies for determining noise ROIs. The first method uses anatomical data to identify white matter and CSF voxels, while the second method uses the temporal standard deviation (tSTD) of the time-series data to identify voxels dominated by physiological noise. We show that the use of principal components derived from a noise ROI as regressors in a GLM of the fMRI signal can significantly reduce the temporal variance in resting state scans and increase the sensitivity of functional BOLD and perfusion-based studies.

4.3 Theory

4.3.1 CompCor Algorithm

The underlying assumption in the CompCor algorithm is that signal from a noise ROI can be used to accurately model physiological fluctuations in gray matter regions. The term "noise

ROI" refers to areas (e.g. white matter, ventricles, large vessels) in which temporal fluctuations are unlikely to modulated by neural activity and are primarily a reflection of physiological noise. The ability to model gray matter physiological noise elements is then predicated on the coherence between physiological fluctuations in noise ROI and the gray matter. A principal components analysis (PCA) is used to compactly characterize the time-series data from the noise ROI. Significant principal components are then introduced as covariates in a general linear model as an estimate of the physiological noise regressors.

In this paper we investigate the use of two methods for determining the noise ROI. The first method uses anatomical data to identify voxels that consist primarily of either white matter or cerebrospinal fluid (CSF). Since neural activation is localized to gray matter, fluctuations in white matter and CSF regions should primarily reflect signals of non-neural origin (e.g. cardiac and respiratory fluctuations).

In the second method, voxels with high temporal standard deviation (tSTD) are used to define a noise ROI. This approach is based on previous preliminary work by Lund et al. in which areas of high temporal standard deviation were found to correspond to ventricles, edge-regions, and vessels (Lund et al., 2001). The advantage of this method is that it utilizes the time-series data to identify a noise ROI without the need for an anatomical scan.

In Figure 1, we present a schematic depicting the basic algorithm in which significant principal components from a noise ROI are used as physiological noise regressors in the GLM for the gray matter signal. For functional studies, an added processing step is included in which a preliminary GLM analysis, using the appropriate design matrix ***Xh***, is used to exclude voxels from the determined noise ROI with a calculated p-value of less than 0.2. This step is performed to hedge against the possibility of removing stimulus related fluctuations.

4.3.2 General Linear Model for ASL and BOLD

The general linear model of the BOLD signal in gray matter can be represented as

$$\boldsymbol{b} = \boldsymbol{Xh} + \boldsymbol{Sd} + \boldsymbol{Pc} + \boldsymbol{n} \qquad [1]$$

where $\boldsymbol{b}$ represents the measured BOLD data, $\boldsymbol{Xh}$ represents the stimulus response where $\boldsymbol{X}$ is a $\boldsymbol{N} \times \boldsymbol{k}$ design matrix and $\boldsymbol{h}$ is a $\boldsymbol{k} \times 1$ vector of hemodynamic parameters. In the case of a block design, $\boldsymbol{X}$ reduces to a vector containing the smoothed stimulus pattern and $\boldsymbol{h}$ reduces to a scalar representing the unknown amplitude. Nuisance parameters are integrated in $\boldsymbol{Sd}$, where $\boldsymbol{S}$ is a $\boldsymbol{N} \times \boldsymbol{l}$ matrix comprised of l nuisance model functions and $\boldsymbol{d}$ is a $\boldsymbol{l} \times 1$ vector of nuisance parameters. We have also added physiological noise terms $\boldsymbol{Pc}$ where $\boldsymbol{P}$ is a $\boldsymbol{N} \times \boldsymbol{m}$ matrix containing m regressors and $\boldsymbol{c}$ represents the unknown regressor weights. Finally, $\boldsymbol{n}$ represents the additive noise term.

A general linear model (GLM) for ASL data in gray matter can be written as

$$\boldsymbol{p} = \boldsymbol{Xh}_{\boldsymbol{BOLD}} + \boldsymbol{MXh}_{\boldsymbol{perf}} + \boldsymbol{Sd} + \boldsymbol{Pc} + \boldsymbol{n} \qquad [2]$$

where $\boldsymbol{p}$ is the acquired raw data representing interleaved tag and control images. In this model, the term modeling perfusion $\boldsymbol{Xh}_{\boldsymbol{perf}}$ is modulated by a diagonal matrix, $\boldsymbol{M}$, consisting of alternating -1's and 1's for the tag and control images, respectively (Mumford et al., 2006; Restom et al., 2006). The term $\boldsymbol{Xh}_{\boldsymbol{BOLD}}$ models a BOLD weighted static tissue component.

In a noise ROI, where we expect no stimulus-related response, the GLM reduces to $\boldsymbol{b} = \boldsymbol{Sd} + \boldsymbol{Pc} + \boldsymbol{n}$ or $\boldsymbol{p} = \boldsymbol{Sd} + \boldsymbol{Pc} + \boldsymbol{n}$ for BOLD and perfusion data, respectively. An assumption of CompCor is that the significant principal components from the noise ROI can be used as an estimate $\boldsymbol{P}_{\boldsymbol{est}}$ of the physiological regressors $\boldsymbol{P}$.

4.4 Methods

4.4.1 Experimental Protocol

Ten healthy subjects (ages 23 to 39) participated in the study after giving informed consent. Each subject viewed a periodic single trial visual stimulus consisting of a 20-second initial “off” period followed by 5 cycles of a 4 second “on” period and a 40 second “off” period. In addition to a periodic design, each subject viewed a block design consisting of 4 cycles of a 20 second “on” period and a 40 second “off” period. During the “on” periods, a full-field, full contrast radial 8 Hz flickering checkerboard was displayed, while the “off” periods consisted of a gray background of luminance equal to the average luminance of the “on” period. All subjects also underwent two resting-state scans, during which the subject was presented with the “off” condition for 3 minutes.

4.4.2 Imaging Protocol

Imaging data were collected on a GE Signa Excite 3 Tesla whole body system with a body transmit coil and an eight channel receive coil. During one of the resting-state and the block design scan, data were acquired with a PICORE QUIPPS II (Wong et al., 1998) arterial spin labeling (ASL) sequence (TR= 2s , TI1/TI2= 600/1500ms, 10 cm tag thickness, and a 1 cm tag-slice gap) with a dual echo spiral readout (TE1/TE2=9.1/30 ms, FOV=24 cm, 64x64 matrix, and a flip angle= 90 degrees). Small bipolar crusher gradients were included to remove signal from large vessels (b=2 s/mm^2). Three oblique axial 8 mm slices were prescribed about the calcarine sulcus for this ASL run. During the periodic single trial runs, BOLD-weighted images were acquired with a spiral readout (TE=25ms, TR=500 ms, FOV=24cm, 64x64 matrix, and a flip-angle of 45 degrees). In all ten subjects, these BOLD runs used the same slice prescription as the ASL runs. For all periodic single trials, 480 volumes at a TR of 500 ms were acquired. The second resting state scan was acquired with the following BOLD imaging parameters with a spiral readout (TE=25ms, TR=250 ms, FOV=24cm, 64x64 matrix, and a flip-angle of 40 degrees).

A high resolution structural scan was acquired with a magnetization prepared 3D fast spoiled gradient acquisition in the steady state (FSPGR) sequence (TI 450ms, TR 7.9ms, TE 3.1ms, 12 degree flip angle, FOV 25x25x16 cm, matrix 256x256x124).

Cardiac pulse and respiratory effort data were monitored using a pulse oximeter (InVivo) and a respiratory effort transducer (BIOPAC), respectively. The pulse oximeter was placed on the subject's left index finger, and the respiratory effort belt was placed around the subject's abdomen. Physiological data were sampled at 40 samples per second using a multi-channel data acquisition board (National Instruments).

4.4.3 Data Analysis

Preprocessing

All images were coregistered using AFNI software (Cox, 1996) and prewhitened using an AR1 model prior to subsequent analysis (Burock et al., 2000; Woolrich et al., 2001). An GLM analysis was then performed using RETROICOR type regressors to construct the physiological noise matrix, $\boldsymbol{P}$, as defined in equations 1 and 2 for ASL and BOLD based imaging, respectively. (Glover et al., 2000; Restom et al., 2006). In addition to statistical inference, this analysis was used to identify cardiac and respiratory components, which will be used as a basis for comparison to elements removed by application of CompCor.

Anatomical Definition of Noise ROI

Anatomical data were segmented into gray matter, white matter, and CSF partial volume maps using the FAST algorithm available in the FSL software package (Smith et al., 2004). Tissue partial volume maps were linearly interpolated to the resolution of the functional data series using AFNI (Cox 1996). In order to form white matter ROIs, the white matter partial volume maps were thresholded at a partial volume fraction of 0.99 and then eroded by two voxels in each direction to minimize partial voluming with gray matter. The erosion process helps identify deep white matter areas. CSF-only voxels were determined by first thresholding the CSF partial volume maps at 0.99 and then applying a 3-dimensional nearest-neighbor criteria to minimize multiple tissue partial voluming. Since CSF regions are typically small compared to white matter regions mask, erosion was not applied.

CSF and white matter ROIs were combined to form the anatomically defined noise ROI, subsequently referred to as noise ROI_{anat}. Figure 2 depicts the significant areas of white matter and cerebrospinal fluid (CSF), as denoted by the magenta voxels, overlayed on their respective partial volume maps from subject 1.

tSTD Based Determination of Noise ROI

In a preliminary abstract, Lund et al. (2001) showed that voxel time courses with a relatively high temporal standard deviation were dominated by physiological noise. They observed that these voxels occurred in edge-regions, ventricles, and in areas close to large vessels. In their approach, they manually selected five pixels with high temporal standard deviation that appeared to represent physiological fluctuation. The time-series from these voxels were then included as nuisance covariates in a GLM, resulting in a marked improvement in detection power (Lund et al., 2001). Here we extend the prior work by first using the temporal standard deviation to select voxels in an unsupervised fashion and then using principal components analysis to reduce the dimensionality of the data. To determine the number of voxels to include in the ROI, we examined the relation between measures of physiological noise and measures of temporal standard deviation. For each voxel, we defined the fractional variance of physiological noise as the ratio of the variance of the time series due to the physiological noise regressors (as determined with RETROICOR) to the variance of the original time series (after removal of constant and linear trends). The fractional variance of physiological noise was then compared to the temporal standard deviation on a per-voxel basis. We denote the ROI identified with this approach as the noise $\mathrm{ROI}_{\mathrm{tSTD}}$. We found that including the top 20 voxels per slice based on tSTD provided robust removal of physiological fluctuations as quantified by the mean reduction in tSTD in gray matter (partial voluming > 0.9) across subjects for resting BOLD runs. This was based on evaluating the performance of CompCor with inclusion of 5,10, 20, and 40 voxels per slice. Using 20 voxels significantly outperformed selecting only 5 and10 voxels but resulted in no significant difference compared to inclusion of 40 voxels. We use a simple selection criteria here to demonstrate proof-of-principle and realize that more sophisticated and dynamic selection methodologies might result in greater gains. However, this will be the focus of subsequent work.

Exclusion of stimulus-related components

To further refine the definition of the noise ROI for runs involving functional stimulus, the voxel time courses within the noise ROI are correlated with the stimulus-related reference function. Any voxels with a p-value less than 0.2 was excluded from the noise ROI. Numerical simulations (shown in appendix) indicate that a excluding voxels with a p-value less than 0.2 (R-value <0.1 for block design) with the reference function prevents degradation of performance due to incorporation of stimulus related fluctuations in the determined prinicipal components. Here we use an even more conservative threshold to hedge against removal of stimulus correlated fluctuations.

Determination of Principal Components

Voxels time-series from the noise ROI (either anatomical or tSTD) are placed in a matrix $\boldsymbol{M}$ with dimensions $\boldsymbol{Nxm}$, representing the dimensions of time and voxels, respectively. The constant and linear trends of the columns matrix $\boldsymbol{M}$ are removed prior to column-wise variance normalization. The covariance matrix, $\boldsymbol{C} = \boldsymbol{MM'}$, is constructed and decomposed into its principal components. In our implementation we utilize the singular value decomposition (SVD) algorithm to perform the PCA, although other algorithms could also be used.

The number of significant principal components is determined using a modified version of the “broken stick” method described in (Jackson, 1993). This method identifies the point at which principal values begin to describe mostly random variation in the data. A Monte-Carlo simulation is first used to generate a statistical representation of expected principal values derived from normally distributed data of rank equal to the matrix $\boldsymbol{M}$. This statistical distribution is then compared to the computed principal values from the data. A threshold is defined at the point where the difference between the calculated principal values from the data are no longer significantly different ($p<0.05$) from the calculated distribution. Based on this method, we found an average of 6.3 ± 0.52 and 4.5 ± 0.38 significant principal components for BOLD and ASL runs, respectively, when using the anatomical noise ROI. For the noise $\mathrm{ROI}_{\mathrm{tSTD}}$,there were an average of 5.9 ± 0.74 and 4.2 ± 0.59 principal components for the BOLD and ASL runs, respectively.

Quantitative Assessment of Performance

For each subject, average power spectra were obtained by computing the power spectra for each voxel time-series of interest, averaging the spectra across voxels within the gray matter voxels (partial volume threshold of 0.9), and then normalizing by the peak power over all frequencies. The average power spectra of physiological noise components estimated by RETROICOR was used to identify the peak frequencies related to the cardiac and respiratory noise elements. Frequencies for which the average cardiac or respiratory components had a normalized power greater than 0.1 were then used to define cardiac and respiratory frequency bands, respectively.

Spectral coherence analysis was used to compare components removed by RETROICOR with those removed by CompCor. The average spectral coherence over a frequency band, f_{band}, is defined (Stoica et al., 1997)

$$\boldsymbol{C}_{xy}(\boldsymbol{f}) = \frac{\left|\boldsymbol{P}_{xy}(\boldsymbol{f}_{band})\right|^2}{\left|\boldsymbol{P}_{xx}(\boldsymbol{f}_{band})\right|\left|\boldsymbol{P}_{yy}(\boldsymbol{f}_{band})\right|}$$

where the $\boldsymbol{P}_{xx}$ and $\boldsymbol{P}_{yy}$ are the power spectra of time-series x and y, respectively, and $\boldsymbol{P}_{xy}$ is the cross power spectral density. For each voxel the spectral coherence across the cardiac and respiratory bands was computed. The average spectral coherence across voxels in gray matter (partial volume > 0.9) was then computed.

In order to quantify the degree of noise reduction in the resting state scans, the temporal standard deviation was computed for all voxels within gray matter (partial volume >0.9). A paired t-test was then used to assess whether CompCor significantly altered the mean temporal standard deviation across voxels per subject.

F-statistics were computed using the appropriate GLM for the BOLD and ASL time-series under the following conditions: 1) no inclusion of physiological noise regressors (e.g. no correction), 2) inclusion of RETROICOR regressors, 3) inclusion of CompCor regressors derived from the noise ROI_{anat}, and 4) inclusion of CompCor regressors derived from the noise ROI_{tSTD}. The reference functions, h_{BOLD} and h_{perf}, were formed by convolving the appropriate stimulus pattern with a gamma density function of the form $h(t) = (\tau n!)^{-1}((t - \Delta t)/\tau) \exp(-(t - \Delta t)/\tau)$ for $t \geq \Delta t$ and 0 otherwise, with $\tau = 1.2$, $n = 3$ and $\Delta t = 1$ (Boynton et al., 1996). A constant term and linear trend term were included as nuisance regressors in the analysis. A functional region-of-interest was determined for each subject by thresholding the F-values (corresponding to data with no correction) at 5 and 100, corresponding to p-values of 0.03 and 0.001, for the ASL and BOLD functional runs, respectively. These values were chosen to yield approximately the same number of activated voxels for the ASL and BOLD functional runs and are consistent with thresholds previously used to investigate physiological noise reduction for ASL (Restom et al., 2006). A paired t-test was used to assess whether CompCor significantly increased the number of activated voxels for periodic BOLD and block ASL runs as compared to no correction on a per subject basis.

4.5 Results

Figure 5 characterizes the elements removed from gray matter regions (partial voluming >0.9) from the resting BOLD run from subject 1. The normalized average power spectra are presented. With application of RETORICOR (panel a) cardiac (~1.2 Hz) and respiratory (~0.2Hz) cpmponents are removed. Application of CompCor using either the noise noise $\mathrm{ROI}_{\mathrm{anat}}$ or noise $\mathrm{nROI}_{\mathrm{tSTD}}$, results in removal of elements consistent with cardiac and respiratory elements. An additional 1/f component is removed with application of noise $\mathrm{ROI}_{\mathrm{anat}}$ as depicted in panel b).

As an example of the noise elements removed with each of the correction schemes, presented as average power spectra, from Subject 1 are presented in Figure 6. Cardiac and respiratory elements are aliased due to the long TR and are represented in red and green lines, respectively. The spectra of elements removed by application of CompCor using the noise ROI (anat) (panel b) is consistent with cardiac and respiratory elements whereas using the noise ROI (tSTD) removes primarily a cardiac component (see panel c).

As described in the Methods section, the average spectral coherence for each subject was computed between noise components identified by CompCor and the cardiac and respiratory components identified by RETROICOR. For CompCor with noise $\mathrm{ROI}_{\mathrm{anat}}$ applied to the resting BOLD runs, the average voxel-wise spectral coherence and standard error values across subjects (N = 10) were 0.67 ± 0.08 and 0.80 ± 0.05 for respiratory and cardiac elements, respectively. With application of CompCor using noise ROI_{tSTD} , average values for the spectral coherence with respiratory and cardiac elements were 0.62 ± 0.10 and 0.86 ± 0.07, respectively. For resting ASL runs the mean spectral coherences when using CompCor with noise ROI_{anat} were 0.79 ± 0.03 and 0.65 ± 0.06 for respiratory and cardiac elements, respectively. With the application of CompCor using noise ROI_{tSTD} , average values for the spectral coherence with respiratory and cardiac elements were 0.82 ± 0.03 and 0.69 ± 0.06, respectively. See tables 2 and 3 for a summary of these results.

The impact of CompCor and RETROICOR on the average temporal standard deviation of the resting BOLD and ASL runs are presented in Figure 7, with associated standard error bars across subjects (N = 10). Panels a) and b) show the mean temporal standard deviation (tSTD) in gray matter (partial voluming >0.9) in resting BOLD and ASL, respectively, with application of RETROICOR and the two variants of CompCor. As compared to no correction, RETROICOR, significantly ($p<0.001$) reduced the tSTD in the resting BOLD run from 84.2 to 78.2 whereas application of CompCor using noise ROI_{anat} and CompCor using noise ROI_{tSTD} resulted in even greater reductions to mean values of 63.2 ($p<0.001$) and 58.4 ($p<0.001$), respectively. In resting ASL data the tSTD was reduced from 56.0 to 45.6 ($p <0.001$), 44.7 ($p<0.001$), and 42.8 ($p<0.001$), with the application of RETROICOR, CompCor using noise ROI_{anat}, and CompCor using noise ROI_{tSTD} , respectively.

Bar graphs comparing the effect of the various correction schemes on the number of activated voxels for the functional ASL block and BOLD periodic runs are shown in Figure 8. The number of activated voxels for a periodic BOLD run (panel a) was significantly increased ($p<0.001$) from 127 to 147.4, 161.2, and 179.9 with the application of RETROICOR, CompCor using noise ROI_{anat} , and CompCor using noise ROI_{tSTD}, respectively. In ASL block functional runs, the number of voxels passing the F-thresholds increased from 105.9 to 119.6 ($p=0.07$), 151.1 ($p=0.004$), and 160.3 ($p=0.003$) with application of RETROICOR, CompCor using noise

ROI_{anat} , and CompCor using noise ROI_{tSTD}, respectively. For both functional BOLD and ASL runs, CompCor using noise ROI_{anat} resulted in greater increases than CompCor using noise ROI_{tSTD} .

4.6 Discussion

In this paper, we have examined whether signal components derived from noise regions of interest, unlikely to be modulated by neural activity. can be used to reduce the contributions of physiological noise components within activated regions in the analysis of ASL and BOLD data. We considered two methods for the determination of the noise ROIs: 1) Anatomical identification of significant areas of CSF and white matter and 2) Definition of noise regions based upon their temporal standard deviation. We demonstrated that the application of CompCor using either ROI significantly reduces the temporal standard deviation of both resting state BOLD and ASL data. Additionally, we have shown that CompCor with either ROI leads to a marked improvement in sensitivity during visual stimulus as quantified by the number of significantly activated voxels for both an ASL block design experiment and a periodic BOLD design experiment.

In each implementation of CompCor, using either noise ROI_{anat} or noise ROI_{tSTD}, there are possible complications arising from introduction of bias and from the accurate determination of noise ROI's. Bias may result in removing components that are related to activation instead of physiological noise. For instance, although CompCor using the noise ROI_{tSTD} resulted in significant decreases in temporal STD and increases in sensitivity, it relies on the ability to accurately exclude voxels that may include activation. Accurate exclusion may prove to be difficult when dealing with complex event-related paradigms for which the expected response may not be well defined or for resting state scans aimed at studying functional connectivity.

Although requiring an additional scan to obtain anatomical data, CompCor using anatomically defined noise ROI provides an unbiased way of removing physiological fluctuations, since neural activation should be absent from regions of white matter and CSF. However, accurate tissue information must be obtained and this can be a concern with various slice prescriptions or when anatomical to functional alignment is problematic (e.g. due to subject motion) and result in possible bias. With care, application of CompCor with an anatomically determined noise ROI, should allow for the robust identification and removal of physiological fluctuations.

In our implementation of CompCor we use a simplified analysis to determine the number of significant principal components to retain. Although more sophisticated methods exist to estimate the latent dimensionality of the noise, we find that the results are fairly insensitive to the exact number of components used in the GLM.

4.7 Conclusion

We have shown that application of CompCor to ASL and BOLD fMRI time-series can significantly reduce physiological noise. CompCor does not require external monitoring and can applied in an automated fashion to reduce the confounding effect of physiological fluctuations on fMRI time-series.

Acknowledgments

The authors thank Dr. Peter Costandi, Khaled Restom and Dr. Joanna Perthen for their valued assistance with the preparation of this paper. This work was supported in part by a Biomedical Engineering Research grant from the Whitaker Foundation and by NIH Grant R01NS051661.

4.8 Appendix . Reduction of Physiological Noise in Simulated fMRI Data

The CompCor algorithm relies on the ability to accurately remove physiological noise without removing stimulus related fluctuations. In an ideal situation, the noise ROI would only contain voxels from the noise-only distribution, H_0 , and determined principal components would describe only the noise subspace. However in practice, a percentage of noise ROI voxels may contain stimulus correlated time-series, taken from a signal+noise distribution H_1, and an exclusion criteria must be used to hedge against removing stimulus correlated components. Here we examine the effect of the choice of correlation coefficient exclusion criteria on the resulting performance of CompCor.

The general linear model of the BOLD signal with activation is represented as

$$\boldsymbol{b}_{\boldsymbol{simulated}} = \boldsymbol{Xh} + \boldsymbol{Sd} + \boldsymbol{Pc} + \boldsymbol{n} \qquad \text{[A.1]}$$

where $b_{simulated}$ represents the overall simulated BOLD response, $\boldsymbol{Xh}$ represents the stimulus response where $\boldsymbol{X}$ is a $\boldsymbol{N} \times \boldsymbol{k}$ design matrix and $\boldsymbol{h}$ is a $\boldsymbol{k} \times 1$ vector of hemodynamic parameters. Nuisance parameters, constant and linear terms, are integrated in $\boldsymbol{Sd}$ and physiological noise terms in $\boldsymbol{Pc}$ where $\boldsymbol{P}$ is a $\boldsymbol{N} \times \boldsymbol{m}$ matrix containing m regressors and $\boldsymbol{c}$ are unknown regressor weights. Finally, $\boldsymbol{n}$ represents the additive noise term. H_1 voxels include a stimulus response while H_0 do not include an $\boldsymbol{Xh}$ term.

As is the case in fMRI data analysis, knowledge of the physiological noise parameters is not available and GLM analysis is performed using an estimate of the physiological noise regressors:

$$\boldsymbol{b}_{\boldsymbol{simulated}} = \boldsymbol{X\hat{h}} + \boldsymbol{S\hat{d}} + \boldsymbol{P}_{\boldsymbol{est}}\boldsymbol{\hat{c}} + \boldsymbol{n} \qquad \text{[A.2]}$$

where the $\boldsymbol{\hat{h}}$, $\boldsymbol{\hat{d}}$, $\boldsymbol{\hat{c}}$ and $\boldsymbol{\hat{n}}$ represent estimates of the true stimulus amplitude, nuisance term, physiological noise, and residual noise. In this formulation, the physiological noise is not explicitly known so an estimate, $\boldsymbol{P}_{est}$, is used. In the CompCor algorithm $\boldsymbol{P}_{est}$ is determined by performing a principal component analysis of noise-only voxels, H_0. A threshold based on a calculated correlation coefficient with the stimulus reference function is used to exclude voxels that may contain stimulus-related fluctuations. Here we explicitly characterize the ability of the CompCor algorithm to remove physiological noise as a function of the correlation coefficient threshold.

A Monte Carlo simulation was used to characterize the CompCor process on removing known physiological data. Individual voxel responses (N=5000) were generated by randomly selecting the relative weights of components within the GLM framework. Noise only voxels, H_0, and noise with activation, H_1, were generated. Physiological regressors were generated at frequencies consistent with cardiac (0.9 Hz) and respiration (0.3 Hz) with randomly generated phases to represent possible phase lags between voxels. Physiological noise weights were chosen from a distribution governed by N(0,0.3). A constant term was included as a nuisance term with $\boldsymbol{d}$ chosen from an uniform distribution, U(0,1). The additive noise term, n, were generated from a normal distribution, N(0,1). For H_1 voxels, the stimulus response, $\boldsymbol{Xh}$, was generated using a block design, 20 second initial off period followed by 4 cycles of 20 seconds on and 40 seconds off. The stimulus weight was chosen as 0.3 to simulate a worst-case scenario with a low-level stimulus response.

The estimation of the physiological noise regressors is determined using a principal component analysis of voxel time-series below an absolute value of correlation coefficients (CC). CC's were determined using the reference function and a simplified version of the GLM without the inclusion of physiological noise terms, Pc.

Panel a) in figure A.1 is a representation of the resulting histogram of correlation coefficients using a equal number of H_1 and H_0 voxels. The solid-line distributions represent the H_0 and H_1 without inclusion of physiological noise and the dotted-line distributions reflect the effect of physiological noise on the respective distributions. The H_1 distribution is centered on a correlation coefficient of 0.3 before inclusion of physiological noise and 0.2 after. As expected, the added noise degrades the calculated CC's.

If a principal component analysis is performed on the H_0 voxel time-series, the physiological noise subspace can be compactly characterized with the use of only five principal components. Principal components are used as columns of the estimated physiological noise matrix $\boldsymbol{P}_{est}$ allowing for the removal of physiological noise. However, in practice we do not have perfect knowledge of H_0 and H_1 voxels and a CC threshold must be used to select voxels to be included in the PCA. As the absolute value of the CC threshold is increased we would expect more H_1 voxels being incorporated in the PCA analysis and the possibility to remove stimulus-related fluctuations is increased. Panel b) of figure A1, depicts the maximum correlation of the identified principal components and the reference function. As the CC threshold increases beyond ~0.2 , the derived PC's begin to become increasingly more correlated. Inclusion of the PC's in the GLM will decrease the estimated stimulus response weight and degrade performance.

As the CC threshold is increased for inclusion of voxels in the subsequent principal component analysis, the degree of correction is reduced, as depicted by the ROC curves provided in panel c) in figure A.1. This is a result of the confounding effects of stimulus related fluctuations. The dotted line is a representation of the probability of detection (pD) versus the probability of false alarm (pFa) of the uncorrected data. Using a low CC threshold, in which H_1 voxels are excluded from PCA analysis, results in increased pD with a decrease in pFa, as depicted in the upward shift of the ROC curve. However, at a threshold of 0.16, the resulting performance of using the correction is worse than the uncorrected data.

Panel d) depicts the area under the ROC curve as a function of CC threshold. This is a non-parametric normalized measure of performance and it is evident that the overall performance is degraded when using a CC threshold beyond 0.2. However, performance is robust below this threshold and based on this simulation we choose to use a conservative exclusion criteria of 0.1 in our presentation of CompCor.

4.9 Figures and Tables

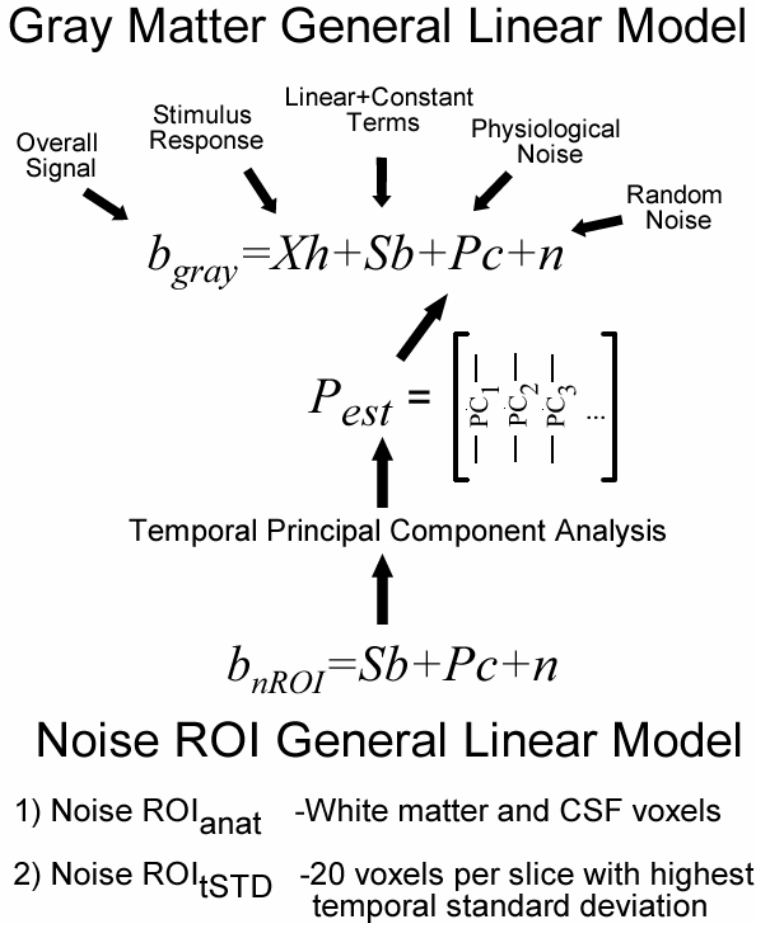

Figure 4.1. Schematic of the CompCor algorithm in which significant principal components derived from time-series data within noise regions-of-interest are used to form an estimate, $\boldsymbol{P}_{est}$, of the physiological noise matrix, $\boldsymbol{P}$. Incorporation of $\boldsymbol{P}_{est}$ into the general linear model for gray matter allows for estimation and removal of physiological fluctuations.

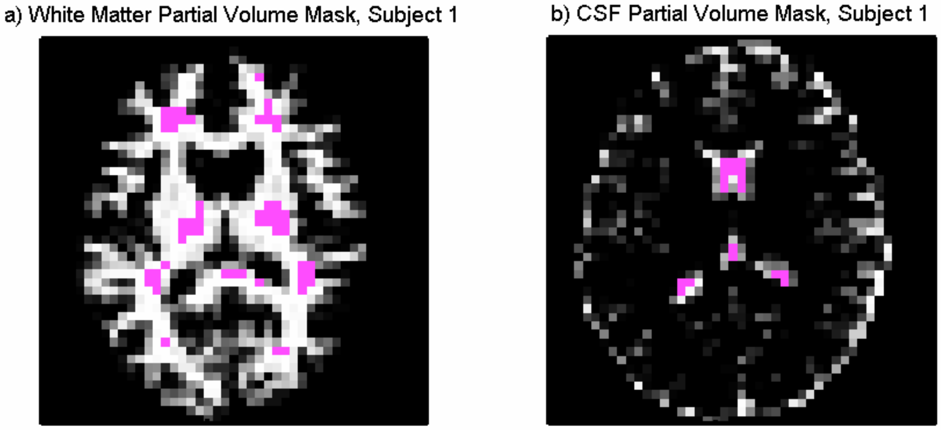

Figure 4.2. Areas with a high fraction of white matter and cerebrospinal fluid (CSF), as denoted by the magenta voxels, overlaid on their respective partial volume maps from a representative slice from Subject 1. White matter-only areas (panel a) were determined by first thresholding the white matter partial volume fraction map at 0.99 and then performing a map erosion by two pixels to minimize the effect of partial voluming with other tissue types. Panel b) displays CSF-only areas with a partial volume fraction greater than 0.99 with application of a nearest neighbor clustering criteria.

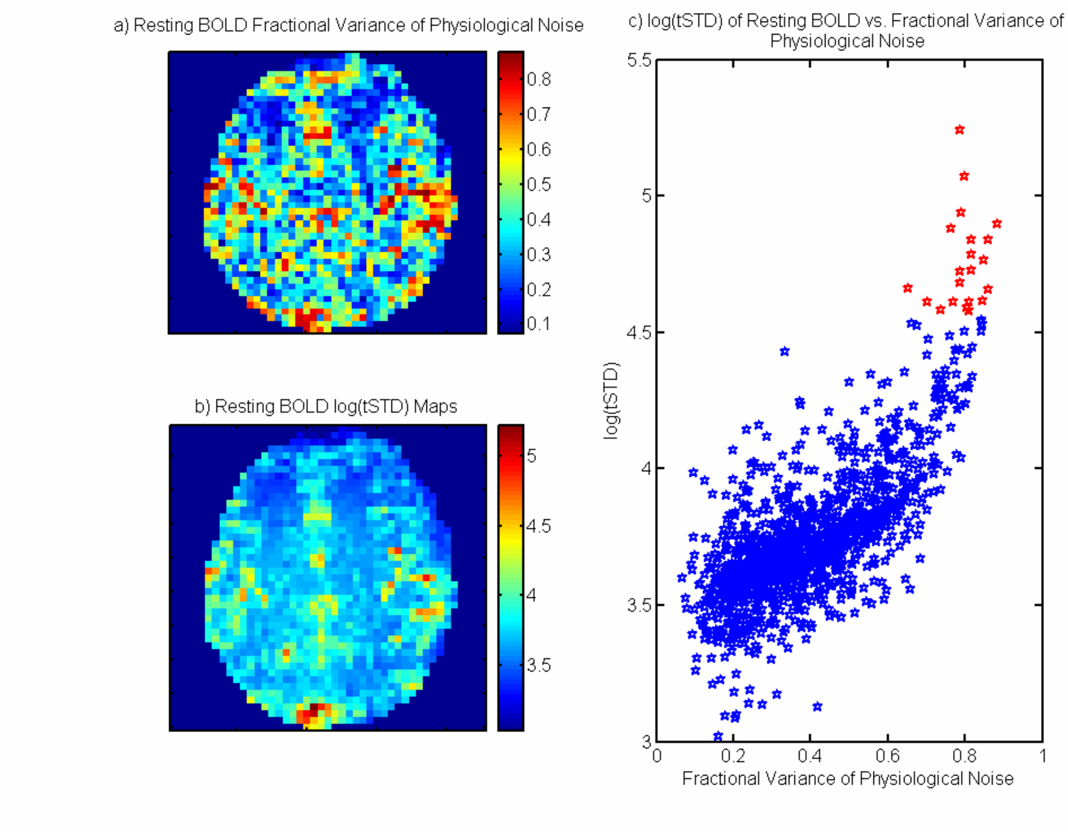

Figure 4.3. Panel a) is a spatial map of the fraction of the variance of physiological noise to the overall signal variance for the resting BOLD scan from a representative slice in subject 1. Panel c) compares the log(tSTD) to the fractional variance of physiological noise per voxel. Data points in red represent the twenty voxels with the highest tSTD and correspond to a high fraction of physiological noise. Areas of high fractional variance of physiological noise correspond to areas of high temporal standard deviation (tSTD) of the raw time-series as depicted in panel b).

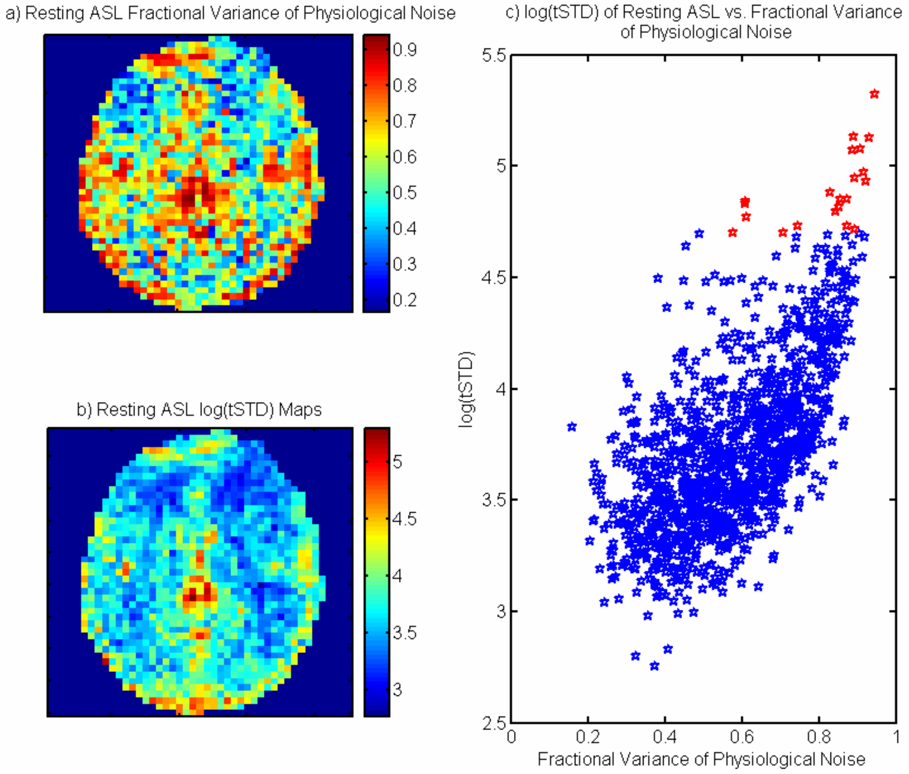
a) Resting ASL Fractional Variance of Physiological Noise

b) Resting ASL log(tSTD) Maps

c) log(tSTD) of Resting ASL vs. Fractional Variance of Physiological Noise

Figure 4.4. Panel a) is a spatial map of the fraction of the variance of physiological noise to the overall signal variance for the resting ASL scan from a representative slice in subject 1. Panel c) compares the log(tSTD) to the fractional variance of physiological noise per voxel. Data points in red represent the twenty voxels with the highest tSTD and correspond to a high fraction of physiological noise. Areas of high fractional variance of physiological noise correspond to areas of high temporal standard deviation (tSTD) of the raw time-series as depicted in panel b).

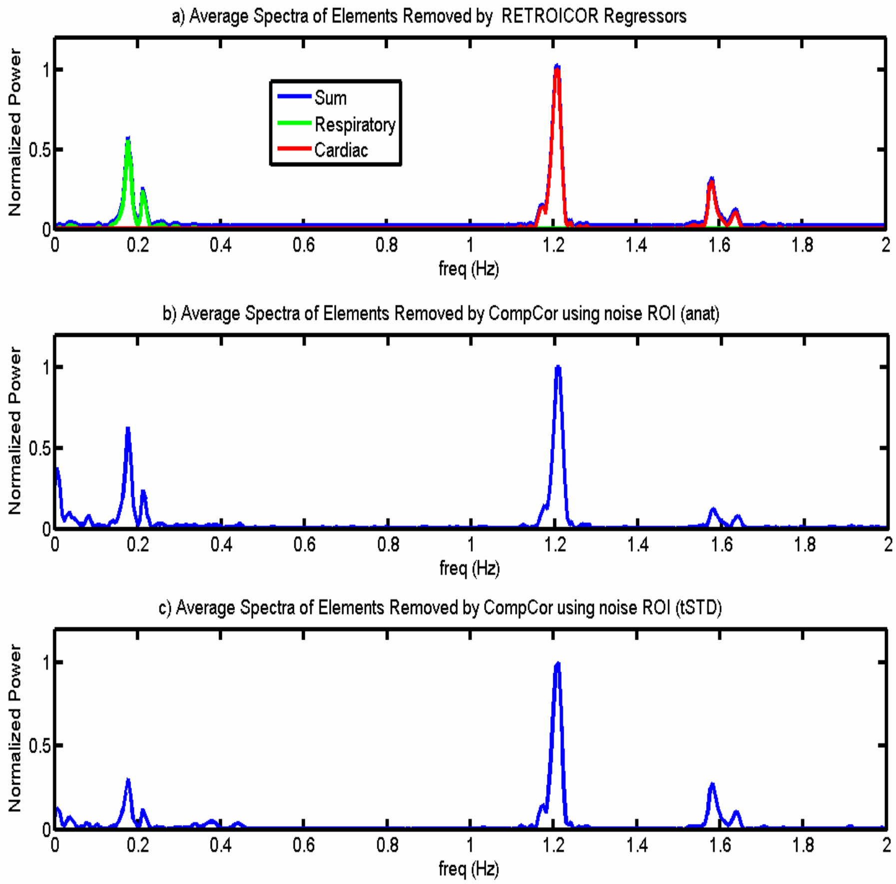

Figure 4.5. Average normalized power spectra of components removed from gray matter (partial volume >0.9) with the application of various correction schemes to the resting BOLD run from subject 1. As shown in panel a, cardiac and respiratory elements removed by RETROICOR are located at 0.2 and 1.2 Hz, respectively. Application of CompCor using either noise ROI$_{anat}$ (panel b) or noise ROI$_{tSTD}$ (panel c) removes components similar to the cardiac and respiratory elements identified by RETROICOR. The use of noise ROI$_{anat}$ also removes a 1/f noise component as evident in panel b).

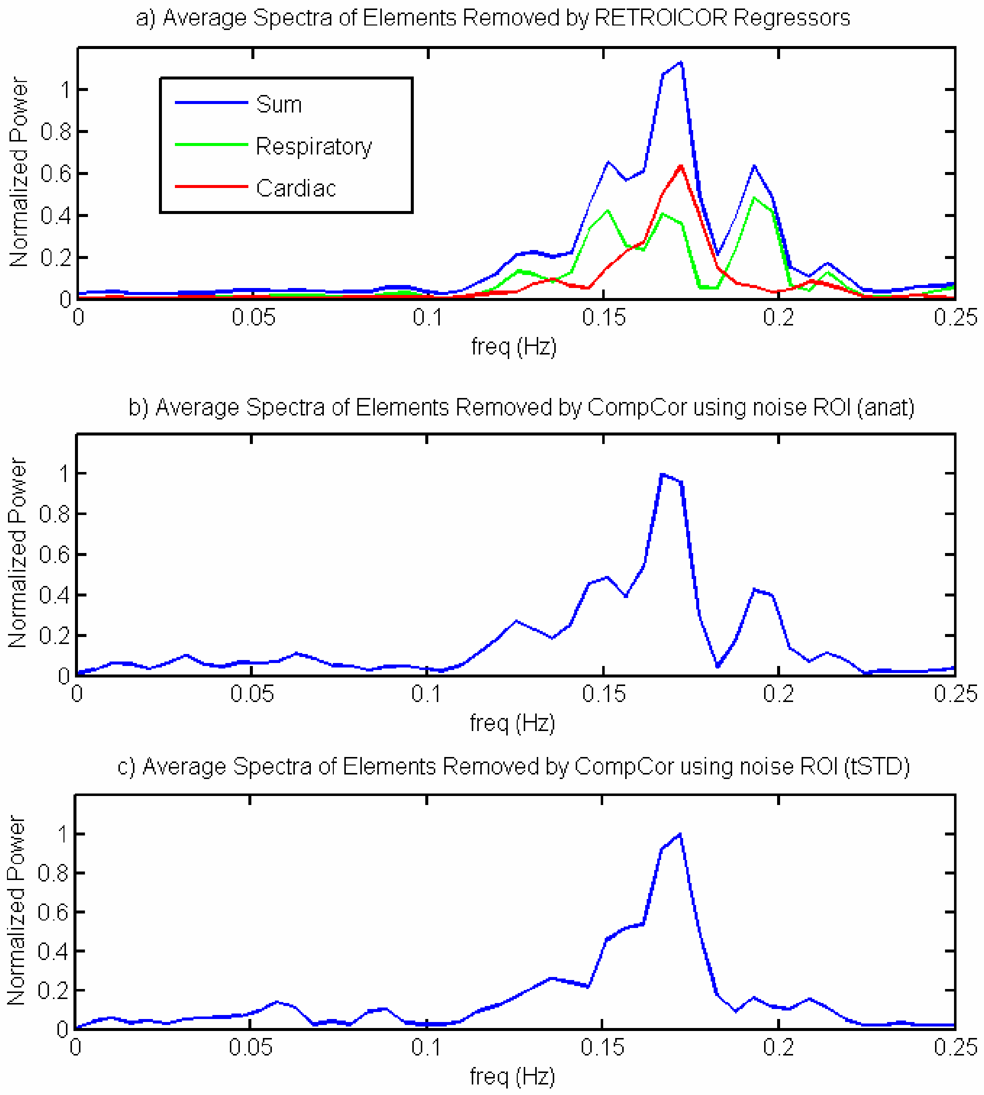

Figure 4.6. Average normalized power spectra of components removed from gray matter (partial volume >0.9) with application of various correction schemes to the resting ASL run from subject 1. As shown in panel a, cardiac (red) and respiratory (green) elements identified by RETROICOR are aliased due to the long TR. The power spectra of components removed by application of CompCor using the noise ROI_{anat} (panel b) is similar to the sum of the cardiac and respiratory elements identified by RETROICOR. In contrast, CompCor with the noise ROI (tSTD) removes primarily a cardiac component (see panel c).

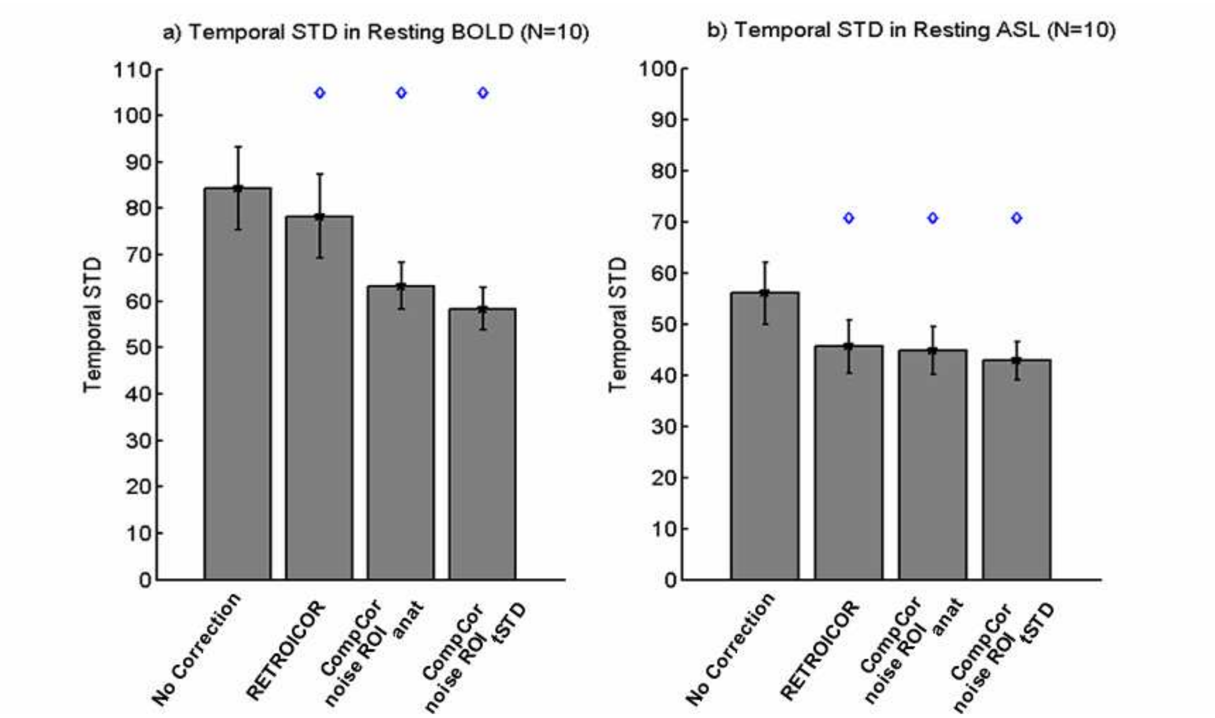

Figure 4.7. Average reduction across subjects (N=10) in the mean temporal standard deviation across voxels with application of RETROICOR and CompCor in both resting BOLD (panel a) and ASL (panel b) runs. Standard error bars represent the standard error across subjects. Diamonds represent a significant difference ($p<0.01$) between the mean temporal standard deviation across voxels per subject when no correction is applied and the standard deviation after removal of physiological noise with use of either RETROICOR or the two variants of CompCor. A paired t-test was used to assess significance.

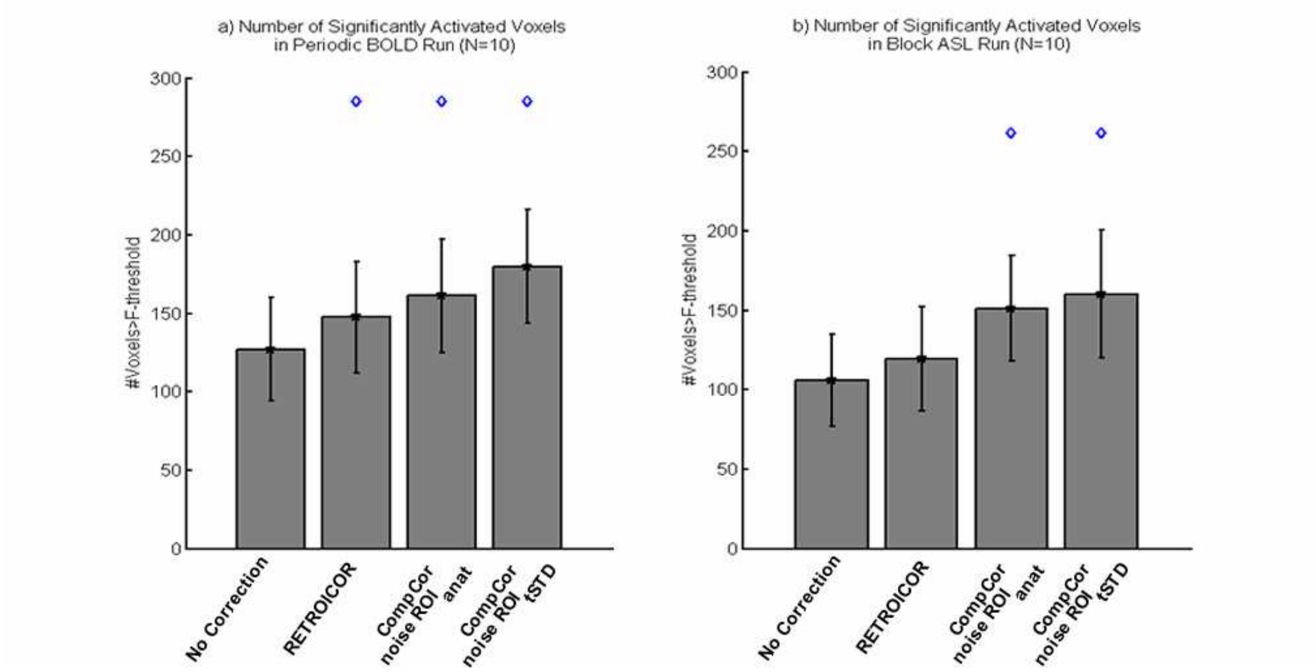

Figure 4.8. Average number of significantly activated voxels across subjects (N=10) with application of RETROICOR and CompCor for both periodic BOLD (panel a) and block ASL (panel b) runs. Standard error bars represent the standard error across subjects. Diamonds represent a significant difference ($p<0.01$) between the number of activated voxels per subject when no correction is applied and the number after removal of physiological noise with use of either RETROICOR or the two variants of CompCor. A paired t-test was used to assess significance.

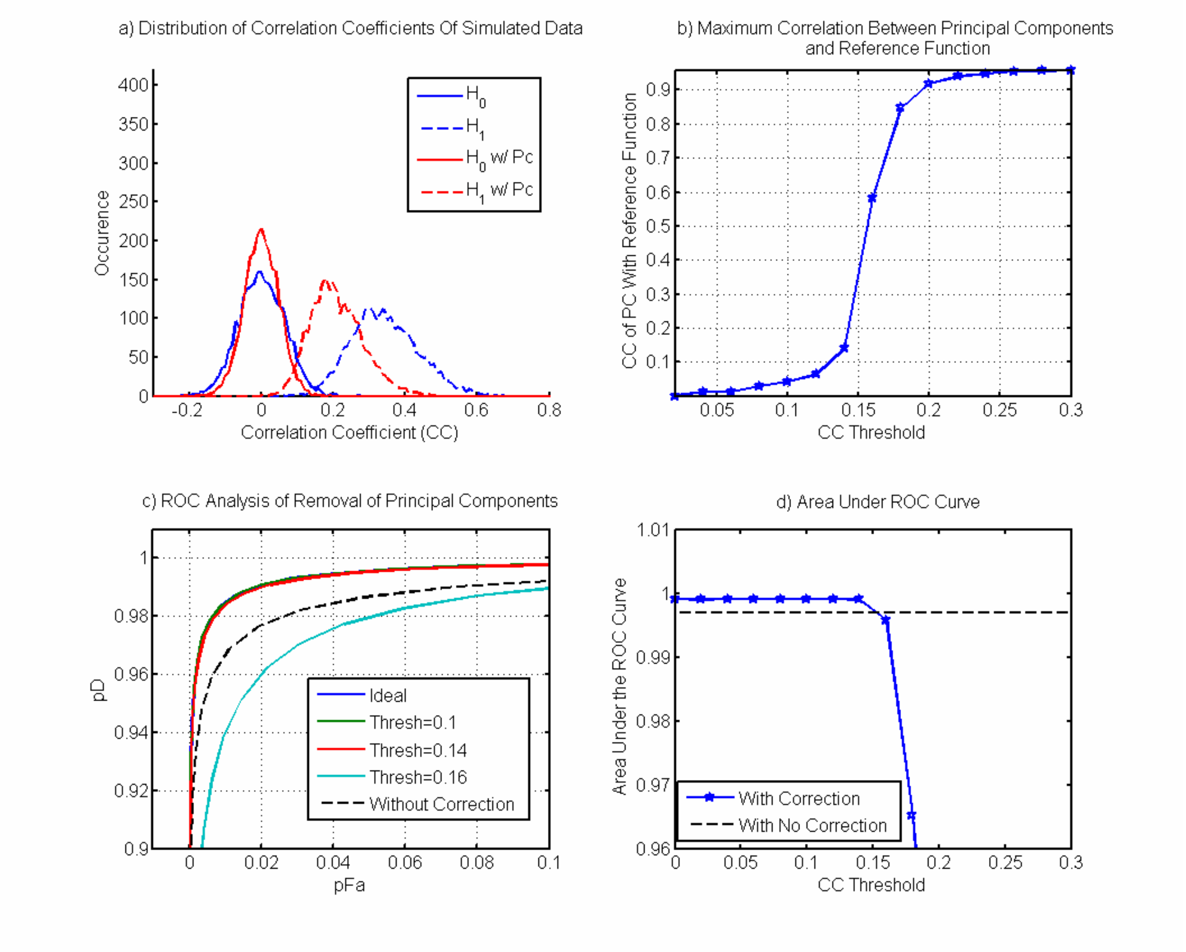

Figure 4.9. Effect of physiological noise and application of CompCor on simulated fMRI responses. Panel a) is a histogram of resulting correlation coefficients between the generated time-series and the reference function. The histograms in blue represent the H_0 and H_1 distributions without the inclusion of physiological noise. The histograms in red depict the degrading effect of physiological noise on the H_1 distribution. Panel b) characterizes the effect of the CC threshold on the derived principal components. As the CC increases stimulus-correlated elements in the principal components become evident. This then results in degradation of performance as shown by the downward shift of the cyan ROC curve with respect to the dotted line representing performance without correction in panel c). Panel d) provides a non-parametric visualization of performance and degradation occurs beyond a CC of 0.15.

Tables 4.1. Average number of principal components used in CompCor for resting BOLD and ASL runs (N=10). Average shown with standard error in parentheses.

	BOLD	ASL
CompCor (noise ROI anat)	6.3 (0.52)	4.5 (0.38)
CompCor (noise ROI tSTD)	5.9 (0.74)	4.2 (0.59)

Tables 4.2. Spectral coherence of components removed by CompCor and identified as cardiac and respiratory noise by RETROICOR. Resting BOLD runs (N=10). Average coherence shown with standard error in parentheses.

	Respiratory Noise	Cardiac Noise
CompCor (noise ROI anat)	0.67 (0.08)	0.80 (0.05)
CompCor (noise ROI tSTD)	0.62 (0.10)	0.86 (0.07)

Tables 4.3. Spectral coherence of components removed by CompCor and identified as cardiac and respiratory noise by RETROICOR. Resting ASL runs (N=10). Average coherence shown with standard error in parentheses.

	Respiratory Noise	Cardiac Noise
CompCor (noise ROI anat)	0.79 (0.03)	0.65 (0.05)
CompCor (noise ROI tSTD)	0.81 (0.03)	0.70 (0.06)

4.10 References

Beckmann C. F. and Smith S. M. (2004) Probabilistic independent component analysis for functional magnetic resonance imaging. *IEEE Trans Med Imaging*. 23, 137-152.

Birn R. M., Diamond J. B., Smith M. A., and Bandettini P. A. (2006) Separating respiratory-variation-related fluctuations from neuronal-activity-related fluctuations in fMRI. *Neuroimage*. 31, 1536-1548.

Biswal B., DeYoe A. E., and Hyde J. S. (1996) Reduction of physiological fluctuations in fMRI using digital filters. *Magn Reson Med*. 35, 107-113.

Boynton G. M., Engel S. A., Glover G. H., and Heeger D. J. (1996) Linear systems analysis of functional magnetic resonance imaging in human V1. *J Neuroscience*. 16, 4207-4221.

Burock M. A. and Dale A. M. (2000) Estimation and detection of event-related fMRI signals with temporally correlated noise: a statistically efficient and unbiased approach. *Human Brain Mapping*. 11, 249-260.

Cox R. W. (1996) AFNI-software for analysis and visualization of functional magnetic resonance neuroimages. *Comput Biomed Res*. 29, 162-173.

Dagli M. S., Ingeholm J. E., and Haxby J. V. (1999) Localization of cardiac-induced signal change in fMRI. *Neuroimage*. 9, 407-415.

Glover G. H., Li T. Q., and Ress D. (2000) Image-based method for retrospective correction of physiological motion effects in fMRI: RETROICOR. *Magn Reson Med*. 44, 162-167.

Glover G. H., Li T.-Q., and Ress D. (2000) Image-based method for retrospective correction of physiological motion effects in fMRI: RETROICOR. *Magn Res Med*. 44, 162-167.

Hoge R. D., Atkinson J., Gill B., Crelier G. R., Marrett S., and Pike G. B. (1999) Investigation of BOLD signal dependence on cerebral blood flow and oxygen consumption: the deoxyhemoglobin dilution model. *Magn Reson Med*. 42, 849-863.

Hu X., Le T. H., Parrish T., and Erhard P. (1995) Retrospective estimation and correction of physiological fluctuation in functional MRI. *Magn Reson Med*. 34, 201-212.

Jackson D. A. (1993) Stopping Rules in Principal Components Analysis: A Comparison of Heuristical and Statistical Approaches. *Ecology*. 74, 2204-2214.

Josephs O., Howseman A., Friston K. J., and Turner R. (2001) Physiological Noise Modelling for multi-slice EPI fMRI using SPM. *Proc Intl Soc Mag Reson Med*, 1682.

Kruger G. and Glover G. H. (2001) Physiological noise in oxygenation-sensitive magnetic resonance imaging. *Magn Reson Med*. 46, 631-637.

Liu C. S., Miki A., Hulvershorn J., Bloy L., Gualtieri E. E., Liu G. T., Leigh J. S., Haselgrove J. C., and Elliott M. A. (2006) Spatial and temporal characteristics of physiological noise in fMRI at 3T. *Acad Radiol*. 13, 313-323.

Lund T. E. and Hanson L. G. (2001) Physiological Noise Reduction in fMRI Using Vessel Time-Series as Covariates in a General Linear Model. *Proc Intl Soc Mag Reson Med*. 9, 22.

Lund T. E., Madsen K. H., Sidaros K., Luo W. L., and Nichols T. E. (2006) Non-white noise in fMRI: does modelling have an impact? *Neuroimage*. 29, 54-66.

McKeown M. J., Hansen L. K., and Sejnowsk T. J. (2003) Independent component analysis of functional MRI: what is signal and what is noise? *Curr Opin Neurobiol*. 13, 620-629.

Mumford J. A., Hernandez-Garcia L., Lee G. R., and Nichols T. E. (2006) Estimation efficiency and statistical power in arterial spin labeling fMRI. *Neuroimage*. 33, 103-114.

Petersen N., Jensen J., Burchardt J., and Stodkilde-Jorgensen H. (1998) State space models for physiological noise in fMRI time series. *Neuroimage*. 7, 727-741.

Pfeuffer J., Van de Moortele P. F., Ugurbil K., Hu X., and Glover G. H. (2002) Correction of physiologically induced global off-resonance effects in dynamic echo-planar and spiral functional imaging. *Magn Reson Med*. 47, 344-353.

Restom K., Behzadi Y., and Liu T. T. (2006) Physiological noise reduction for arterial spin labeling functional MRI. *Neuroimage*. 31, 1104-1115.

Smith S. M., Jenkinson M., Woolrich M. W., Beckmann C. F., Behrens T. E., Johansen-Berg H., Bannister P. R., De Luca M., Drobnjak I., Flitney D. E., Niazy R. K., Saunders J., Vickers J., Zhang Y., De Stefano N., Brady J. M., and Matthews P. M. (2004) Advances in functional and structural MR image analysis and implementation as FSL. *Neuroimage*. 23 Suppl 1, S208-219.

Stoica P. and Moses R. (1997) *Introduction to Spectral Analysis*. Prentice-Hall, Upper Saddle River, NJ.

Thomas C. G., Harshman R. A., and Menon R. S. (2002) Noise reduction in BOLD-based fMRI using component analysis. *Neuroimage*. 17, 1521-1537.

Wong E. C., Buxton R. B., and Frank L. R. (1998) Quantitative imaging of perfusion using a single subtraction (QUIPSS and QUIPSS II). *Magn Reson Med*. 39, 702-708.

Woolrich M. W., Ripley B. D., Brady M., and Smith S. M. (2001) Temporal autocorrelation in univariate linear modeling of FMRI data. *Neuroimage*. 14, 1370-1386.

Chapter 5

Conclusions

fMRI has grown tremendously over the past decade as a valuable tool to non-invasively study the working human brain. Although a powerful tool, the fMRI signal is an indirect measure of neural activity and is the result of the complex coupling of evoked neural responses and regional hemodynamics. Non-neuronal sources of variability have limited the application and quantitative interpretation of the fMRI signal. In particular, the baseline vascular state and physiological noise have remained important factors confounding the fMRI signal.

5.1 An Arteriolar Compliance Model of the CBF Response to Neural Stimulus

5.1.1 Contributions

In chapter 2, a novel arteriolar compliance model was presented and shown to describe to first order the observed complex dependence of BOLD dynamics on the baseline vascular state. Published in (Behzadi et al., 2005), the arteriolar compliance model represents the first concerted effort to model this important effect.

5.1.2 Future Directions

Although the arteriolar compliance model has been shown to predict to first order the observed changes in the temporal dynamics of the CBF and BOLD responses, it is unable to simultaneously fit the post-stimulus undershoot of the BOLD response under all baseline conditions(Behzadi et al., 2005). The post-stimulus undershoot is thought to originate from a mismatch between CBF and CBV that is a result of the viscoelastic properties of the venous compartment(Buxton et al., 1998). As CBF returns to its baseline value with cessation of evoked neural activity the CBV remains elevated, returning to baseline with a viscoelastic time constant for deflation, τ_{v-} . Then if the oxygen extraction fraction returns to baseline with CBF, and the CBV remains elevated, the total dHb will be higher than baseline, reducing the BOLD signal. However other explanations of the post-stimulus undershoot are possible. $CMRO_2$ may remain elevated with a return to baseline of CBF and CBV or CBF may drop below baseline after the stimulus ends, possibly due to neuronal inhibition during the post-stimulus period(Buxton et al., 1998).

In Behzadi et al., we showed that the τ_{v-} appears to decrease with resting CBF(Behzadi et al., 2005). A smaller τ_{v-} at low baseline CBF suggests a relatively greater elastic response. This may reflect the non-linear nature of the veins in which they are fairly compliant and stiffen exponentially as the CBF and radius increase(Fung, 1984). Although this result supports the notion that the post-stimulus undershoot is a reflection of a mismatch between CBF and CBV, more investigation is required to fully elucidate the role of $CMRO_2$ and neural activity during this period. Extensions to the arteriolar compliance model are needed to explain the dynamics of the post-stimulus undershoot.

In order to describe discrepancies between spin echo and gradient echo based BOLD measurements, Uludag et al. recently presented the compartmental balloon model(Uludag et al., 2005). In his formulation the BOLD signal model was adapted to describe the various contribution of the arteriole, capillary, and venules vascular compartments to the overall BOLD signal. This extension of the balloon model represents an important step in describing differences in the observed BOLD dynamics as a result of different pulse sequence sensitivities. Future work will involve integration of the arteriolar compliance model and the compartmental balloon model.

5.2 Caffeine Reduces the Initial Dip in the Visual BOLD Response at 3T

5.2.1 Contributions

In chapter 3, we show that caffeine, through modulation of the baseline vascular state, significantly affects the detection of the initial dip in the visual BOLD response. As presented in (Behzadi et al., 2006), this study provides insight into the physiological basis of the initial dip and on the on-going debate in fMRI regarding the presence of the initial dip that has spanned several years.

5.2.2 Future Directions

Additional extensions to the BOLD model are needed to help explain the experimental observation that the initial dip is reduced with vasoconstriction. If strict coupling of CBF and $CMRO_2$ is preserved, as presented in the formulation of the arteriolar compliance model in chapter 2, we would expect no initial decrease in dHb. For an initial dip of the BOLD signal to occur, there must be a transient increase in dHb resulting from a mismatch of CBF and $CMRO_2$ (Behzadi et al., 2006). This may occur if there is a time delay between an immediate change in $CMRO_2$ and the consequent CBF changes. It is currently unclear what the dependence of the $CMRO_2$ dynamics are on the baseline vascular state. A more formal metabolic model for $CMRO_2$ dynamics as a function of baseline is needed and will be the focus of future work.

5.3 Component Based Noise Correction

5.3.1 Contributions

In chapter 4, a component based method for the removal of physiological noise was developed and shown to significantly reduce the temporal variance and increase the sensitivity of BOLD and perfusion-based fMRI. The proposed algorithm was shown to remove cardiac and respiratory induced noise without the need for external monitoring of physiological processes .

5.3.2 Future Directions

We presented a component based noise correction scheme in chapter 4 that utilized principal components from noise regions-of-interest to model and remove the effect of physiological noise from gray matter. Future extensions to this technique will investigate the use of independent component analysis (ICA) to identify individual physiological noise elements. Whereas PCA involves the estimation of uncorrelated (orthogonal) components, ICA takes a more general approach and aims at decomposing the data into statistically independent and non-Gaussian components (McKeown et al., 1998). ICA has been used extensively in fMRI to identify underlying patterns of activation (Beckmann et al., 2004; McKeown et al., 2003; McKeown et al., 1998). However, its ability to robustly identify the physiological noise subspace has yet to be studied.

Recently additional sources of physiological noise have been identified involving variations in respiratory volume and cardiac rate variation (Birn et al., 2006) (Katura et al., 2006). Additional extensions to the CompCor algorithm presented in chapter 4 will be to characterize its ability to remove noise components related to variation of the respiratory and cardiac rates occurring at 0.03 Hz and 0.1 Hz, respectively.

5.4 References

Beckmann C. F. and Smith S. M. (2004) Probabilistic independent component analysis for functional magnetic resonance imaging. *IEEE Trans Med Imaging*. 23, 137-152.

Behzadi Y. and Liu T. T. (2005) An arteriolar compliance model of the cerebral blood flow response to neural stimulus. *Neuroimage*. 25, 1100-1111.

Behzadi Y. and Liu T. T. (2005) The Viscoelastic Properties of the Venous Compartment are Dependent on Baseline CBF. In: *ISMRM 13th Scientific Meeting*), pp. 279, Miami.

Behzadi Y. and Liu T. T. (2006) Caffeine reduces the initial dip in the visual BOLD response at 3 T. *Neuroimage*.

Birn R. M., Diamond J. B., Smith M. A., and Bandettini P. A. (2006) Separating respiratory-variation-related fluctuations from neuronal-activity-related fluctuations in fMRI. *Neuroimage*. 31, 1536-1548.

Buxton R. B., Miller K., Frank L. R., and Wong E. C. (1998) BOLD signal dynamics: the balloon model with viscoelastic effects. In: *Sixth Meeting, International Society for Magnetic Resonance in Medicine*), pp. 1401, Sydney, Australia.

Buxton R. B., Wong E. C., and Frank L. R. (1998) The post-stimulus undershoot of the functional MRI signal.

Fung Y. (1984) *Biomechanics: Circulation*, 2 edn. Springer-Verlag, New York.

Katura T., Tanaka N., Obata A., Sato H., and Maki A. (2006) Quantitative evaluation of interrelations between spontaneous low-frequency oscillations in cerebral hemodynamics and systemic cardiovascular dynamics. *Neuroimage*. 31, 1592-1600.

McKeown M. J., Hansen L. K., and Sejnowsk T. J. (2003) Independent component analysis of functional MRI: what is signal and what is noise? *Curr Opin Neurobiol*. 13, 620-629.

McKeown M. J. and Sejnowski T. J. (1998) Independent component analysis of fMRI data: examining the assumptions. *Hum Brain Mapp*. 6, 368-372.

Uludag K. and Buxton R. (2005) The Compartmental Balloon Model. In: *12th ISMRM.*), Miami.

Appendix A1

Magnetic Resonance Imaging Physics Primer

A1.1 Introduction

In 1936, Pauling and Coryell demonstrated that deoxyhemoglobin (dHb) disrupts a magnetic field, whereas oxygenated Hb does not (Pauling et al., 1936). This origin of this effect is that Hb is diamagnetic when oxygenated and paramagnetic when deoxygenated. As a paramagnetic agent, dHb alters the local magnetic susceptibility, creating magnetic field distortions within and around blood vessels, and this inhomogenous field produces alterations in the local magnetic resonance (MR) signal. This phenomenon was not leveraged until Ogawa et al, in 1990, showed that the MR image of a mouse brain was modulated by the level of inspired 0_2 (Ogawa et al., 1990). They noted that the presence of dHb, a function of inspired 0_2, reduced the local MR signal. They identified the effect as the blood oxygenation level dependent (BOLD) signal and it was soon after that Kwong et al. first demonstrated a mapping of activation in the human brain using gradient echo MR imaging during visual stimulation (Kwong et al., 1992).

In order to gain a qualitative understanding of the BOLD signal, we can use the experimental observation detailed in the Introduction that with neural activity CBF increases more than $CMRO_2$, leading to decreases in dHb and an increase in the local BOLD signal. This basic observation has served as the foundation of fMRI and helped revolutionize neuroimaging. In order to more quantitatively understand the BOLD signal it is first important to review basic

MR physics in the context of the BOLD signal. Interpretation of BOLD measurements is greatly increased with the application of arterial spin labeling (ASL) techniques used to image the perfusion response to neural activity. Taken together, the ASL and BOLD signals provide an added insight into the dynamics of the hemodynamics response to neural activity.

A1.2 The NMR signal

A basic review of MR physics is provided to help in the understanding of the BOLD response used in fMRI. When an object is placed in a uniform magnetic field, denoted by B_0, the nuclear magnetic dipole tend to align with the field. If the direction of magnetization is altered from its equilibrium point, with application of an external force, the magnetization will realign with a given time constant T_1.

Another important physical phenomena central to MRI is that certain nuclei (notably hydrogen) possess an intrinsic magnetic moment and rotate at a frequency proportional to the magnetic field. This phenomena, known as the nuclear magnetic resonance (NMR), was discovered in 1946 by two groups: Purcell, Torry, and Pound and Bloch, Hansen, and Packard. The fundamental equation of magnetic resonance is:

$$\boldsymbol{v}_0 = \gamma \boldsymbol{B}_0 \qquad [1]$$

In which the resonant frequency (i.e. Larmor frequency) v_0, is a function of the molecule specific gyromagnetic ratio, γ , and the magnetic field, B_0. In a basic NMR experiment, a sample is placed in a uniform magnetic field and an oscillating RF pulse , generated by an oscillating current in a nearby coil, is applied. At its resonant frequency, a nucleus can absorb electromagnetic energy from the RF pulse which can effect the direction of its magnetization. Therefore if the RF pulse is applied at the resonant frequency of the sample and in a field orthogonal to B_0, the magnetization of the sample will "tip" toward a direction orthogonal to B_0, or equivalently into the transverse plane. In time, the magnetization recovers back to align with

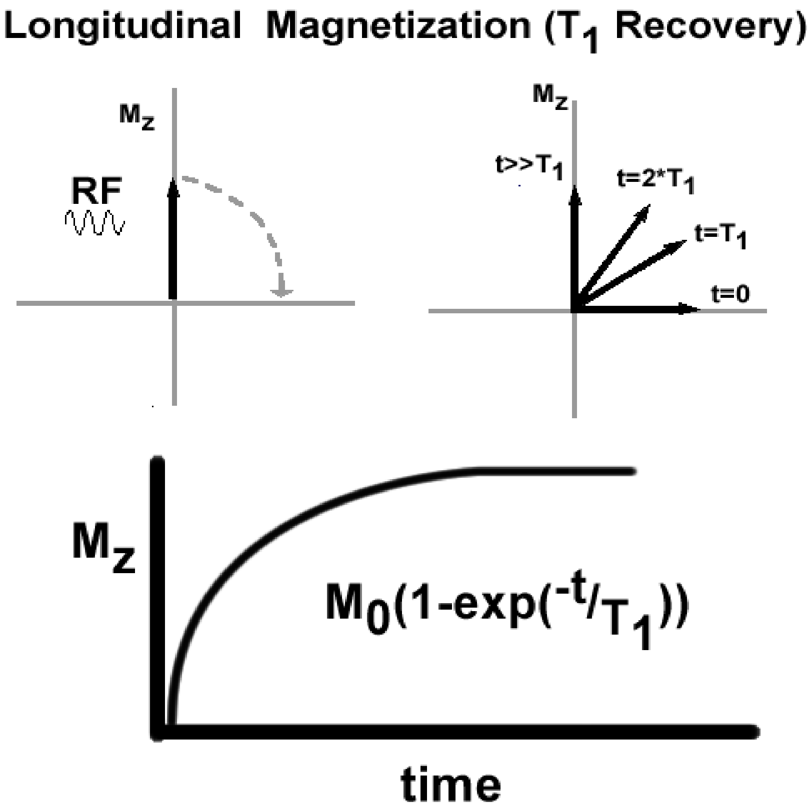

Figure A1.1. Longitudinal magnetization with recovery rate of T_1. After application of a RF pulse, the longitudinal magnetization is “tipped” onto the transverse plane. The magnetization then recovers to align with B_0.

the direction of B_0 with a time constant T_1. During the recovery period, the molecules are rotating about the axis of the direction of magnetization. This rotating magnetic field creates a transient oscillating current, known as the free induction decay (FID), in the coil. The recovery of the longitudinal magnetization following the 90 degree RF pulse, as governed by exponential T_1 recovery, is depicted figure A1.1. The magnitude of the magnetization in the direction of B_0 is referred to longitudinal magnetization whereas the magnetization orthogonal to B_0 is known as transverse magnetization or precessing magnetization. The net precessing magnetization decays away with a time constant, T_2. The reason for this is that the individual dipoles that contribute to the overall transverse magnetization are not all precessing at the same rate. For instance, a hydrogen molecule in a water sample will experience randomly varying magnetic fields due to thermal motion of other hydrogen atoms. In some cases the interaction will speed up the precession and in other cases slow down the precession causing phase shifts between individual dipoles. Since the net magnetization is dependent on the coherence of the precession of individual dipoles the signal will be degraded. The process of phase dispersion and T_2 decay is presented in figure A1.2.

To summarize, the NMR signal is a result of applying a RF pulse to tip the sample magnetization to an angle, known as the flip angle, to the main magnetic field B_0. As the individual molecules precess and realign with the main field, an oscillating current is generated in a nearby coil. The resultant signal is a function in time of the longitudinal relation time constant T_1 and the transverse decay constant T_2, which are both a function of B_0. In a more complex sample, the resultant signal is a function of time determined by multiple T_1's and T_2's.

In practice, the transverse magnetization decays faster than the expected T_2. This increased decay is due to magnetic field inhomogeneity and is referred to T_{2*}. In order to describe the NMR signal, Block proposed a set of three coupled differential equations. The equations are written separately for each direction of the magnetization, M_x, M_y, and M_z.

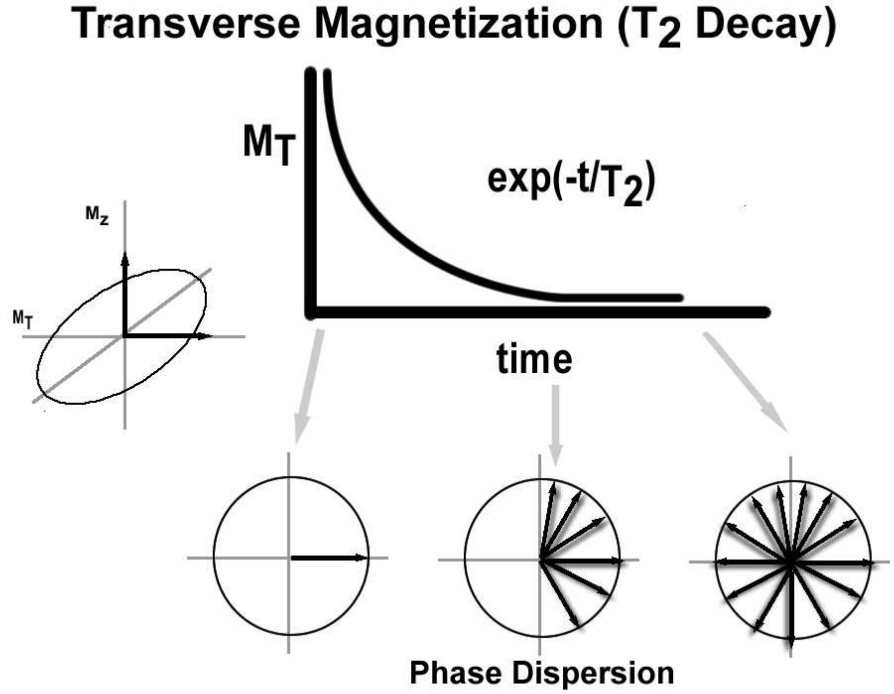

Figure A1.2. The decay of transverse magnetization with the decay rate of T_2. After the 90^0 RF pulse is turned off and the magnetization is in the transverse plane, all spins are in phase. Dephasing occurs in time due to spin-spin interactions and magnetic field inhomogeneity.

$$\frac{dM_x}{dt} = \gamma B_0 M_y - \frac{M_x}{T_2}$$
$$\frac{dM_y}{dt} = -\gamma B_0 M_x - \frac{M_y}{T_2} \qquad [2]$$
$$\frac{dM_z}{dt} = -\frac{M_z - M_0}{T_1}$$

In this formulation, M_z is the direction of the main magnetic field B_0, and M_x and M_y are the directions orthogonal to B_0.

A1.3 Magnetic Resonance Imaging

In MRI the hydrogen molecule is used as a basis for generating the NMR signal. Contrast is generated by taking advantage of the fact that the T_1 and T_2 of various tissues are different. For instance, at a B_0 of 1.5T, the T_1's for gray matter, white matter, and CSF are 900ms, 700ms, and 4000ms, respectively(Buxton, 2002). The T_2's are considerably shorter at 70 ms, 90 ms, and 400 ms, for gray matter, white matter, and CSF, respectively(Buxton, 2002). Due to the difference in the T_1 and T_2's, contrast between tissue types can be generated by adjusting the time in which one records the resultant NMR signal. However, the acquired signal has no information about the location of the source of the signal. Some form of spatial encoding must be done to localize the acquired signal.

Lauterbaur (1973) and Mansfield (1977) applied a magnetic gradient across a sample in order to spatially localize the NMR signal (Lauterbur, 1973; Mansfield, 1977). Since the resonant frequency is dependent on the magnetic field, the molecules in a sample under a gradient would precess at different rates depending on their location. In other words, a gradient field produces a linear variation of the precession rate with position. This effect can be understood by dividing a sample in the direction of the gradient into three distinct regions denoted by their position relative to the center as x_{-1}, x_0, x_1. Since the gradient is linear with respect to location, the local field in each subsection of the sample can be thought as B_0-ΔB, as

B_0 ,and, as $B_0+\Delta B$. At time equal to zero, the net phase of the magnetization in each section is equivalent. However in time, the phase of x_{-1} will lag with respect to x_0 while x_1 will be ahead due to their different respective magnetic fields. The application of a gradient is modulating the phase of the localized signal. This modulation is equivalent to multiplying the local signal with a cosine with a given frequency, which is a function of the length of time the local phase has been affected by the gradient. The basis of imaging using the NMR signal is the fact that the phase of the local signal can be manipulated by the application of a magnetic gradient such that the net signal is the spatial Fourier transform of the distribution of transverse magnetization. If encoding is performed in multiple directions the resultant NMR signal can be localized in space.

This is more formerly characterized by considering a signal, *S*(t), within a sample volume *V*:

$$\boldsymbol{S}(\boldsymbol{t}) = \int_V \boldsymbol{p}(\boldsymbol{r}) \boldsymbol{e}^{-i\phi(r,t)} \boldsymbol{d}^3\boldsymbol{r} \qquad [3]$$

where *p(r)* is the position dependent density of nuclear spins and $\phi(\boldsymbol{r},\boldsymbol{t})$ represents their phase. The phase of the signal increases at a rate proportional to its angular velocity, which is turn is a function of the local magnetic field. With application of a magnetic field gradient, described by $\boldsymbol{B}(\boldsymbol{r},\boldsymbol{t}) = \boldsymbol{B}_0 + \boldsymbol{G}(\boldsymbol{t}) \cdot \boldsymbol{r}$, the relative phase between spins can be expressed by:

$$\phi(\boldsymbol{r},\boldsymbol{t}) = \left[\gamma \int_0^{\boldsymbol{t}} \boldsymbol{G}(\boldsymbol{t}')\boldsymbol{dt}' \right] \cdot \boldsymbol{r} = \boldsymbol{k}(\boldsymbol{t}) \cdot \boldsymbol{r} \qquad [4]$$

Combining equations 3 and 4, yields

$$\boldsymbol{S}(\boldsymbol{k}) = \int_V \boldsymbol{p}(\boldsymbol{r}) \boldsymbol{e}^{-ik(t)\cdot r} \boldsymbol{d}^3\boldsymbol{r} \qquad [5]$$

which is the Fourier transform equation, stating that *S*(k) is equivalent the Fourier transform of the spin density *p(r).* The net area under the curve of the gradient then determines the relative position in k-space. A basic MRI image is formed by applying a RF-pulse to tip the

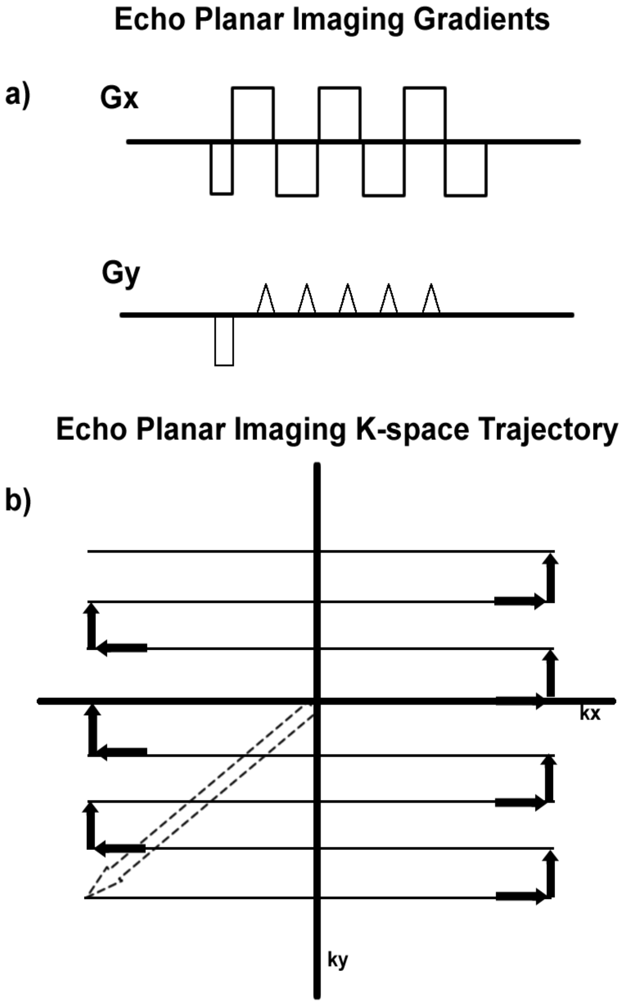

Echo Planar Imaging Gradients

Echo Planar Imaging K-space Trajectory

Figure A1.3. (a) Schematic echo planar G_x and G_y gradients.
(b)Corresponding trajectory through k-space.

magnetization to a given flip angle, α, one then waits a given echo time (TE) depending on desired contrast, and finally applies gradients and then samples the resultant k-space representation of the image. The raw data is then the spatially encoded spin density, at an imaging time with contrast determined by the T_1's, T_2's. Reconstruction of the image is accomplished by taking the inverse Fourier transform of the image with knowledge of the k-space trajectory. The process of applying an RF and imaging is repeated at a given time of repetition, TR.

A basic echo planar imaging (EPI) scheme is presented in figure A1.3. EPI is a time efficient way to traverse k-space. After slice selective excitation, a negative G_x and G_y gradient is applied to acquire the first sample in k-space. Recall that the net area under the curve of the gradients represents the relative encoding of the image and position in k-space. Next a positive G_x gradient is used to march across k_x in which discrete samples are taken from the resultant NMR signal. A positive G_y gradient is used to move positively in k_y and the G_x gradient is reversed to traverse back across k_x. This sequence is repeated until the required k-space samples are captured. The primary focus of MRI has been in the manipulation of this basic sequence of events to optimize different contrast of interest in the context of the trade-off between spatial and temporal resolution.

A1.4 Applications to Functional Imaging

Especially relevant to the discussion of the BOLD signal used extensively in fMRI is the concept of magnetic susceptibility. Magnetic susceptibility refers to degree to which a material becomes magnetized when placed in a magnetic field. In addition to the forces discussed earlier, another effect of placing a sample in a magnetic field is that the local magnetic field is distorted by the interaction of internal dipole moments in the material with the field. The effective magnetic field around an object is then distorted by the geometry and susceptibility of that object. These distortions alter the local magnetic field and thus the resonant frequency of the hydrogen molecule. Difference in susceptibility between different types of materials in the brain can cause signal reductions. For instance, sinus cavities filled with air can cause field distortions that negatively affect the surrounding MR signal. These unwanted distortions are further exaggerated with certain types of imaging sequences. Ironically, although susceptibility effects have been the cause of much grief in MRI they form the basis of BOLD based fMRI. The BOLD effect is the result of the differences in magnetic susceptibility of oxygenated and deoxygenated blood in a vessel. Figure A1.4 is a schematic of a magnetized cylinder in which the presence of deoxyhemoglobin within the vessel causes magnetic field distortions in the surrounding space. This then increases the degree of phase dispersion, decreasing the T_{2*}, and reducing the resulting MR signal.

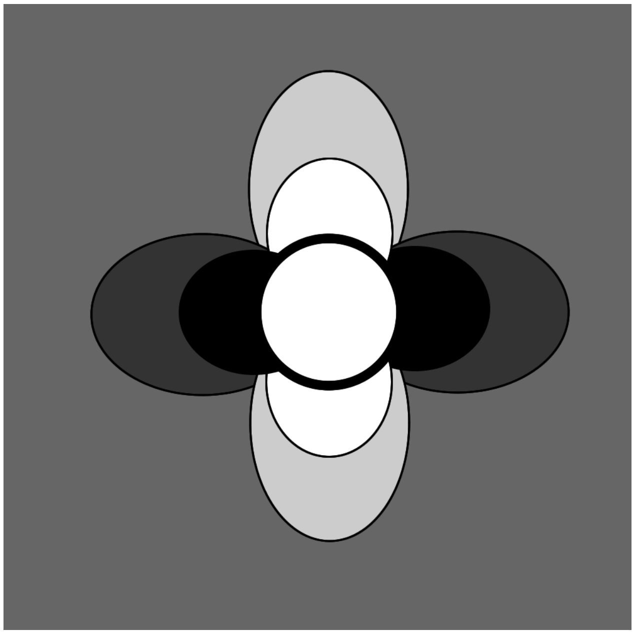

Figure A1.4. The magnetized cylinder is a model for a blood vessel containing deoxyhemoglobin, showing a dipole distortion in the space around the vessel.

A1.5 References

Buxton R. B. (2002) *Introduction to Functional Magnetic Resonance Imaging*. Cambridge University Press, Cambridge.

Kwong K. K., Belliveau J. W., Stern C. E., Chesler D. A., Goldberg I. E., Poncelet B. P., Kennedy D. N., Weisskoff R. M., Cohen M. S., Turner R., Cheng H.-M., Brady T. J., and Rosen B. R. (1992) Functional MR imaging of primary visual and motor cortex. *JMRI*. 2(P) [Abstr.], 76.

Lauterbur P. C. (1973) Image formation by induced local interactions: examples employing nuclear magnetic resonance. *Nature*. 242, 190-191.

Mansfield P. (1977) Multi-planar image formation using NMR spin echoes. *J Phys*. C10, L55-L58.

Ogawa S. and Lee T.-M. (1990) Magnetic resonance imaging of blood vessels at high fields: in vivo and in vitro measurements and image simulation. *Magn Reson Med*. 16, 9-18.

Pauling L. and Coryell C. D. (1936) The magnetic properties and structure of hemoglobin, oxyhemoglobin, and carbonmonoxyhemoglobin. *Proc Natl Acad Sci USA*. 22, 210-216.

Appendix A2

fMRI: Phyiological Basis

A2.1 Neural System

Neurons are the functional subunits of the brain and their coordinated function results in the seemingly limitless information processing capability of the human brain. A stark, simple view of population neuronal processing was put forward in 1943 by McCullough and Pitts in which all synaptic inputs converged into a single point neuron (McCulloch et al., 1943). In this model individual neurons would respond to specific environmental or internal inputs and then broadcast their response, via action potentials, to their postsynaptic targets. Summation of incoming spikes from multiple neurons would occur at each target neuron and if a given threshold was exceeded, the target neuron would generate a spike in response. McCullough and Pitts proved that a sufficiently large number of these simple logic devices, wired appropriately, would be capable of universal computation (McCulloch et al., 1943). This simple model provided insight into the importance of the coordinated function and the interconnectivity of neurons as a basis for their ability to process information. The brain then utilizes this information according to two fundamental principles of functional specialization and integration. Specialization refers to the localization of specific types of processing to anatomically distinct areas of the brain. Integration then refers to the interconnectivity of these specialized regions.

One of the most well studied areas in the human brain is the visual system located in the occipital lobe. A brief exploration of the visual system will help highlight the role of specialization and integration in the processing of information. Once visual information is captured in the eye it is transmitted via the optic nerve to the lateral geniculate nucleus (LGN) in the thalamus. The V1 region of the visual cortex then receives input directly from LGN. Specialization is well illustrated in V1, where the visual scene is spatially encoded in a highly conserved and specific manner. For example, the upper bank of the calcarine sulcus responds to the lower half of the visual field whereas the lower bank responds to the upper half of the visual field (Belliveau et al., 1991).

V1 is responsible for the neuronal processing of spatial frequency, orientation, motion, direction, speed, and other visual features . Strong feedforward connections exist between V1 and V2 and serve to carry and integrate information from V1 for further processing. V2 is tuned for processing of complex patterns and has connections to V3, V4, and V5 and send feedback connections back to V1. In addition to environmental inputs from the eyes, the visual system is modulated by internal sources such as attention pathways. The interconnectivity of the visual system exemplifies the role of information integration from specialized regions in overall information processing.

In fMRI applications, the localized neural activity can be simply modeled as a inhibitory feedback system, in which the neural response U(t) is treated as the sum of excitatory E(t) and inhibitory inputs I(t). The inhibitory response is driven by the neural response and can be represented by:

$$\boldsymbol{U(t)} = \boldsymbol{E(t)} - \boldsymbol{I(t)} \qquad [1]$$

$$\frac{\boldsymbol{dI}}{\boldsymbol{dt}} = \frac{\kappa \boldsymbol{U(t)} - \boldsymbol{I(t)}}{\tau_1} \qquad [2]$$

where κ and τ_1 are a gain factor and time constant, respectively(Buxton et al., 2001).This simple linear model allows for the incorporation of neural adaptation and refractory effects demonstrated experimentally. An nonlinear component may also be introduced to more accuratley capture observed dynamics. By introducing a baseline level of neural activity and requiring the neural activity to be always positive , one can prevent post-stimulus undershoots that may occurr in the linear model presented above. This behavior matches a pattern originally proposed to describe BOLD signal nonlinearities observed in the visual cortex (Boynton et al., 1996). The necessity of a refractory period has also been proposed to model the diminsihing response to a pair of closely spaced stimuli (Buxton et al., 2004).

Neural activity leads to increases in tissue metabolism and the firing of neuronal action potentials result in (1) the release of neurotransmitter into the synaptic cleft and (2) changes in ionic gradients(Buxton, 2002). Consequently the main cost of maintaining homeostasis involves the restoration of ionic gradients and repacking of neurotransmitter molecules. Weighing approximately 3 lbs, the brain uses nearly 20% of the body's energy and its demands are met almost exclusively by glucose oxidation, in which 90% of resting glucose consumption is oxidative (Buxton, 2002). Since the energy yield of glucose oxidation is much more than glycolysis nearly all the ATP production in the resting state is via glucose oxidation(Buxton, 2002).

Figure A2.1 is a representation of the cellular events associated with the cycling of glutamate, a neurotransmitter. It is important to note that ATP is used to extrude Na^+ taken in along with glutamate from the synapse, convert glutamate to glutamine, and supply energy to the Na^+/K^+ pump used to restore ionic potentials. ATP is primarily supplied by aerobic glycolysis in astrocytes and the excess lactate is transported to adjacent neurons to be further metabolized (Raichle et al., 2006).

PET studies by Fox et al. reported that the $CMRO_2$ and for cerebral metabolic rate of glucose (CMRGlu) is in a ~4:1 molar ratio further supporting the dominant role of oxidative mechanisms during rest(Raichle et al., 2006). With functional activation, $CMRO_2$ is increased by only ~15% whereas CMRGlu and CBF are increased ~50% (Raichle et al., 2006).

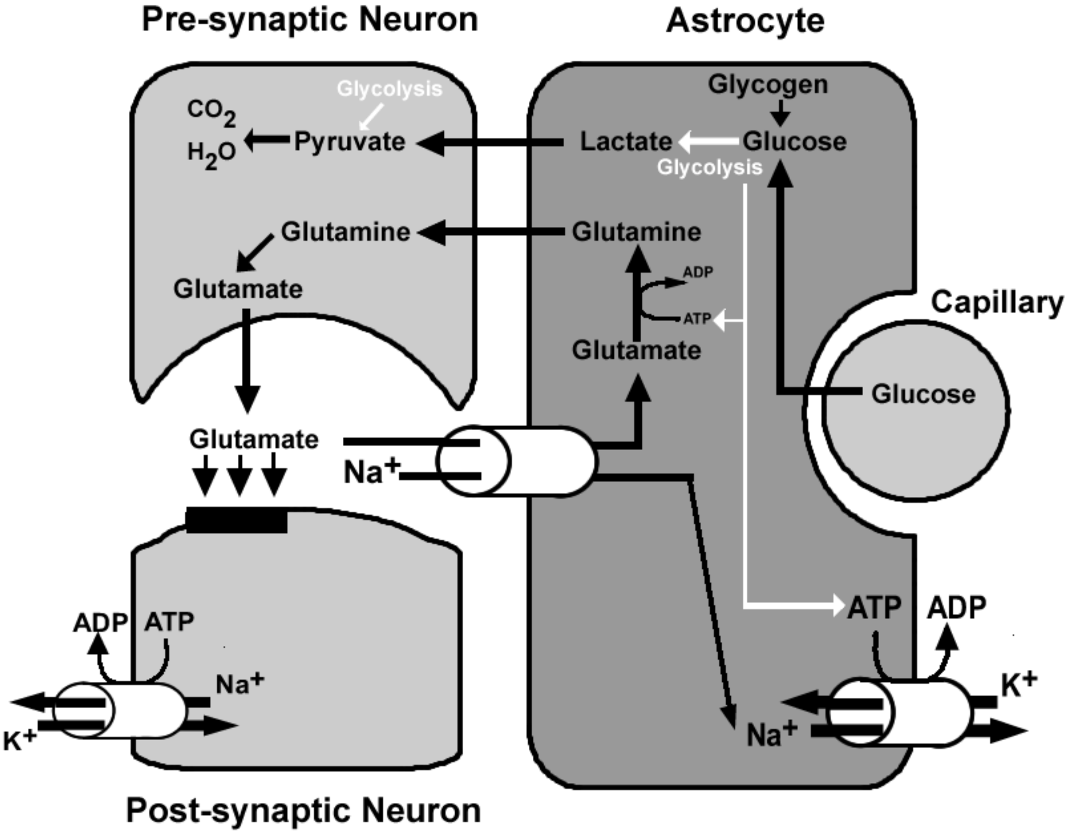

Figure A2.1. A representation of the metabolic events associated with the release of glutamate. It is important to note the role of the astrocyte in supplying ATP for the conversion of glutamate to glutamine, $Na^+\backslash K^+$ pump, and the reuptake of glutamate from the synapse. Based on figure from (Raichle et al., 2006).

A2.2 Hemodynamic System

Increases in CBF during activation serve to deliver needed nutrients (e.g. glucose and oxygen) and carry away byproducts of metabolism (e.g. lactate, heat). The ratio between relative changes in CBF with respect changes in $CMRO_2$ with neural activity is used as a parameter describing neurovascular coupling (n) and is denoted (Buxton et al., 2004):

$$\boldsymbol{n} = \frac{\Delta \boldsymbol{CBF} / \boldsymbol{CBF}_0}{\Delta \boldsymbol{CMRO}_2 / \boldsymbol{CMRO}_{2,0}} = \frac{\boldsymbol{f} - 1}{\boldsymbol{m} - 1} \qquad [3]$$

Where f and m are CBF and $CMRO_2$ normalized to their respective baseline values. This fundamental ratio forms the basis of fMRI. The basic picture of brain activation is simple: stimuli evoke increased activity in neuronal populations, ATP consumption increases, oxidative metabolism increases to restore ATP, and CBF increases to supply nutrients and carry away metabolic byproducts. However, the mechanisms involved are complex. A recent review by Iadecola summarizes the role of activity-induced signaling mechanisms that not only involve neurons but also astrocytes and vascular cells. Dilation of arterioles resulting from increased neural activity is dependent on Ca^{2+} oscillations in astrocytes (Iadecola, 2004). In addition, upstream vasodilation may result from intramural signaling in endothelial and smooth muscle cells. Despite the complete understanding of the exact mechanisms involved, it is known that various vasoactive agents are released following increases in neural activity that modulate the local cerebral blood flow through their effect on smooth muscle cells(Iadecola, 2004). Several models have been introduced to describe the CBF response to neural stimulus, most relevant to fMRI is a model by Friston et al, who presented a simple linear second-order system to describe the regulation of CBF following neural activity (Friston et al., 2000).

Hemodynamic changes involve the coupling of changes in CBF with cerebral blood volume and $CMRO_2$. As the smooth muscle relaxes in response to the release of vasoactive agents, the resistance in the vascular tree decreases. As the resistance decreases, the pressure drop across the vessels also decreases, raising the pressure in both the capillaries and veins. The vessels expand, increasing the cerebral blood volume. The steady-state relationship between CBF and CBV is described by (Grubb et al., 1974):

$$\boldsymbol{v} = \boldsymbol{f}^{\alpha} \qquad [4]$$

where v and f are CBV and CBF normalized by their initial values, respectively. Grubb experimentally found that α equal to 0.38 which is in contrast to a laminar flow assumption in which α should equal 0.5 (Grubb et al., 1974). An analytical solution for Grubb's empirical relationship can be derived by noting that the total blood volume is the sum of arteriole (V_a), capillary(V_c), and venous blood volumes(V_v) as denoted.

$$\boldsymbol{V_T} = \boldsymbol{V_a} + \boldsymbol{V_c} + \boldsymbol{V_v} \qquad [5]$$

The relationship between volume and flow in the arterial and venous compartments is governed by a power law relationship with the assumption of laminar flow, $\alpha_L=0.5$. In contrast, during increases in flow, the capillary compartment experiences negligible increases in volume(Fung, 1984). Substituting expressions for the blood volume in terms of flow using the following relationships:

$$\boldsymbol{V_a} = \boldsymbol{V_{a,0}}(\boldsymbol{F}/\boldsymbol{F_0})^{\alpha_L} \qquad \boldsymbol{V_v} = \boldsymbol{V_{v,0}}(\boldsymbol{F}/\boldsymbol{F_0})^{\alpha_L} \qquad \boldsymbol{V_T} = \boldsymbol{V_{T,0}}(\boldsymbol{F}/\boldsymbol{F_0})^{\alpha_T} \qquad \boldsymbol{V_c} = \boldsymbol{V_{c,0}} \qquad [6]$$

and solving for α_T yields the analytical expression for Grubb's constant:

$$\alpha_{\boldsymbol{T}} = \log_{\boldsymbol{f}}(\boldsymbol{f}^{\alpha_L}(\boldsymbol{V_{a,0}}/\boldsymbol{V_{T,0}} + \boldsymbol{V_{v,0}}/\boldsymbol{V_{T,0}}) + \boldsymbol{V_{c,0}}/\boldsymbol{V_{T,0}}) \qquad [7]$$

Where *f* is the normalized flow to its baseline value. Using fractional blood volumes of 0.33, 0.46, and 0.21 for the arterial, venous, and capillary compartments(Oja et al., 1999) , respectively, and a physiological change in *f* of 50% yields a α_T of 0.41. This is similar to the experimental value of 0.38 found by Grubbs.

By definition, the CMRO$_2$ is a function of the oxygen extraction fraction E, the arterial oxygen concentration C_a, and the CBF, as represented by(Buxton et al., 2004):

$$CMRO_2 = E \cdot C_a \cdot CBF \qquad [8]$$

one can also show that the steady-state deoxyhemoglobin concentration [dHb] depends on $CMRO_2$ and CBF, from basic mass conversation(Hoge et al., 1999):

$$[dHb] = \frac{1}{4}\frac{CMRO_2}{CBF} \qquad [9]$$

which can also be rewritten in terms of the normalized oxygen extraction fraction as

$$\frac{[dHb]}{[dHb]_0} = \frac{CMRO_2}{CBF} \cdot \frac{CBF_0}{CMRO_{2,0}} = \frac{E}{E_0} \qquad [10]$$

If $CMRO_2$ is held constant, the baseline [dHb] term is inversely proportional to the normalized CBF by

$$\frac{[dHb]}{[dHb]_0} = \frac{CBF_0}{CBF} \qquad [11]$$

Combining equation 3 and 10, in order to quantify dHb changes with changes in $CMRO_2$ and CBF, leads to the expression:

$$\frac{[dHb]}{[dHb]_0} = \frac{f + n - 1}{nf} \qquad [12]$$

From experimental observation n>1, typically in the range 2-3, which means that concentration of dHb would decrease with activation. The total dHb is then determined as the product of the CBV and dHb concentration. Incorporating Grubb's relationship, equation 4, with equation 12, the total amount of dHb can be quantified by:

$$\frac{dHb}{dHb_0} = \frac{f + n - 1}{n} \cdot f^{\alpha - 1} \qquad [13]$$

We are left with the following picture of the associated hemodynamics following neural activation: With activation, the CBF flow is increased much more than the $CMRO_2$, which leads to increased CBV and decreases in dHb. It was the discovery that dHb modulates the MR signal,as discussed in Appendix A1, that serves as a foundation for fMRI. The previously outlined cascade of events following evoked neural activity is illustrated in figure 1.2 of the Introductory chapter.

A2.3 BOLD Signal

In their pioneering work in 1990, Ogawa et al. found that when the mouse breathed 100% O_2, the brain was rather uniform (Ogawa et al., 1992). However, when the mouse breathed 20% O_2 many dark lines appeared and were localized to vessels. They also noted that the signal loss was greater with increased TE, suggesting that the presence of deoxygenated blood was acting on reducing the T_{2*}, and equivalently increasing the R_{2*}, of the blood (Ogawa et al., 1992). Boxerman et al. later determined that R_{2*} was related to CBV and [dHb], according to (Boxerman et al., 1995):

$$\boldsymbol{R}_2^*\Big|_{\boldsymbol{dHb}} = \boldsymbol{A} \cdot \boldsymbol{CBV} \cdot [\boldsymbol{dHb}]_{\boldsymbol{v}}^{\beta} \qquad [14]$$

where β is a constant depending on blood volume and the tissue sample, A is a proportionality constant, and $[\boldsymbol{dHb}]_{\boldsymbol{v}}$ is the dHb concentration in the venous compartment. Changes in $\boldsymbol{R}_2^*\Big|_{\boldsymbol{dHb}}$ lead to changes in signal intensity as a function of TE by the following expression:

$$\frac{\Delta \boldsymbol{BOLD}}{\boldsymbol{BOLD}_0} = \boldsymbol{e}^{-\boldsymbol{TE} \cdot \Delta \boldsymbol{R}_{2,\boldsymbol{dHb}}^*} - 1 \qquad [15]$$

which for small changes in $\boldsymbol{R}_2^*\Big|_{\boldsymbol{dHb}}$ can be linearized to

$$\frac{\Delta \boldsymbol{BOLD}}{\boldsymbol{BOLD}_0} = -\boldsymbol{TE} \cdot \Delta \boldsymbol{R}_{2,\boldsymbol{dHb}}^* \qquad [16]$$

where $\Delta \boldsymbol{R}_{2,\boldsymbol{dHb}}^* = \boldsymbol{A} \cdot (\boldsymbol{CBV}_0 \cdot [\boldsymbol{dHb}]_{\boldsymbol{v}0}^{\beta} - \boldsymbol{CBV}[\boldsymbol{dHb}]_{\boldsymbol{v}}^{\beta})$ [17], substituting the expression for $\Delta \boldsymbol{R}_2^*\Big|_{\boldsymbol{dHb}}$ into equation 16 and non-dimensionalizing yields

$\frac{\Delta BOLD}{BOLD_0} = M \cdot \left(1 - \left(\frac{CBV}{CBV_0}\right)\left(\frac{[dHb]_v}{[dHb]_{v0}}\right)^{\beta}\right)$ [18] where M represents the maximal BOLD signal and is equal to $M = TE \cdot A \cdot CBV_0 \cdot [dHb]_{v0}^{\beta}$ (Hoge et al., 1999). Hoge et al. presented a method for calibrating the BOLD signal with administration of CO_2 (Hoge et al., 1999). Since CO_2 modulates both resting CBF and BOLD without changes in $CMRO_2$ it can be used to determine the scaling factor M. Without changes in $CMRO_2$, the [dHb] is determined by eq 11, given by.

$$\frac{[dHb]}{[dHb]_0} = \frac{CBF_0}{CBF} \qquad [19]$$

Substituting the above expression into eq. 18 along with Grubb's equation relating CBV and CBF changes, eq 4, and solving for M yields the expression:

$$M = \frac{\Delta BOLD \big/ BOLD_0}{1 - \left(CBF \big/ CBF_0\right)^{\alpha - \beta}} \qquad [20]$$

With determination of M it is possible then to calculate $CMRO_2$ changes with a functional paradigm. This equation and CO_2 calibration methodology has proved very useful in interpretating steady-state fMRI experiments.

A2.4 BOLD Signal Dynamics

In the appendix section of chapter two a dynamic model of the BOLD signal was presented. Here we revisit the presented model and discuss some of its characteristics. Recall

that the flow out of the venous compartment is governed Grubb's relationship with viscoelastic effects as defined by

$$f_{out}(t) = v^{1/\alpha} + \tau_v \frac{dv}{dt} \qquad [21]$$

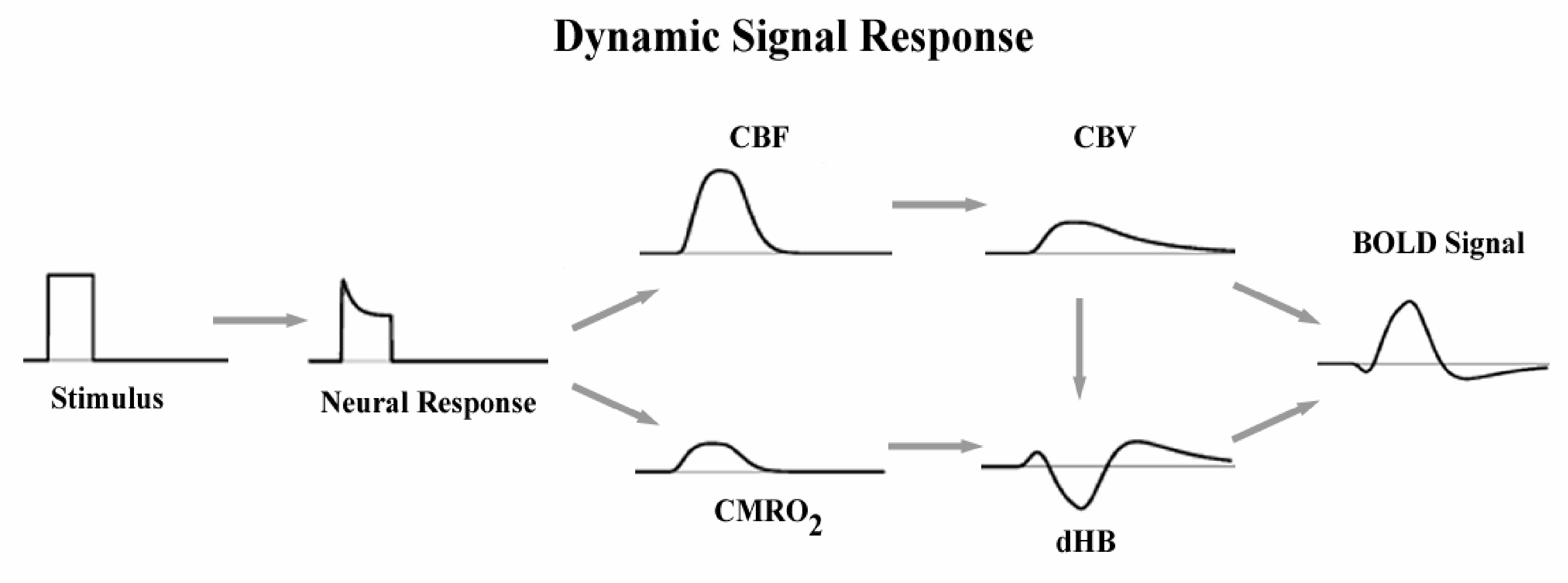

Figure A2.2. Dynamic response of the physiological quantities underlying the BOLD signal. The BOLD signal is a function of [dHb] and CBV which are driven by evoked responses of CBF and $CMRO_2$.

the volume (v) and concentration of deoxyhemoglobin (q) are dynamically defined by a

$$\begin{aligned} \frac{d\boldsymbol{v}}{d\boldsymbol{t}} &= \frac{1}{\tau_0}(\boldsymbol{f}_{\boldsymbol{in}} - \boldsymbol{f}_{\boldsymbol{out}}) \\ \frac{d\boldsymbol{q}}{d\boldsymbol{t}} &= \frac{1}{\tau_0}\left(\frac{\boldsymbol{f}_{\boldsymbol{in}} + \boldsymbol{n} - 1}{\boldsymbol{n}} - \boldsymbol{f}_{\boldsymbol{out}}\frac{\boldsymbol{q}}{\boldsymbol{v}}\right) \end{aligned} \qquad [22]$$

where τ_0 is the mean transit time, n is the coupling parameter, and $\boldsymbol{f}_{\boldsymbol{in}}$ is the flow into the venous compartment as determined by the arteriolar compliance model. The BOLD signal is then determined by a signal model (Chapter 2, Eq. A17) that is a function of the state variable v and q along with constants determined by imaging parameters.

Figure A2.2 is a schematic representing the dynamics response of the various physiological parameters underlying the BOLD effect in fMRI. A stimulus, in this case represented by a block of activity, drives a neural response which reaches a peak and slowly decays as governed by equations 1 and 2. The neural activity modulates the CBF response through the release of a vasoactive agent that acts on the smooth muscle compliance as governed by the arteriolar compliance model put forward in Chapter 2. The CBF response serves as an input into the balloon model which predicts the temporal time courses of CBV and the dHb content. The $CMRO_2$ response is a reflection of the CBF response since a linear coupling was assumed. However, we delay the CBF response relative to the $CMRO_2$ to reveal the initial dip in the depicted BOLD response. With cessation of activation the CBF response returns back to baseline but the CBV response remains elevated due to the viscoelastic properties of the venous compartment. The temporal mismatch between the CBF and CBV response leads to an accumulation of dHb and a post-stimulus undershoot in the BOLD response. This schematic is helpful in understanding the complicated interplay of the various physiological parameters governing the dynamics of the evoked BOLD response.

A2.5 ASL Signal

ASL refers to a class of non-invasive MRI methods for the measurement of CBF and involve taking the difference of two sets of images: tag images, in which the magnetization of arterial blood is inverted or saturated, and control images in which the magnetization of arterial blood in fully relaxed (Golay et al., 2004). There are several variant of ASL and in a popular implementation, PICORE QUIPPS II (Wong et al., 1996), short RF pulses are used to invert a slab of blood that is proximal to the imaging region of interest. For pulsed ASL, after a time TI, needed to allow the tagged blood to flow into the region-of-interest, imaging is performed. In PICORE QUIPPS II, an additional saturation pulse is applied to the same spatial slab prior to imaging to create a temporally defined slab of blood. Figure A2.3 is a schematic representing a typical pulsed ASL experiment, in which tag and control images are acquired in an interleaved fashion.

The difference in the magnetization between tag and control images is proportional to perfusion provided that the QUIPSS II modification is used to remove transit delay sensitivity. Modifying the Bloch equations to account for the PICORE QUIPPS II imaging sequence, the signal difference between control and tag acquisitions, ΔM, measured at time TI_2, is given by:

$$\Delta \boldsymbol{M}(\boldsymbol{TI}_2) = \boldsymbol{f} \cdot 2\alpha \boldsymbol{M}_{0\boldsymbol{A}} \boldsymbol{TI}_1 \boldsymbol{e}^{-\boldsymbol{TI}_2 / \boldsymbol{T}_{1,A}} \qquad [23]$$

where f is cerebral blood flow, TI_1 is the time of the QUIPSS saturation pulse (and therefore defines the tag duration), α is the labeling efficiency, T_{1A} is the longitudinal relaxation time for arterial blood, and M_{0A} is the equilibrium magnetization of arterial blood at time TE, where TE is the echo time.

ASL methods measure a physiological quantity tightly linked to neural activity which can be used to greatly enhance the interpretation of fMRI experiments. As compared to BOLD, ASL measures also have the potential for providing greater localization of the sites of neural activity. (Duong et al., 2001; Luh et al., 2000). However, ASL methods have been limited in use because they have a low signal-to-noise (SNR) which reflects the fact that the CBF signal is a small fraction of the overall magnetic resonance signal from the tissue.

For a quantitative exploration of the inherent low sensitivity of ASL experiments we begin by defining the standard unit of measurement for CBF as (milliliters of blood)/(100 grams of tissue)/ (minute), with a typical value in the human brain is 60 ml/(100 g)/minute. Assuming an average brain tissue density of 1 g/ml, the average CBF may also be written as 60 ml/(100 ml)/minute = 0.01 s-1. In a typical ASL experiment, about 1 second is allowed for the delivery of blood. This corresponds to 1 ml of blood delivered to 100 ml of tissue. As a result, the overall magnetic resonance signal due to increased blood is 1 % of the total tissue signal. Since the ASL signal is a relatively small proportion of the acquired MR signal it is more easily confounded by the presence of physiological noise than the BOLD signal.

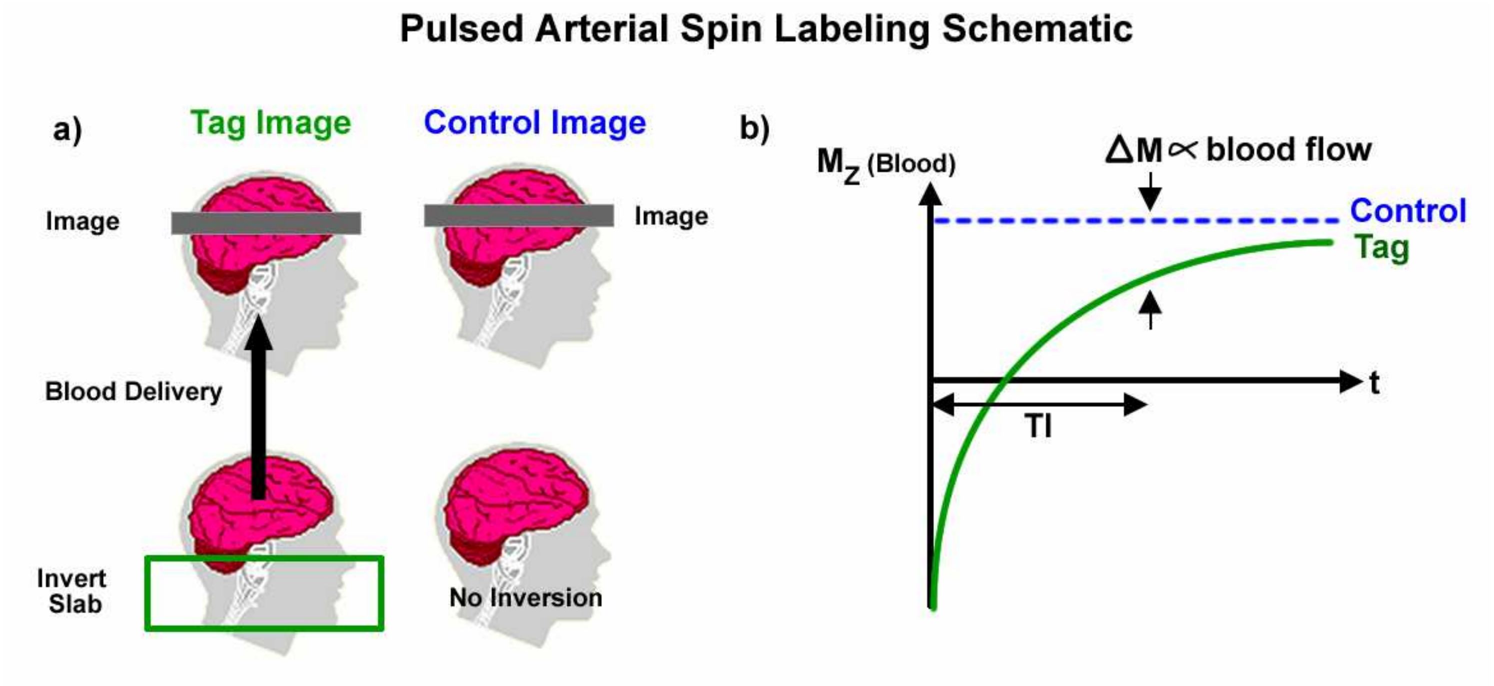

Figure A2.3. Schematic for a basic pulsed ASL method. (a) During a tag acquisition, the blood in a proximal slab is inverted, whereas in a control image there is no inversion. (g) The difference in the between the magnetization of the tag and control images is then proportional to the amount of blood flow in the imaging slice.

A2.6 References

Belliveau J. W., Kennedy D. N., McKinstry R. C., Buchbinder B. R., Weisskoff R. M., Cohen M. S., Vevea J. M., Brady T. J., and Rosen B. R. (1991) Functional mapping of the human visual cortex by magnetic resonance imaging. *Science*. 254, 716-719.

Boxerman J. L., Hamberg L. M., Rosen B. R., and Weisskoff R. M. (1995) MR contrast due to intravascular magnetic susceptibility perturbations. *Magn Reson Med*. 34, 555-566.

Boynton G. M., Engel S. A., Glover G. H., and Heeger D. J. (1996) Linear systems analysis of functional magnetic resonance imaging in human V1. *J Neuroscience*. 16, 4207-4221.

Buxton R. B. (2002) *Introduction to Functional Magnetic Resonance Imaging*. Cambridge University Press, Cambridge.

Buxton R. B., Liu T. T., and Wong E. C. (2001) Nonlinearity of the Hemodynamic Response: Modeling the Neural and BOLD Contributions. In: *9th ISMRM Meeting*), pp. 1164, Glasgow, Scotland.

Buxton R. B., Uludag K., Dubowitz D. J., and Liu T. T. (2004) Modeling the hemodynamic response to brain activation. *Neuroimage*. 23 Suppl 1, S220-233.

Duong T. Q., Kim D. S., Ugurbil K., and Kim S. G. (2001) Localized cerebral blood flow response at submillimeter columnar resolution. *Proc Natl Acad Sci USA*. 98, 10904-10909.

Friston K. J., Mechelli A., Turner R., and Price C. J. (2000) Nonlinear Responses in fMRI: The Balloon Model, Volterra Kernels, and Other Hemodynamics. *NeuroImage*. 12, 466-477.

Fung Y. (1984) *Biomechanics: Circulation*, 2 edn. Springer-Verlag, New York.

Golay X., Hendrikse J., and Lim T. C. (2004) Perfusion Imaging Using Arterial Spin Labeling. *Top Magn Reson Imaging*. 15, 10-27.

Grubb R. L., Raichle M. E., Eichling J. O., and Ter-Pogossian M. M. (1974) The effects of changes in $PaCO_2$ on cerebral blood volume, blood flow, and vascular mean transit time. *Stroke*. 5, 630 - 639.

Hoge R. D., Atkinson J., Gill B., Crelier G. R., Marrett S., and Pike G. B. (1999) Investigation of BOLD signal dependence on cerebral blood flow and oxygen consumption: the deoxyhemoglobin dilution model. *Magn Reson Med*. 42, 849-863.

Iadecola C. (2004) Neurovascular regulation in the normal brain and in Alzheimer's disease. *Nat Rev Neurosci*. 5, 347-360.

Luh W. M., Wong E. C., Bandettini P. A., Ward B. D., and Hyde J. S. (2000) Comparison of simultaneously measured perfusion and BOLD signal increases during brain activation with T(1)-based tissue identification. *Magn Reson Med*. 44, 137-143.

McCulloch and 1943. P. (1943) A logical Calculus of Ideas Immanent in Nervous Activity. *Ibid*. 5, 115-133.

Ogawa S. and Lee T. M. (1992) Functional brain imaging with physiologically sensitive image signals. *JMRI*. 2(P)-WIP suppliment, [Abstr.], S22.

Oja J. M., Gillen J., Kauppinen R. A., Kraut M., and van Zijl P. C. (1999) Venous blood effects in spin-echo fMRI of human brain. *Magn Reson Med*. 42, 617-626.

Raichle M. E. and Mintun M. A. (2006) Brain Work and Brain Imaging. *Annu Rev Neurosci*.

Wong E. C., Buxton R. B., and Frank L. R. (1996) Quantitative imaging of perfusing using a single subtraction (QUIPSS). *Neuroimage*. 3, S5.

A2.7 All References

An H. and Lin W. (2002) Cerebral venous and arterial blood volumes can be estimated separately in humans using magnetic resonance imaging. *Magn Reson Med*. 48, 583-588.

Ances B. M. (2004) Coupling of changes in cerebral blood flow with neural activity: what must initially dip must come back up. *J Cereb Blood Flow Metab*. 24, 1-6.

Ances B. M., Buerk D. G., Greenberg J. H., and Detre J. A. (2001) Temporal dynamics of the partial pressure of brain tissue oxygen during functional forepaw stimulation in rats. *Neurosci Lett*. 306, 106-110.

Ances B. M., Greenberg J. H., and Detre J. A. (2001) The effects of graded hypercapnia on the activation flow coupling response due to forepaw stimulation in alpha-chloralose anesthetized rats. *Brain Res*. 911, 82-88.

Attwell D. and Iadecola C. (2002) The neural basis of functional brain imaging signals. *Trends Neurosci*. 25, 621-625.

Bakalova R., Matsuura T., and Kanno I. (2001) Frequency dependence of local cerebral blood flow induced by somatosensory hind paw stimulation in rat under normo- and hypercapnia. *Jpn J Physiol*. 51, 201-208.

Bandettini P. A., Wong E. C., Hinks R. S., Tikofsky R. S., and Hyde J. S. (1992) Time course EPI of human brain function during task activation. *Magn Reson Med*. 25, 390-397.

Beckmann C. F. and Smith S. M. (2004) Probabilistic independent component analysis for functional magnetic resonance imaging. *IEEE Trans Med Imaging*. 23, 137-152.

Behzadi Y. and Liu T. T. (2005) An arteriolar compliance model of the cerebral blood flow response to neural stimulus. *Neuroimage*. 25, 1100-1111.

Behzadi Y. and Liu T. T. (2005) The Viscoelastic Properties of the Venous Compartment are Dependent on Baseline CBF. In: *ISMRM 13th Scientific Meeting*), pp. 279, Miami.

Behzadi Y. and Liu T. T. (2006) Caffeine reduces the initial dip in the visual BOLD response at 3 T. *Neuroimage*.

Belliveau J. W., Kennedy D. N., McKinstry R. C., Buchbinder B. R., Weisskoff R. M., Cohen M. S., Vevea J. M., Brady T. J., and Rosen B. R. (1991) Functional mapping of the human visual cortex by magnetic resonance imaging. *Science*. 254, 716-719.

Bentourkia M., Bol A., Ivanoiu A., Labar D., Sibomana M., Coppens A., Michel C., Cosnard G., and De Volder A. G. (2000) Comparison of regional cerebral blood flow and glucose metabolism in the normal brain: effect of aging. *J Neurol Sci*. 181, 19-28.

Birn R. M., Diamond J. B., Smith M. A., and Bandettini P. A. (2006) Separating respiratory-variation-related fluctuations from neuronal-activity-related fluctuations in fMRI. *Neuroimage*. 31, 1536-1548.

Biswal B., DeYoe A. E., and Hyde J. S. (1996) Reduction of physiological fluctuations in fMRI using digital filters. *Magn Reson Med*. 35, 107-113.

Blamire A. M., Ogawa S., Ugurbil K., Rothman D., McCarthy G., Ellermann J. M., Hyder F., Rattner Z., and Shulman R. G. (1992) Dynamic mapping of the human visual cortex by high-speed magnetic resonance imaging. *Proc Natl Acad Sci USA*. 89, 11069-11073.

Boxerman J. L., Hamberg L. M., Rosen B. R., and Weisskoff R. M. (1995) MR contrast due to intravascular magnetic susceptibility perturbations. *Magn Reson Med*. 34, 555-566.

Boynton G. M., Engel S. A., Glover G. H., and Heeger D. J. (1996) Linear systems analysis of functional magnetic resonance imaging in human V1. *J Neuroscience*. 16, 4207-4221.

Buckner R. L., Snyder A. Z., Sanders A. L., Raichle M. E., and Morris J. C. (2000) Functional brain imaging of young, nondemented, and demented older adults. *J Cogn Neurosci*. 12 Suppl 2, 24-34.

Burock M. A. and Dale A. M. (2000) Estimation and detection of event-related fMRI signals with temporally correlated noise: a statistically efficient and unbiased approach. *Human Brain Mapping*. 11, 249-260.

Buxton R. B. (2001) The elusive initial dip. *Neuroimage*. 13, 953-958.

Buxton R. B. (2002) *Introduction to Functional Magnetic Resonance Imaging*. Cambridge University Press, Cambridge.

Buxton R. B., Liu T. T., and Wong E. C. (2001) Nonlinearity of the Hemodynamic Response: Modeling the Neural and BOLD Contributions. In: *9th ISMRM Meeting*), pp. 1164, Glasgow, Scotland.

Buxton R. B., Miller K., Frank L. R., and Wong E. C. (1998) BOLD signal dynamics: the balloon model with viscoelastic effects. In: *Sixth Meeting, International Society for Magnetic Resonance in Medicine*), pp. 1401, Sydney, Australia.

Buxton R. B., Miller K. L., Wong E. C., and Frank L. R. (1998) BOLD signal dynamics: the balloon model with viscoelastic effects. In: *Proc. 6th Annual Meeting ISMRM*), pp. 1401, Sydney.

Buxton R. B., Uludag K., Dubowitz D. J., and Liu T. T. (2004) Modeling the hemodynamic response to brain activation. *Neuroimage*. 23 Suppl 1, S220-233.

Buxton R. B., Wong E. C., and Frank L. R. (1998) Dynamics of blood flow and oxygenation changes during brain activation: the balloon model. *Magn Reson Med*. 39, 855-864.

Buxton R. B., Wong E. C., and Frank L. R. (1998) The post-stimulus undershoot of the functional MRI signal.

Cameron O. G., Modell J. G., and Hariharan M. (1990) Caffeine and human cerebral blood flow: a positron emission tomography study. *Life Sci*. 47, 1141-1146.

Chalela J., Alsop D. C., Gonzalez-Atavales J. B., Maldjian J. A., Kasner S. E., and Detre J. A. (2000) Magnetic resonance perfusion imaging in acute ischemic stroke using continuous arterial spin labeling. *Stroke*. 31, 680-687.

Cohen E. R., Ugurbil K., and Kim S. G. (2002) Effect of basal conditions on the magnitude and dynamics of the blood oxygenation level-dependent fMRI response. *J Cereb Blood Flow Metab*. 22, 1042-1053.

Cox R. W. (1996) AFNI-software for analysis and visualization of functional magnetic resonance neuroimages. *Comput Biomed Res*. 29, 162-173.

Dagli M. S., Ingeholm J. E., and Haxby J. V. (1999) Localization of cardiac-induced signal change in fMRI. *Neuroimage*. 9, 407-415.

Davis M. J. and Gore R. W. (1989) Length-tension relationship of vascular smooth muscle in single arterioles. *Am J Physiol*. 256, H630-640.

Davis M. J. and Hill M. A. (1999) Signaling mechanisms underlying the vascular myogenic response. *Physiol Rev*. 79, 387-423.

Davis T. L., Kwong K. K., Weisskoff R. M., and Rosen B. R. (1998) Calibrated functional MRI: mapping the dynamics of oxidative metabolism. *Proc Natl Acad Sci USA*. 95, 1834-1839.

D'Esposito M., Deouell L. Y., and Gazzaley A. (2003) Alterations in the BOLD fMRI signal with ageing and disease: a challenge for neuroimaging. *Nat Rev Neurosci*. 4, 863-872.

D'Esposito M., Zarahn E., Aguirre G. K., and Rypma B. (1999) The effect of normal aging on the coupling of neural activity to the BOLD hemodynamic response. *NeuroImage*. 10, 6-14.

Duong T. Q., Kim D. S., Ugurbil K., and Kim S. G. (2000) Spatiotemporal dynamics of the BOLD fMRI signals: toward mapping submillimeter cortical columns using the early negative response. *Magn Reson Med*. 44, 231-242.

Duong T. Q., Kim D. S., Ugurbil K., and Kim S. G. (2001) Localized cerebral blood flow response at submillimeter columnar resolution. *Proc Natl Acad Sci USA*. 98, 10904-10909.

Ernst T. and Hennig J. (1994) Observation of a fast response in functional MR. *Magn Reson Med*, 146-149.

Field A. S., Laurienti P. M., Yen Y.-F., Burdette J. H., and Moody D. M. (2003) Dietary Caffeine Consumption and Withdrawal: Confounding Variables in Quantitative Cerebral Perfusion Studies? *Radiology*. 227, 129-135.

Fransson P., Kruger G., Merboldt K. D., and Frahm J. (1998) Temporal characteristics of oxygenation-sensitive MRI responses to visual activation in humans. *Magn Reson Med*. 39, 912-919.

Fredholm B. B., Battig K., Holmen J., Nehlig A., and Zvartau E. E. (1999) Actions of caffeine in the brain with special reference to factors that contribute to its widespread use. *Pharmacol Rev*. 51, 83-133.

Friston K. J. (2002) Bayesian estimation of dynamical systems: an application to fMRI. *Neuroimage*. 16, 513-530.

Friston K. J., Harrison L., and Penny W. (2003) Dynamic causal modelling. *Neuroimage*. 19, 1273-1302.

Friston K. J., Mechelli A., Turner R., and Price C. J. (2000) Nonlinear Responses in fMRI: The Balloon Model, Volterra Kernels, and Other Hemodynamics. *NeuroImage*. 12, 466-477.

Fukuda M., Wang P., Moon C., Tanifuji M., and Kim S. G. (2005) Spatial specificity of the enhanced dip inherently induced by prolonged oxygen consumption in cat visual cortex: Implication for columnar resolution functional MRI. *Neuroimage*. in-press.

Fung Y. (1984) *Biomechanics: Circulation*, 2 edn. Springer-Verlag, New York.

Fung Y. (1993) *Biomechanics: Mechanical Properties of Living Tissues*. Springer-Verlag, New York.

Fung Y. (1994) *A First Course in Continuum Mechanics*, Third edn. Prentice Hall, New Jersey.

Fung Y. C. (1997) *Biomechanics: Circulation*. Springer-Verlag, New York.

Glover G. H., Li T. Q., and Ress D. (2000) Image-based method for retrospective correction of physiological motion effects in fMRI: RETROICOR. *Magn Reson Med*. 44, 162-167.

Glover G. H., Li T.-Q., and Ress D. (2000) Image-based method for retrospective correction of physiological motion effects in fMRI: RETROICOR. *Magn Res Med*. 44, 162-167.

Golay X., Hendrikse J., and Lim T. C. (2004) Perfusion Imaging Using Arterial Spin Labeling. *Top Magn Reson Imaging*. 15, 10-27.

Grubb R. L., Raichle M. E., Eichling J. O., and Ter-Pogossian M. M. (1974) The effects of changes in $PaCO_2$ on cerebral blood volume, blood flow, and vascular mean transit time. *Stroke*. 5, 630 - 639.

Hajdu M. A., Heistad D. D., Siems J. E., and Baumbach G. L. (1990) Effects of aging on mechanics and composition of cerebral arterioles in rats. *Circ Res*. 66, 1747-1754.

Handwerker D. A., Ollinger J. M., and D'Esposito M. (2004) Variation of BOLD hemodynamic responses across subjects and brain regions and their effects on statistical analyses. *Neuroimage*. 21, 1639-1651.

Hinke R. M., Hu X., Stillman A. E., Kim S.-G., Merkle H., Salmi R., and Ugurbil K. (1993) Functional magnetic resonance imaging of brocs's area during internal speech. *Neuroreport*. 4, 675-678.

Hoge R. D., Atkinson J., Gill B., Crelier G. R., Marrett S., and Pike G. B. (1999) Investigation of BOLD signal dependence on cerebral blood flow and oxygen consumption: the deoxyhemoglobin dilution model. *Magn Reson Med*. 42, 849-863.

Hoge R. D., Atkinson J., Gill B., Crelier G. R., Marrett S., and Pike G. B. (1999) Linear coupling between cerebral blood flow and oxygen consumption in activated human cortex. *Proc Natl Acad Sci U S A*. 96, 9403-9408.

Hu X., Le T. H., Parrish T., and Erhard P. (1995) Retrospective estimation and correction of physiological fluctuation in functional MRI. *Magn Reson Med*. 34, 201-212.

Hu X., Le T. H., and Ugurbil K. (1997) Evaluation of the early response in fMRI in individual subjects using short stimulus duration. *Magn Reson Med*. 37, 877-884.

Huettel S. A., Singerman J. D., and McCarthy G. (2001) The effects of aging upon the hemodynamic response measured by functional MRI. *Neuroimage*. 13, 161-175.

Iadecola C. (2004) Neurovascular regulation in the normal brain and in Alzheimer's disease. *Nat Rev Neurosci*. 5, 347-360.

Irikura K., Maynard K. I., and Moskowitz M. A. (1994) Importance of nitric oxide synthase inhibition to the attenuated vascular responses induced by topical L-nitroarginine during vibrissal stimulation. *J Cereb Blood Flow Metab*. 14, 45-48.

Ito H., Kanno I., Ibaraki M., Hatazawa J., and Miura S. (2003) Changes in human cerebral blood flow and cerebral blood volume during hypercapnia and hypocapnia measured by positron emission tomography. *J Cereb Blood Flow Metab*. 23, 665-670.

Jackson D. A. (1993) Stopping Rules in Principal Components Analysis: A Comparison of Heuristical and Statistical Approaches. *Ecology*. 74, 2204-2214.

Jones M., Berwick J., Johnston D., and Mayhew J. (2001) Concurrent optical imaging spectroscopy and laser-Doppler flowmetry: the relationship between blood flow, oxygenation, and volume in rodent barrel cortex. *Neuroimage*. 13, 1002-1015.

Josephs O., Howseman A., Friston K. J., and Turner R. (2001) Physiological Noise Modelling for multi-slice EPI fMRI using SPM. *Proc Intl Soc Mag Reson Med*, 1682.

Kashikura K., Kershaw J., Kashikura A., Zhang X., Matsuura T., and Kanno I. (2001) Hyperoxia modified activation-induced blood oxygenation level-dependent response of human visual cortex (V1): an event-related functional magnetic resonance imaging study. *Neurosci Lett*. 299, 53-56.

Kastrup A., Kruger G., Neumann-Haefelin T., Glover G. H., and Moseley M. E. (2002) Changes of cerebral blood flow, oxygenation, and oxidative metabolism during graded motor activation. *Neuroimage*. 15, 74-82.

Katura T., Tanaka N., Obata A., Sato H., and Maki A. (2006) Quantitative evaluation of interrelations between spontaneous low-frequency oscillations in cerebral hemodynamics and systemic cardiovascular dynamics. *Neuroimage*. 31, 1592-1600.

Kemna L. J. and Posse S. (2001) Effect of respiratory CO(2) changes on the temporal dynamics of the hemodynamic response in functional MR imaging. *Neuroimage*. 14, 642-649.

Kety S. and Schmidt C. (1948) Nitrous oxide method for the quantitative determination of cerebral blood flow in man: Theory, procedure and normal values. *J Clin Invest*. 27, 475-483.

Kim D. S., Duong T. Q., and Kim S. G. (2000) High-resolution mapping of iso-orientation columns by fMRI. *Nat Neurosci*. 3, 164-169.

Kim S.-G., Ashe J., Hendrich K., Ellerman J. M., Merkle H., Ugurbil K., and Georgopoulos A. P. (1993) Functional magnetic resonance imaging of motor cortex: hemispheric asymmetry and handedness. *Science*. 261, 615-616.

Kruger G. and Glover G. H. (2001) Physiological noise in oxygenation-sensitive magnetic resonance imaging. *Magn Reson Med*. 46, 631-637.

Kwong K. K., Belliveau J. W., Stern C. E., Chesler D. A., Goldberg I. E., Poncelet B. P., Kennedy D. N., Weisskoff R. M., Cohen M. S., Turner R., Cheng H.-M., Brady T. J., and Rosen B. R. (1992) Functional MR imaging of primary visual and motor cortex. *JMRI*. 2(P) [Abstr.], 76.

Lash J. M., Bohlen H. G., and Waite L. (1991) Mechanical characteristics and active tension generation in rat intestinal arterioles. *Am J Physiol*. 260, H1561-1574.

Lauterbur P. C. (1973) Image formation by induced local interactions: examples employing nuclear magnetic resonance. *Nature*. 242, 190-191.

Leenders K. L., Perani D., Lammertsma A. A., Heather J. D., Buckingham P., Healy M. J. R., Gibbs J. M., Wise R. J. S., Hatazawa J., Herold S., Beaney R. P., Brooks D. B., Spinks T., Rhodes C., Frackowiak R. S. J., and Jones T. (1990) Cerebral blood flow, blood volume and oxygen utilization: Normal values and effect of age. *Brain*. 113, 27-47.

Li D., Wang Y., and Waight D. J. (1998) Blood oxygen saturation assessment in vivo using T2* estimation. *Magn Reson Med*. 39, 685-690.

Lindauer U., Royl G., Leithner C., Kuhl M., Gold L., Gethmann J., Kohl-Bareis M., Villringer A., and Dirnagl U. (2001) No evidence for early decrease in blood oxygenation in rat whisker cortex in response to functional activation. *Neuroimage*. 13, 988-1001.

Liu C. S., Miki A., Hulvershorn J., Bloy L., Gualtieri E. E., Liu G. T., Leigh J. S., Haselgrove J. C., and Elliott M. A. (2006) Spatial and temporal characteristics of physiological noise in fMRI at 3T. *Acad Radiol*. 13, 313-323.

Liu T. T., Behzadi Y., Restom K., and Uludag K. (2004) Caffeine Affects the Dynamics of the Visual BOLD Response. *NeuroImage*. 22, TU148.

Liu T. T., Behzadi Y., Restom K., Uludag K., Lu K., Buracas G. T., Dubowitz D. J., and Buxton R. B. (2004) Caffeine alters the temporal dynamics of the visual BOLD response. *Neuroimage*. 23, 1402-1413.

Logothetis N. K., Guggenberger H., Peled S., and Pauls J. (1999) Functional imaging of the monkey brain. *Nat Neurosci*. 2, 555-562.

Logothetis N. K. and Wandell B. A. (2004) Interpreting the BOLD signal. *Annu Rev Physiol*. 66, 735-769.

Luh W. M., Wong E. C., Bandettini P. A., Ward B. D., and Hyde J. S. (2000) Comparison of simultaneously measured perfusion and BOLD signal increases during brain activation with T(1)-based tissue identification. *Magn Reson Med*. 44, 137-143.

Lund T. E. and Hanson L. G. (2001) Physiological Noise Reduction in fMRI Using Vessel Time-Series as Covariates in a General Linear Model. *Proc Intl Soc Mag Reson Med*. 9, 22.

Lund T. E., Madsen K. H., Sidaros K., Luo W. L., and Nichols T. E. (2006) Non-white noise in fMRI: does modelling have an impact? *Neuroimage*. 29, 54-66.

Malonek D. and Grinvald A. (1996) Interactions between electrical activity and cortical microcirculation revealed by imaging spectroscopy: implications for functional brain mapping. *Science*. 272, 551-554.

Mandeville J. B., Marota J. J., Ayata C., Moskowitz M. A., Weisskoff R. M., and Rosen B. R. (1999) MRI measurement of the temporal evolution of relative CMRO(2) during rat forepaw stimulation. *Magn Reson Med*. 42, 944-951.

Mandeville J. B., Marota J. J. A., Ayata C., Zaharchuk G., Moskowitz M. A., Rosen B. R., and Weisskoff R. M. (1999) Evidence of a cerebrovascular postarteriole windkessel with delayed compliance. *J Cereb Blood Flow Metab*. 19, 679-689.

Mansfield P. (1977) Multi-planar image formation using NMR spin echoes. *J Phys*. C10, L55-L58.

Marchal G., Rioux P., Petit-Taboue M.-C., Sette G., Travere J.-M., LePoec C., Courtheoux P., Derlon J.-M., and Baron J.-C. (1992) Regional cerebral oxygen consumption, blood flow, and blood volume in healthy human aging. *Arch Neurol*. 49, 1013-1020.

Marota J. J., Ayata C., Moskowitz M. A., Weisskoff R. M., Rosen B. R., and Mandeville J. B. (1999) Investigation of the early response to rat forepaw stimulation. *Magn Reson Med*. 41, 247-252.

Martin A. J., Friston K. J., Colebatch J. G., and Frackowiak R. S. (1991) Decreases in regional cerebral blood flow with normal aging. *J Cereb Blood Flow Metab*. 11, 684-689.

Martinez-Lemus L. A., Wu X., Wilson E., Hill M. A., Davis G. E., Davis M. J., and Meininger G. A. (2003) Integrins as unique receptors for vascular control. *J Vasc Res*. 40, 211-233.

Matsuura T., Fujita H., Kashikura K., and Kanno I. (2000) Evoked local cerebral blood flow induced by somatosensory stimulation is proportional to the baseline flow. *Neurosci Res*. 38, 341-348.

Matsuura T., Fujita H., Kashikura K., and Kanno I. (2000) Modulation of evoked cerebral blood flow under excessive blood supply and hyperoxic conditions. *Jpn J Physiol*. 50, 115-123.

Matsuura T., Kashikura K., and Kanno I. (2001) Hemodynamics of local cerebral blood flow induced by somatosensory stimulation under normoxia and hyperoxia in rats. *Comp Biochem Physiol A Mol Integr Physiol*. 129, 363-372.

Mayhew J. E., Askew S., Zheng Y., Porrill J., Westby G. W., Redgrave P., Rector D. M., and Harper R. M. (1996) Cerebral vasomotion: a 0.1-Hz oscillation in reflected light imaging of neural activity. *Neuroimage*. 4, 183-193.

McCulloch and 1943. P. (1943) A logical Calculus of Ideas Immanent in Nervous Activity. *Ibid*. 5, 115-133.

McKeown M. J., Hansen L. K., and Sejnowsk T. J. (2003) Independent component analysis of functional MRI: what is signal and what is noise? *Curr Opin Neurobiol*. 13, 620-629.

McKeown M. J. and Sejnowski T. J. (1998) Independent component analysis of fMRI data: examining the assumptions. *Hum Brain Mapp*. 6, 368-372.

Mehagnoul-Schipper D. J., van der Kallen B. F., Colier W. N., van der Sluijs M. C., van Erning L. J., Thijssen H. O., Oeseburg B., Hoefnagels W. H., and Jansen R. W. (2002) Simultaneous measurements of cerebral oxygenation changes during brain activation by near-infrared spectroscopy and functional magnetic resonance imaging in healthy young and elderly subjects. *Hum Brain Mapp*. 16, 14-23.

Menon R. S., Ogawa S., Strupp J. P., Anderson P., and Ugurbil K. (1995) BOLD based functional MRI at 4 tesla includes a capillary bed contribution: echo-planar imaging correlates with previous optical imaging using intrinsic signals. *Magn Reson Med*. 33, 453 - 459.

Mildner T., Norris D. G., Schwarzbauer C., and Wiggins C. J. (2001) A Qualitative Test of the Balloon Model for BOLD-based MR Signal Changes at 3T. *Magn Reson Med*. 46, 891-899.

Miller K. L., Luh W. M., Liu T. T., Martinez A., Obata T., Wong E. C., Frank L. R., and Buxton R. B. (2001) Nonlinear temporal dynamics of the cerebral blood flow response. *Hum Brain Mapp*. 13, 1-12.

Mosso A. (1881) *Uber den Kreislauf des Blutes im Menschlichen Gehirn.* Verlag von Veit & Co., Leipzig.

Mumford J. A., Hernandez-Garcia L., Lee G. R., and Nichols T. E. (2006) Estimation efficiency and statistical power in arterial spin labeling fMRI. *Neuroimage*. 33, 103-114.

Murray K. J. (1990) Cyclic AMP and mechanisms of vasodilation. *Pharmacol Ther*. 47, 329-345.

Nakao Y., Itoh Y., Kuang T. Y., Cook M., Jehle J., and Sokoloff L. (2001) Effects of anesthesia on functional activation of cerebral blood flow and metabolism. *Proc Natl Acad Sci U S A*. 98, 7593-7598.

Ngai A. C., Coyne E. F., Meno J. R., West G. A., and Winn H. R. (2001) Receptor subtypes mediating adenosine-induced dilation of cerebral arterioles. *Am J Physiol Heart Circ Physiol*. 280, H2329-2335.

Obata T., Liu T. T., Miller K. L., Luh W. M., Wong E. C., Frank L. R., and Buxton R. B. (2004) Discrepancies between BOLD and flow dynamics in primary and supplementary motor areas: application of the balloon model to the interpretation of BOLD transients. *Neuroimage*. 21, 144-153.

Ogawa S. and Lee T. M. (1992) Functional brain imaging with physiologically sensitive image signals. *JMRI*. 2(P)-WIP suppliment, [Abstr.], S22.

Ogawa S. and Lee T.-M. (1990) Magnetic resonance imaging of blood vessels at high fields: in vivo and in vitro measurements and image simulation. *Magn Reson Med*. 16, 9-18.

Oja J. M., Gillen J., Kauppinen R. A., Kraut M., and van Zijl P. C. (1999) Venous blood effects in spin-echo fMRI of human brain. *Magn Reson Med*. 42, 617-626.

Osborne P. G. (1997) Hippocampal and striatal blood flow during behavior in rats: chronic laser Doppler flowmetry study. *Physiol Behav*. 61, 485-492.

Panczel G., Daffertshofer M., Ries S., Spiegel D., and Hennerici M. (1999) Age and stimulus dependency of visually evoked cerebral blood flow responses. *Stroke*. 30, 619-623.

Pantano P., Baron J. C., Lebrun-Grandie P., Duquesnoy N., Bousser M. G., and Comar D. (1984) Regional cerebral blood flow and oxygen consumption in human aging. *Stroke*. 15, 635-641.

Pauling L. and Coryell C. D. (1936) The magnetic properties and structure of hemoglobin, oxyhemoglobin, and carbonmonoxyhemoglobin. *Proc Natl Acad Sci USA*. 22, 210-216.

Petersen N., Jensen J., Burchardt J., and Stodkilde-Jorgensen H. (1998) State space models for physiological noise in fMRI time series. *Neuroimage*. 7, 727-741.

Pfeuffer J., Van de Moortele P. F., Ugurbil K., Hu X., and Glover G. H. (2002) Correction of physiologically induced global off-resonance effects in dynamic echo-planar and spiral functional imaging. *Magn Reson Med*. 47, 344-353.

Raichle M. E. and Mintun M. A. (2006) Brain Work and Brain Imaging. *Annu Rev Neurosci*.

Restom K., Behzadi Y., and Liu T. T. (2006) Physiological noise reduction for arterial spin labeling functional MRI. *Neuroimage*. 31, 1104-1115.

Restom K., Behzadi Y., Uludag K., and Liu T. T. (2004) Image Based Physiological Noise Correction for Perfusion-Based fMRI. In: *12th ISMRM Scientific Meeting*), pp. 2525, Kyoto.

Richter W. and Richter M. (2003) The shape of the fMRI BOLD response in children and adults changes systematically with age. *Neuroimage*. 20, 1122-1131.

Riddle D. R., Sonntag W. E., and Lichtenwalner R. J. (2003) Microvascular plasticity in aging. *Ageing Res Rev*. 2, 149-168.

Rosengarten B., Spiller A., Aldinger C., and Kaps M. (2003) Control system analysis of visually evoked blood flow regulation in humans under normocapnia and hypercapnia. *Eur J Ultrasound*. 16, 169-175.

Rostrup E., Law I., Pott F., Ide K., and Knudsen G. M. (2002) Cerebral hemodynamics measured with simultaneous PET and near-infrared spectroscopy in humans. *Brain Res*. 954, 183-193.

Roy C. S. and Sherrington C. S. (1890) On the regulation of the blood-supply of the brain. *J Physiol*. 11, 85-108.

Schroeter M. L., Zysset S., Kruggel F., and von Cramon D. Y. (2003) Age dependency of the hemodynamic response as measured by functional near-infrared spectroscopy. *Neuroimage*. 19, 555-564.

Sicard K., Shen Q., Brevard M. E., Sullivan R., Ferris C. F., King J. A., and Duong T. Q. (2003) Regional cerebral blood flow and BOLD responses in conscious and anesthetized rats under basal and hypercapnic conditions: implications for functional MRI studies. *J Cereb Blood Flow Metab*. 23, 472-481.

Silva A. C., Iadecola C., and Kim S.-G. (1999) The Dependence of BOLD and CBF Changes on the CBF Baseline during Somatsensory Simulation. In: *Seventh ISMRM Scientific Meeting*), pp. 1736, Philadelphia, PA.

Silva A. C., Lee S. P., Iadecola C., and Kim S. G. (2000) Early temporal characteristics of cerebral blood flow and deoxyhemoglobin changes during somatosensory stimulation. *J Cereb Blood Flow Metab*. 20, 201-206.

Silvennoinen M. J., Clingman C. S., Golay X., Kauppinen R. A., and van Zijl P. C. (2003) Comparison of the dependence of blood R2 and R2* on oxygen saturation at 1.5 and 4.7 Tesla. *Magn Reson Med*. 49, 47-60.

Smith S. M., Jenkinson M., Woolrich M. W., Beckmann C. F., Behrens T. E., Johansen-Berg H., Bannister P. R., De Luca M., Drobnjak I., Flitney D. E., Niazy R. K., Saunders J., Vickers J., Zhang Y., De Stefano N., Brady J. M., and Matthews P. M. (2004) Advances in functional and structural MR image analysis and implementation as FSL. *Neuroimage*. 23 Suppl 1, S208-219.

Somlyo A. P. and Somlyo A. V. (1994) Signal transduction and regulation in smooth muscle. *Nature*. 372, 231-236.

Stewart G. N. (1894) Researches on the circulation time in organs and on the influences which affect it. *J Physiol (London)*. 15, Parts I-III.

Stoica P. and Moses R. (1997) *Introduction to Spectral Analysis*. Prentice-Hall, Upper Saddle River, NJ.

Taoka T., Iwasaki S., Uchida H., Fukusumi A., Nakagawa H., Kichikawa K., Takayama K., Yoshioka T., Takewa M., and Ohishi H. (1998) Age correlation of the time lag in signal change on EPI-fMRI. *J Comput Assist Tomogr*. 22, 514-517.

Thomas C. G., Harshman R. A., and Menon R. S. (2002) Noise reduction in BOLD-based fMRI using component analysis. *Neuroimage*. 17, 1521-1537.

Thompson J. K., Peterson M. R., and Freeman R. D. (2004) High-resolution neurometabolic coupling revealed by focal activation of visual neurons. *Nat Neurosci*. 7, 919-920.

Uludag K. and Buxton R. (2005) The Compartmental Balloon Model. In: *12th ISMRM.*), Miami.

Ursino M. (1991) Mechanisms of cerebral blood flow regulation. *Critical Reviews in Biomedical Engineering*. 18, 255-288.

Vanzetta I. and Grinvald A. (1999) Increased cortical oxidative metabolism due to sensory stimulation: implications for functional brain imaging. *Science*. 286, 1555-1558.

Wang J., M.Qiu, and Constable R. T. (2005) In vivo method for corrrecting transmit/receive nonuniformities with phased array coils. *Magn Reson Imaging*. 53, 666-674.

West G. A., Meno J. R., Nguyen T. S., Ngai A. C., Simard J. M., and Winn H. R. (2003) cGMP-dependent and not cAMP-dependent kinase is required for adenosine-induced dilation of intracerebral arterioles. *J Cardiovasc Pharmacol*. 41, 444-451.

Wilson H. R. (1999) *Spikes, Decisions and Actions: Dynamical Foundations of Neuroscience*. Oxford University Press, Oxford.

Wong E. C., Buxton R. B., and Frank L. R. (1996) Quantitative imaging of perfusing using a single subtraction (QUIPSS). *Neuroimage*. 3, S5.

Wong E. C., Buxton R. B., and Frank L. R. (1998) Quantitative imaging of perfusion using a single subtraction (QUIPSS and QUIPSS II). *Magn Reson Med*. 39, 702-708.

Woolrich M. W., Ripley B. D., Brady M., and Smith S. M. (2001) Temporal autocorrelation in univariate linear modeling of FMRI data. *Neuroimage*. 14, 1370-1386.

Yacoub E. and Hu X. (2001) Detection of the early decrease in fMRI signal in the motor area. *Magn Reson Med*. 45, 184-190.

Yacoub E., Le T. H., Ugurbil K., and Hu X. (1999) Further evaluation of the initial negative response in functional magnetic resonance imaging. *Magn Reson Med*. 41, 436-441.

Yacoub E., Shmuel A., Pfeuffer J., Van De Moortele P. F., Adriany G., Andersen P., Vaughan J. T., Merkle H., Ugurbil K., and Hu X. (2001) Imaging brain function in humans at 7 Tesla. *Magn Reson Med*. 45, 588-594.

Yacoub E., Shmuel A., Pfeuffer J., Van De Moortele P. F., Adriany G., Ugurbil K., and Hu X. (2001) Investigation of the initial dip in fMRI at 7 Tesla. *NMR Biomed*. 14, 408-412.

Yang J., Clark J. W., Jr., Bryan R. M., and Robertson C. (2003) The myogenic response in isolated rat cerebrovascular arteries: smooth muscle cell model. *Med Eng Phys*. 25, 691-709.

Yang J., Clark J. W., Jr., Bryan R. M., and Robertson C. S. (2003) The myogenic response in isolated rat cerebrovascular arteries: vessel model. *Med Eng Phys*. 25, 711-717.

Zheng Y., Martindale J., Johnston D., Jones M., Berwick J., and Mayhew J. (2002) A model of the hemodynamic response and oxygen delivery to brain. *Neuroimage*. 16, 617-637.